

Universität des Saarlandes



Fachrichtung Physik

# **Artificial Intelligence-Based Assessment for Red Blood Cell-Related Disease Characterization**

---

Dissertation  
zur Erlangung des Grades  
des Doktors der Naturwissenschaften  
der Naturwissenschaftlich-Technischen Fakultät  
der Universität des Saarlandes  
von

**Marcelle Guedes de Medeiros Lopes**

---

Saarbrücken  
2025

**Tag des Kolloquiums:** 10.10.2025

**Dekan:** Prof. Dr.-Ing. Dirk Bähre

**Berichterstatter:** Prof. Dr. Lars Kaestner  
Prof. Dr. Stéphane Egée

**Akad. Mitglied:** Dr. Divyendu Goud Thalla

**Vorsitz:** Prof. Dr. Rolf Pelster

To the memory of my grandfather Heráclito, whose constant encouragement in the pursuit of knowledge live on within me.

“Cantar (e cantar e cantar) a beleza de ser um eterno aprendiz.”

Gonzaguinha

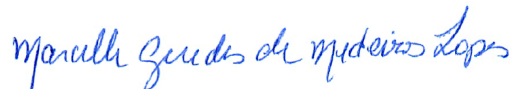




## Eidesstattliche Erklärung

Hiermit versichere ich an Eides statt, dass ich die vorliegende Arbeit selbstständig und ohne Benutzung anderer als der angegebenen Hilfsmittel angefertigt habe. Die aus anderen Quellen oder indirekt übernommenen Daten und Konzepte sind unter Angabe der Quelle gekennzeichnet. Die Arbeit wurde bisher weder im In- noch im Ausland in gleicher oder ähnlicher Form in einem Verfahren zur Erlangung eines akademischen Grades vorgelegt.

Saarbrücken, 23.11.2023  
Ort, Datum

  
Marcelle Guedes de Medeiros Lopes



# Abstract

The adaptability and deformability of red blood cells (RBCs) are crucial for efficient microvascular perfusion and gas exchange, enabling these cells to conform to varying vessel flow conditions. This thesis investigates changes in RBC deformability occurring in diseases such as Neuroacanthocytosis Syndromes (NAS), Sickle Cell Disease (SCD), and conditions like COVID-19.

Traditionally, diagnosing these conditions involves genetic analysis and manual assessment of RBC shapes. This thesis proposes an automated method using artificial intelligence (AI) and image processing to analyze single RBC shapes in real-time flow. This innovative approach shows promise in characterizing diverse RBC shape abnormalities seen in blood disorders.

Chapter one discusses blood properties and RBC behavior in microcapillaries. Chapter two explains details of materials and methods. The third chapter focuses on methodology development, including image processing tools and AI implementation. In chapter four, RBC morphology is discussed in detail for diseases like COVID-19, NAS, SCD, and others. The thesis concludes by summarizing findings and suggesting future research directions.



# Zusammenfassung

Die Deformierbarkeit von Erythrozyten (red blood cells, RBCs) ist für eine effiziente mikrovaskuläre Durchblutung und den Gasaustausch von entscheidender Bedeutung, da sie es diesen Zellen ermöglicht, sich an unterschiedliche Strömungsbedingungen anzupassen. In dieser Arbeit werden Veränderungen in der Verformbarkeit der Erythrozyten untersucht, die bei Krankheiten wie Neuroakanthozytose-Syndromen (NAS), der Sichelzellkrankheit (SCD) und Erkrankungen wie COVID-19 auftreten.

Für die Diagnose vieler Krankheiten sind traditionell eine genetische Analyse oder eine manuelle Bewertung der Erythrozytenform erforderlich. In dieser Arbeit wird eine automatisierte Methode vorgeschlagen, bei der KI und Bildverarbeitung eingesetzt werden, um die Form einzelner Erythrozyten in Echtzeit zu analysieren. Dieser innovative Ansatz ist vielversprechend für die Diagnose verschiedener Anomalien der Erythrozytenform, die bei Blutkrankheiten auftreten.

Im ersten Kapitel werden die Eigenschaften von Blut und insbesondere das Verhalten der Erythrozyten in Mikrokapillaren beschrieben. Kapitel zwei erläutert Einzelheiten zu den verwendeten Materialien und Methoden. Das dritte Kapitel konzentriert sich auf die Entwicklung der Methodik, einschließlich der Bildverarbeitung und der KI-Implementierung. In Kapitel vier wird die Morphologie der Erythrozyten bei Krankheiten wie COVID-19, NAS, SCD und anderen Krankheiten im Detail diskutiert. Die Arbeit schließt mit einer Zusammenfassung der Ergebnisse und Vorschlägen für zukünftige Forschungsrichtungen ab.



## List of author's publication

- **Lopes, Marcelle G.M., Steffen M. Recktenwald, Greta Simionato, Hermann Eichler, Christian Wagner, Stephan Quint, and Lars Kaestner**  
Big Data in Transfusion Medicine and Artificial Intelligence Analysis for Red Blood Cell Quality Control.  
Transfusion Medicine and Hemotherapy 50, no. 3 (2023): 163–73.  
<https://doi.org/10.1159/000530458>.
- **Recktenwald, Steffen M., Marcelle G. M. Lopes, Stephana Peter, Sebastian Hof, Greta Simionato, Kevin Peikert, Andreas Hermann, *et al.***  
Erysense, a Lab-on-a-Chip-Based Point-of-Care Device to Evaluate Red Blood Cell Flow Properties With Multiple Clinical Applications.  
Frontiers in Physiology 13 (April 27, 2022): 884690.  
<https://doi.org/10.3389/fphys.2022.884690>
- **Recktenwald, Steffen M., Greta Simionato, Marcelle G. M. Lopes, Fabia Gamboni, Monika Dzieciatkowska, Patrick Meybohm, Kai Zacharowski, *et al.***  
Cross-Talk between Red Blood Cells and Plasma Influences Blood Flow and Omics Phenotypes in Severe COVID-19.  
Preprint. Hematology, March 31, 2022.  
<https://doi.org/10.1101/2022.03.31.22273226>.
- **Martin-Wortham, Julie, Steffen M. Recktenwald, Marcelle G. M. Lopes, Lars Kaestner, Christian Wagner, and Stephan Quint**  
A Deep Learning-Based Concept for High Throughput Image Flow Cytometry.  
Applied Physics Letters 118, no. 12 (March 22, 2021): 123701.  
<https://doi.org/10.1063/5.0037336>





## Declaration of author contributions

In this section, declarations corresponding to the papers listed in the preceding section are presented. These declarations detail the specific roles and contributions of each co-author in the scientific research, methodology, data analysis, and manuscript preparation, thereby ensuring transparency and accountability in the collaborative efforts supporting each publication.

All reasonable efforts were undertaken to contact every co-author listed in the publications to obtain their explicit confirmation and signature regarding their respective contributions. Nevertheless, despite multiple attempts through various channels, it was not possible to establish contact with certain co-authors. The attribution of contributions to these individuals is based on the descriptions provided in the original publications and reflects, to the best of my knowledge and understanding, their respective roles in the research.

In some cases (\*), the co-authors did not respond to the email addresses made available, nor to additional contact attempts through professional or academic social networks. In other instances (\*\*), no valid or current contact information—such as an institutional or personal email—could be located. Additionally (\*\*\*), in one case, the co-authors had retired and could not be reached despite extensive efforts.

#### DECLARATION 1

Hereby, we,

Co-authors of the below-mentioned article, attest that Marcelle Guedes de Medeiros Lopes played a prominent role in the scientific conceptualization and design of the study, implementation of the technical measurements and protocols, analysis and interpretation of the results obtained in the scientific research, as well as in the writing of the manuscript. Detailed contributions of each author for each article are presented below.


**Big Data in Transfusion Medicine and Artificial Intelligence Analysis for Red Blood Cell Quality Control. Transfus Med Hemother 27 June 2023; 50 (3): 163–173.** Marcelle G.M. Lopes, Steffen M. Recktenwald, Greta Simionato, Hermann Eichler, Christian Wagner, Stephan Quint, Lars Kaestner.

Marcelle GM Lopes and Steffen M Recktenwald, Conceptualization, Data curation, Formal analysis, Writing – original draft, Writing – review and editing; Greta Simionato, Methodology, Writing – review and editing; Hermann Eichler, Writing – review and editing; Christian Wagner, Resources, Writing – review and editing; Lars Kaestner, Conceptualization, Writing – original draft, Writing – review and editing; Stephan Quint, Supervision, Writing – review and editing.

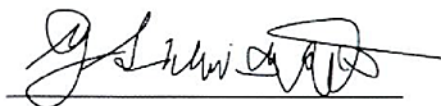
Date, Signature:

24.01.2025, 

Marcelle Guedes de Medeiros Lopes

30.01.25 

Steffen M Recktenwald



Greta Simionato

30.01.25 

Hermann Eichler

2.7.25 

Christian Wagner



Stephan Quint

5.3.25 

Lars Kaestner

## DECLARATION 2

Hereby, we,

Co-authors of the below-mentioned article, attest that Marcelle Guedes de Medeiros Lopes played a role in the implementation of the technical measurement, analysis and interpretation of the results obtained in the scientific research, as well as in the writing of the manuscript. Detailed contributions of each author for each article are presented below.

**Erysense, a Lab-on-a-Chip-Based Point-of-Care Device to Evaluate Red Blood Cell Flow Properties With Multiple Clinical Applications.** *Front. Physiol.* **13:884690.** (2022) Recktenwald SM, Lopes MGM, Peter S, Hof S, Simionato G, Peikert K, Hermann A, Danek A, van Bentum K, Eichler H, Wagner C, Quint S and Kaestner L

Steffen M Recktenwald, Conceptualization, Data curation, Formal analysis, Investigation; Methodology, Writing – original draft, Writing – review and editing; Marcelle GM Lopes; Formal analysis, Methodology, Writing – review and editing; Peter S, Investigation, Writing – review and editing; Hof S, Formal analysis, Writing – review and editing; Greta Simionato, Methodology, Writing – original draft, Writing – review and editing; Peikert K, provided blood samples and clinical data interpretation, Writing – review and editing; Hermann A, provided blood samples and clinical data interpretation, Writing – review and editing; Danek A, provided blood samples and clinical data interpretation, Writing – review and editing; van Bentum K, provided blood samples and clinical data interpretation, Writing – review and editing; Eichler H; provided blood samples and clinical data interpretation, Writing – review and editing; Christian Wagner, Resources, Funding acquisition, Writing – review and editing; Stephan Quint, Conceptualization, Data curation, Supervision, Investigation, Methodology, Writing – review and editing; Lars Kaestner, Conceptualization, Supervision, Writing – original draft, Writing – review and editing;

Date, Signature:

24.01.2025, 


Marcelle Guedes de Medeiros Lopes

30.01.25 

Steffen M Recktenwald

5.3.25 

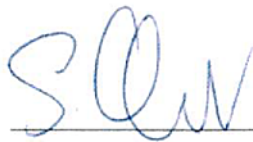
Lars Kaestner



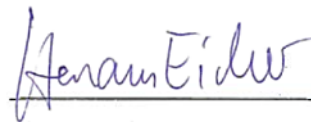
Greta Simionato

2.2.25 

Christian Wagner



Stephan Quint



Hermann Eichler

\*

Stephana Peter




Sebastian Hof

Kevin Peikert

Digital unterschrieben von  
Kevin Peikert  
Datum: 2025.02.05 07:29:23  
+01'00'

Kevin Peikert



Andreas Hermann

\*\*\*

Adrian Danek

\*

Kai van Bentum

### DECLARATION 3

Hereby, we,

Co-authors of the below-mentioned article, attest that Marcelle Guedes de Medeiros Lopes played a role in the implementation of the technical measurements and protocols, data analysis, as well as in the writing of the manuscript. Detailed contributions of each author for each article are presented below.

**Cross-talk between red blood cells and plasma influences blood flow and omics phenotypes in severe COVID-19** *eLife* 11:e81316 (2022). Steffen M Recktenwald, Greta Simionato, Marcelle GM Lopes, Fabia Gamboni, Monika Dzieciatkowska, Patrick Meybohm, Kai Zacharowski, Andreas von Knethen, Christian Wagner, Lars Kaestner, Angelo D'Alessandro, Stephan Quint

Steffen M Recktenwald, Greta Simionato, Conceptualization, Data curation, Formal analysis, Investigation; Methodology, Writing – original draft, Writing – review and editing; Marcelle GM Lopes; Data curation, Methodology, Writing – review and editing; Fabia Gamboni, Monika Dzieciatkowska, Data curation; Formal analysis, Writing – review and editing; Patrick Meybohm, Resources, Writing – review and editing; Provided blood samples and clinical data interpretation; Kai Zacharowski Resources, Writing – review and editing; Provided blood samples and clinical data interpretation; Andreas von Knethen, Resources, Writing – review and editing, Provided blood samples and clinical data interpretation; Christian Wagner, Resources, Funding acquisition, Writing – review and editing; Lars Kaestner, Conceptualization, Writing – review and editing; Angelo D'Alessandro, Resources, Formal analysis, Supervision, Funding acquisition, Writing – review and editing; Stephan Quint, Conceptualization, Data curation, Supervision, Investigation, Methodology, Writing – review and editing.

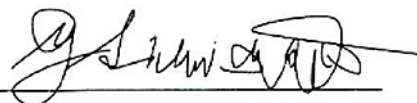
Date, Signature:

24.01.2025, 

Marcelle Guedes de Medeiros Lopes

30.01.25 

Steffen M Recktenwald



Greta Simionato

\*\*

Fabia Gamboni

01/31/2025 MONIKA DZIECIATKOWSKA

Monika Dzieciatkowska



\*\*

---

Patrick Meybohm

\*\*

---

Kai Zacharowski

\*\*

---

Andreas von Knethen

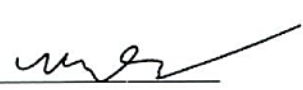
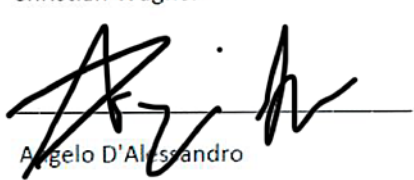
---

Christian Wagner

5.3.25   

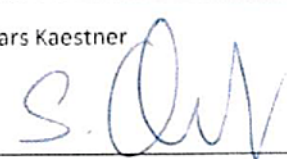
---

Lars Kaestner

2.2.25   
  

---

Angelo D'Alessandro

---

Stephan Quint

#### DECLARATION 4

Hereby, we,

Co-authors of the below-mentioned articles attest that Marcelle Guedes de Medeiros Lopes contributed specifically to the methodology section during the revision requests after the paper submission. Detailed contributions of each author for each article are presented below. Detailed contributions of each author for each article are presented below.

**A deep learning-based concept for high throughput image flow cytometry. *Appl. Phys. Lett.* 22 March 2021; 118 (12): 123701.** Julie Martin-Wortham, Steffen M. Recktenwald, Marcelle G. M. Lopes, Lars Kaestner, Christian Wagner, Stephan Quint

Julie Martin-Wortham, Data curation, Formal analysis, Investigation; Methodology, Writing – original draft, Writing – review and editing; Steffen M. Recktenwald, Data curation, Writing – review and editing; Marcelle G. M. Lopes, Methodology, Writing – review and editing; Christian Wagner, Resources, Funding acquisition, Writing – review and editing; Lars Kaestner, Supervision, Writing – review and editing; Stephan Quint, Conceptualization, Data curation, Supervision, Investigation, Methodology, Writing – original draft, Writing – review and editing.


Date, Signature:

24.01.2025, 

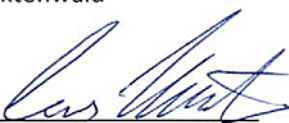
\_\_\_\_\_  
Marcelle Guedes de Medeiros Lopes

30.01.25 

\_\_\_\_\_  
Steffen M Recktenwald

2.2.25 

\_\_\_\_\_  
Christian Wagner

5.3.25 

\_\_\_\_\_  
Lars Kaestner

\*  
\_\_\_\_\_

\_\_\_\_\_  
Stephan Quint

31/03/2025 

\_\_\_\_\_  
Julie Martin-Wortham





## **Declaration on the use of translation assistance tools**

I declare that I used translation and language assistance tools, such as ChatGPT [1] and DeepL Translator [2], to support the writing of this thesis, given that English is not my native language. These tools were used solely to assist with translation and to improve the clarity and coherence of the text. All technical, scientific, and intellectual content is entirely my own work.



# Contents

<b>Eidesstattliche Erklärung</b>	<b>V</b>
<b>Abstract</b>	<b>VII</b>
<b>Zusammenfassung</b>	<b>IX</b>
<b>List of author's publication</b>	<b>XI</b>
<b>Declaration of author contributions</b>	<b>XIII</b>
<b>Declaration on the use of translation assistance tool</b>	<b>XXI</b>
<b>1 Introduction</b>	<b>1</b>
1.1 Generalities on blood . . . . .	1
1.2 Red Blood Cells . . . . .	2
1.2.1 Behavior in microcapillaries flow . . . . .	2
1.2.2 RBC deformability as a biomarker . . . . .	3
1.2.3 Pathologies . . . . .	4
1.2.4 Stored Blood . . . . .	12
1.2.5 Artificial Intelligence . . . . .	15
<b>2 Materials and Methods</b>	<b>27</b>
2.1 Sample preparation . . . . .	27
2.2 Deoxygenation stage . . . . .	29
2.3 Microfluidic chips preparation . . . . .	30
2.4 Microfluidics experiment . . . . .	31
2.5 Tracking and cropping toolbox . . . . .	32
<b>3 Results</b>	<b>37</b>
3.1 Methodology development . . . . .	37
3.1.1 RBC shape miniaturization . . . . .	37
3.1.2 Variational Auto-Encoder (VAE) . . . . .	40
3.1.3 CNN-based decision tree . . . . .	42
3.1.4 Transfer-learning . . . . .	48
3.1.5 Training and validation set . . . . .	50

3.1.6	Training and validation metrics . . . . .	53
3.2	Biological Investigation . . . . .	57
3.2.1	Control . . . . .	58
3.2.2	COVID-19 . . . . .	62
3.2.3	Sickle Cell Disease . . . . .	68
3.2.4	Neuroacanthocytosis syndromes . . . . .	73
3.2.5	Huntington's Disease . . . . .	76
3.2.6	Stored blood . . . . .	80
<b>4</b>	<b>Discussion</b>	<b>85</b>
4.1	Impact of RBC Morphology on Microcapillary Flow during COVID-19	86
4.2	Insights into RBC Behavior in Sickle Cell Disease . . . . .	91
4.3	Biomechanical RBC properties in Neuroacanthocytosis syndrome compared to Huntington's disease . . . . .	93
4.4	Assessing RBC Shapes in Microfluidic Flow for Stored Blood . . . .	95
<b>5</b>	<b>Conclusion and outlook</b>	<b>99</b>
5.1	Future prospects . . . . .	102
	<b>Bibliography</b>	<b>103</b>
	<b>Acknowledgments</b>	<b>115</b>

# 1 Introduction

This introduction chapter aims to provide a comprehensive summary of the thesis, offering an overview of its primary content while highlighting significant findings derived from existing literature.

## 1.1 Generalities on blood

Blood is a vital bodily fluid that performs several functions, including transportation, regulation, and protection [3]. It constantly circulates throughout the body, carrying oxygen, carbon dioxide, nutrients, hormones, heat, and waste products. Additionally, it regulates the pH, protects against blood loss by clotting and diseases through phagocytic leukocytes, antibodies, and interferons. The average temperature of blood is about 37°C, and it has a slightly alkaline pH between 7.35 and 7.45. Its composition is given by 4 elements **(i)** plasma, **(ii)** red blood cells (RBCs), **(iii)** white blood cells (WBCs), and **(iv)** platelets.

- (i) Making up 55% of blood, plasma is the largest component and comprises approximately 90% of the blood's volume. It is composed of 90% water, 9% proteins, and 1% electrolytes. The primary role of plasma is to transport blood cells throughout the body along with various substances such as nutrients, waste products, antibodies, coagulation proteins, and chemical messengers.
- (ii) Red blood cells (RBCs) are the primary cellular component of blood. They lack a nucleus and organelles, and have a biconcave discocyte shape with a diameter ranging from 7 to 8  $\mu m$  and thickness of approximately 2  $\mu m$ . This shape is highly deformable, enabling them to pass through various blood vessels. However, the lack of a nucleus limits their lifespan, as this impairs their capacity for self-repair and renewal, especially as they traverse the smallest blood vessels and suffer membrane damage. On average, RBC have a lifespan of around 120 days before they are broken down within the bone marrow, spleen, or liver. After circulating through the body and undergoing gradual cell membrane degradation, the phagocytic cells in the spleen and liver detect the altered appearance of aging or non-viable RBCs. Subsequently, these

cells are eliminated from circulation through phagocytosis. Furthermore, the RBC owe their characteristic red color to hemoglobin, a specialized protein responsible for transporting oxygen around the body.

- (iii) White blood cells make up approximately 1% of the blood and are crucial for the immune response as they combat bacterial, viral, parasitic, or fungal infections.
- (iv) Platelets, despite being much smaller than red blood cells, are essential for blood clotting. They accumulate at the site of injury, adhere to the lining of the damaged blood vessel, and form a fibrin clot that seals the wound and stops bleeding.

## 1.2 Red Blood Cells

### 1.2.1 Behavior in microcapillaries flow

RBCs flow in a complex network of branching blood vessels throughout the human body at different velocities and scales. Their behavior in large blood vessels can be approximated as a homogeneous fluid due to their lower volume fraction [3]. However, in contrast to this, in microcapillaries, the flow of RBCs cannot be regarded as a homogeneous fluid since the blood contains a high concentration of suspended cells, including highly deformable RBCs as shown in [3]. Moreover, the RBC microcirculation is mainly responsible for nutrient uptake and delivery [4] and gas exchange between blood and tissues [5], and RBCs' remarkable deformability enables them to flow through microcapillaries whose dimensions are comparable to their own size.

Microfluidic devices offer an efficient approach to investigate the flow behavior of a single-cell in microcapillaries. Such behavior has been demonstrated to be dependent on confinement conditions in several instances, as shown in numerical simulations [6,7], and in vitro experiments [4,5,8]. Mathematical models were used to simulate various microflow conditions for fluid flow around RBCs, revealing that RBCs exhibit both symmetric and asymmetric shapes. The cause of this deformation in RBCs was hypothesized to be the result of interactions between the elastic properties of the lipid bilayer and cytoskeleton, as well as the flow conditions within the microcapillary, as stated in [7].

The study of bistability between symmetric and asymmetric RBC shapes was extensively carried out in [6]. A combination of microfluidic experiments and numerical simulations was used to mimic a constant flow with velocities ranging from 0.1

to 10 mm/s in a rectangular microfluidic channel with a height of  $10\ \mu\text{m}$  and a width of  $12\ \mu\text{m}$ . The study revealed that at low velocities, RBCs tend to take on a symmetrical and centered shape with a concave front and a convex back, referred to as a croissant. However, at higher flow rates, RBCs adopt an asymmetric and off-centered shape with a pointed front and a flat rear, referred to as a slipper. The transition between croissants and slippers has also been studied, as shown in [4] and the images of both stable forms obtained from experiments and simulations conducted on it are displayed in Figure 1.1.

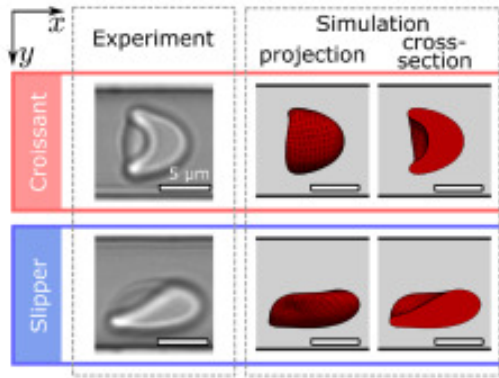


Fig. 1.1: The images in the experiment display Croissant-shaped and slipper-shaped RBC, which are followed by simulation images generated under identical conditions. The RBC flow direction is in the x-axis, and the scale bars correspond to a length of  $5\ \mu\text{m}$ . Taken from [4].

Together with numerical simulations, in vitro experiments using a rectangular-section microfluidic channels (30 parallel channels with a width of  $10.8\ \mu\text{m}$ , a height of  $7.9\ \mu\text{m}$  and a total length of  $40\ \mu\text{m}$ ) were used for pressure drops ranging from 200 to 1000 mbar, and with increasing and decreasing pressure ramps to achieve the RBC shape transition. The investigation of the shape evolution of the cells as they travel through the microchannel resulted in the observation of various shape transitions such as elongation, deformation, rotation, and tumbling under different flow conditions, justified depending on the flow rate and the amplitude and frequency of flow fluctuations.

### 1.2.2 RBC deformability as a biomarker

The velocity of RBCs and the characteristics of the surrounding medium affect their shape [6, 9] in microcirculation. These shapes are determined by intrinsic factors such as cytoplasmic viscosity, cytoskeleton properties, and membrane rigidity [9]. Pathological alterations in RBC deformability have been linked to changes in these

factors [10, 11]. Such pathological changes in the RBCs deformability can be observable, for example, in inflammatory responses in COVID-19 [12], malaria [13], sickle cell anemia [14], diabetes [11, 15], hereditary disorders [11, 16], myocardial infarction [11], [17], and storage lesions [9] caused by blood storage.

Changes in the mechanical properties of RBCs, such as their cytoplasmic viscosity and bending stiffness, can significantly impact their shape, decrease of microvascular perfusion, and blood flow behavior, causing harm to the endothelial cells lining blood vessels. Even in stasis, the shape of the RBC is a highly sensitive parameter [18]. When combined with information on capillary flow, which can detect abnormalities [19], RBC flow properties can serve as a biomarker with broad applications, including undiagnosed or challenging-to-diagnose diseases, known diseases, monitoring patient therapy, or in vitro treatment tests [9] as outlined in the next sections.

### 1.2.3 Pathologies

#### Coronavirus disease 2019 (COVID-19)

Severe acute respiratory syndrome coronavirus 2 (SARS-CoV-2) causes COVID-19, which is an acronym for corona virus disease first identified in 2019. COVID-19 is an extremely contagious respiratory disease that spreads mainly through contact, droplets, and potentially through the air. To diagnose COVID-19, healthcare professionals look for typical symptoms like fever, respiratory issues, abnormalities in chest computed tomography (CT) scans, and conduct polymerase chain reaction (PCR) testing [20]. As of August 2023, the disease has caused over 760 million confirmed cases and more than 6.9 million deaths worldwide [21, 22]. Up to 15% of individuals infected with COVID-19 [23] can experience acute respiratory illness and hypoxia, which may require hospitalization. Among these patients, some may develop acute respiratory distress syndrome (ARDS) and multiple organ failure (MOF), and even die. COVID-19 can present with various hematologic manifestations, such as the disruption of the balance and stability of the RBC membrane structure, as suggested in [24]. The disruption is evident by increased levels of glycolytic intermediates, substances involved in energy production, within the RBCs. Additionally, the membrane proteins of RBCs undergo chemical alterations, oxidation, and fragmentation. These changes indicate that COVID-19 significantly affects the integrity and function of the RBC membrane, potentially leading to impaired oxygen transport and delivery. Furthermore, this disruption may contribute to microvascular coagulation, as noted in [25].

Several studies [26–28] have highlighted the impact of altered iron metabolism on



RBCs in COVID-19 patients. These individuals may exhibit elevated levels of ferritin, a protein involved in iron storage. Increased ferritin levels are often indicative of a robust inflammatory response and are associated with longer hospital stays, a higher risk of ICU admission, and an increased likelihood of requiring mechanical ventilation. These findings emphasize the significant role of iron metabolism changes in COVID-19 and their implications for patient outcomes.

Additionally, according to [29], COVID-19 has a direct impact on hemoglobin within the bone marrow. The virus specifically targets the precursor cells of RBCs in the bone marrow and interacts with specific receptors on RBCs and their precursors. This interaction leads to viral entry and affects the iron-containing heme molecule in hemoglobin. Specifically, the virus targets and interacts with the  $\alpha$ -chain of hemoglobin with the intention of separating iron from it, subsequently forming protophyrin. This disruption in hemoglobin function can potentially contribute to hemolysis, leading to the destruction of RBCs and the formation of dysfunctional hemoglobin. Given the significant impact of COVID-19 on the cardiovascular system and the urgent need for reliable biomarkers to assess disease progression and identify high-risk patients, hematological biomarkers hold great importance for screening, managing patients, and preventing severe complications [30]. Specifically, deformability in RBC shapes has shown promise as a potential biomarker, as demonstrated by a study conducted in [31]. In this research, blood samples obtained from healthy individuals, COVID-19 patients at various stages of severity, and individuals who had recovered from the disease were subjected to real-time deformability cytometry (RT-DC) using a microfluidic device. The study observed notable alterations in the morphology of blood cells, particularly RBCs, which exhibited changes in shape and size. These findings not only highlight the enduring effects of COVID-19 on the body but also suggest that morphological analysis of RBCs can serve as a fast and sensitive approach to detect functional changes in cells. Such analysis holds potential as a biomarker for COVID-19 and other infectious diseases.

Also thinking about the shape of RBC as a possible biomarker for COVID-19, Recktenwald *et al.* [12] investigated the potential of RBC shape as a biomarker for severe COVID-19 and its implications for blood flow and omic phenotypes. Proteomic analyses, focused on identifying and characterizing proteins, along with metabolomics, which examines small molecules involved in cellular processes, were conducted to explore the reciprocal interactions between RBCs and plasma in individuals with COVID-19. Using microfluidic devices, we conducted experiments and observed significant morphological changes, such as irregularities and spiculated shapes, in RBCs from patients with severe COVID-19. These abnormal RBC shapes founded, could contribute to impaired blood flow and microcirculation, resulting in tissue hypoxia and organ dysfunction [12]. The study emphasizes the

importance of understanding the interplay between RBCs and plasma in severe COVID-19 and suggests that alterations in RBC shape may play a role in the disease's pathophysiology. Additionally, the findings suggest that RBC shape changes could potentially serve as a biomarker for risk stratification, enabling timely treatment interventions.

### Neutoacanthocytosis Syndromes

Neuroacanthocytosis Syndromes (NAS) comprises a cluster of hereditary neurodegenerative conditions marked by acanthocytosis, a RBC abnormality [32], [33] that is shown in Figure 1.2. Indeed, [34] showed that the majority of NAS patients show acanthocytosis on a peripheral blood smear at some stage during the disease, with 10-30% of erythrocytes displaying a distinctive spiky appearance that aids in diagnosing the disease. The prevalence of NAS is extremely low, with estimates ranging from less than 1 to 5 cases per 1,000,000 population [35].

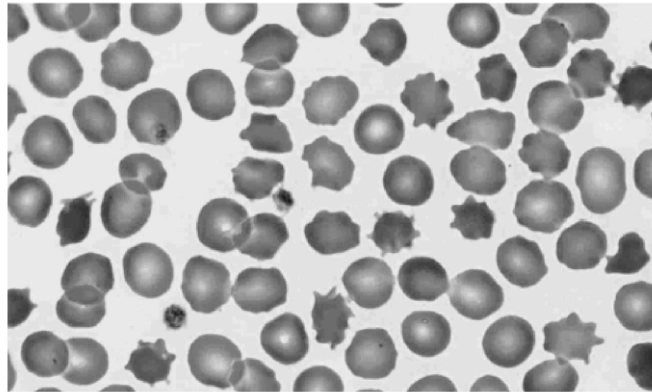


Fig. 1.2: The figure shows the presence of acanthocytes in a blood smear obtained from a patient diagnosed with McLeod's neuroacanthocytosis syndrome. Taken from [33].

Chorea-acanthocytosis (VPS13A-disease) [36] and McLeod syndrome (XK-disease) [37] are part of the NAS, with approximately one thousand cases reported worldwide. VPS13A-disease is most prevalent in Japan and among the French-Canadian population [35], while XK-disease cases are distributed across Europe, the Americas, and Japan [35], totaling several hundred individuals affected. As described in [32], Chorein, a 360-kDa protein, is coded by the VPS13A gene on chromosome 9, and mutations in this gene cause the autosomal recessive disorder VPS13A-disease.

While mature RBCs contain Chorein, it is either partially or entirely absent in VPS13A-disease RBCs. VPS13A-disease symptoms include chorea, dystonia, parkin-

sonism, as well as cognitive and psychiatric symptoms. On the other hand, XK-disease is a condition that affects the hematologic, neuromuscular, and central nervous systems caused by a mutation in the XK gene located on the X chromosome. The XK protein plays a crucial role in the expression of the Kell blood group antigen on RBCs, leading to reduced expression in XK-disease and resulting in compensated hemolytic anemia. Most affected individuals are males who experience chorea, cognitive impairment, and psychiatric symptoms beginning in adulthood, with a decrease in abnormal involuntary movements after VPS13A-disease diagnosis, according to [33]. As highlighted in [38], the clinical diagnosis for VPS13A-disease and XK-disease is established by detecting increased levels of acanthocytes in peripheral blood smears.

The specific mechanisms by which NAS affects changes in RBC morphology are still not fully understood. Research has revealed a lack of comprehensive knowledge regarding the connection between NAS progression and hematologic factors, such as the formation of acanthocytes. However, it is established that the reduction in the deformability capacity of RBCs, directly associated with an increased rigidity of their membranes, contributes to the hematological alterations observed in NAS, as indicated by several studies [35, 39, 40]. In a study conducted by Reichel *et al.* [39], microfluidic devices and flow cytometry were employed to assess and quantify RBC deformability in individuals with NAS. The findings revealed that acanthocytes exhibit decreased deformability within the bloodstream. This reduced deformability not only compromises the survival of the affected cells but also leads to impaired oxygenation of other tissues in the body, decreasing oxygen delivery, particularly in sensitive areas of the brain [39, 41]. Furthermore, Rabe *et al.* [40] proposed the use of erythrocyte sedimentation rate (ESR) as a diagnostic biomarker. In his study, they demonstrated not only the altered rigidity of acanthocytes present in NAS patients' RBCs but also in the healthy shapes of RBCs found in their blood. By employing the standard Westergren method and microfluidic devices, they confirmed that the healthy RBCs of NAS patients exhibited higher rigidity compared to healthy donors. Moreover, they observed a higher degree of sedimentation in NAS samples and suggested the sedimentation rate after 2 hours as a diagnostic biomarker. They also revealed that the transition point between the crescent and slipper shapes of RBCs was delayed in patients with NAS. In addition, Recktenwald *et al.* combined microfluidic channels and artificial intelligence, demonstrating promising results in the diagnosis of NAS [9] ( See section Author's declaration of contributions, DECLARATION 2.). The study showed that samples from both VPS13A-disease and XK-disease patients exhibit acanthocytes during flow, and the RBC flow properties of samples affected by NAS are different from healthy controls by calculating what the authors called as "shape-ratio". Through the confirmation of distinct shape ratios between NAS patients and healthy individuals, as well as the presence of pathological forms of RBC that are not documented

in the literature, a novel biomarker for diagnosing NAS was proposed: RBC deformability. These findings suggest a potentially functional characterization tool or even a new biomarker for NAS interventional studies.

The impaired deformability of RBC in NAS patients is affected by treatments, highlighting the importance of monitoring the mechanical properties of blood cells during disease progression and potential therapies [39]. This monitoring can enhance the understanding of the disease. While clinical descriptions of NAS often prioritize neurological symptoms, the effects on blood cell deformability should not be disregarded, as they may contribute to clinical manifestations. Therefore, methods capable of evaluating these effects should be considered crucial parameters in clinical trials. Currently, there are no available curative or disease-modifying treatments for NAS, and treatment remains focused on managing symptoms. However, with appropriate measures, the life expectancy and quality of life of patients can be significantly improved.

### **Huntington's disease**

Huntington's disease (HD) is a genetic disorder caused by a mutation in the huntingtin gene that results in the production of an abnormal protein, leading to the death of neurons in the brain. Based on data from the European Medicines Agency (EMA), the estimated prevalence of Huntington's disease in the European Union is approximately 1.2 cases per 10,000 individuals [42]. This suggests that there are approximately 62,000 people affected by this condition within the EU. Symptoms of HD include involuntary movements, cognitive and psychiatric disturbances, and motor difficulties. Distinguishing between Huntington's disease and the NAS is challenging due to similarities in symptoms and imaging findings [43, 44]. Acanthocytes in peripheral blood have been used to support the diagnosis of NAS [45]. However, recent studies [46] have suggested that HD patients may also exhibit altered RBC morphology that is sometimes confused with acanthocytosis. This ambiguity can be observed in the study conducted by Yu *et al.* [46], which used scanning electron microscopy to investigate the RBCs of Huntington's disease patients displaying atypical shapes. The study revealed that HD can affect RBCs, leading to abnormalities such as oxidative damage, an increased number of stomatocytes, and the formation of cells with membrane deformations that sometimes resemble acanthocytes and echinocytes, as shown in Figure 1.3. On the other hand, [47] utilized flow cytometry and blood smears to find that the count of acanthocytes in both HD patients, HDL2, and control subjects remained below the normal threshold. This implies that the creation of acanthocytes does not play a significant role in these diseases. Both researches indicate that abnormal RBC shapes can occur with HD, but its development is still unclear as it may be in-

fluenced by specific genetic or environmental factors. Moreover, they emphasized that it is necessary to regularly monitor the blood morphology of patients as it can change over time.

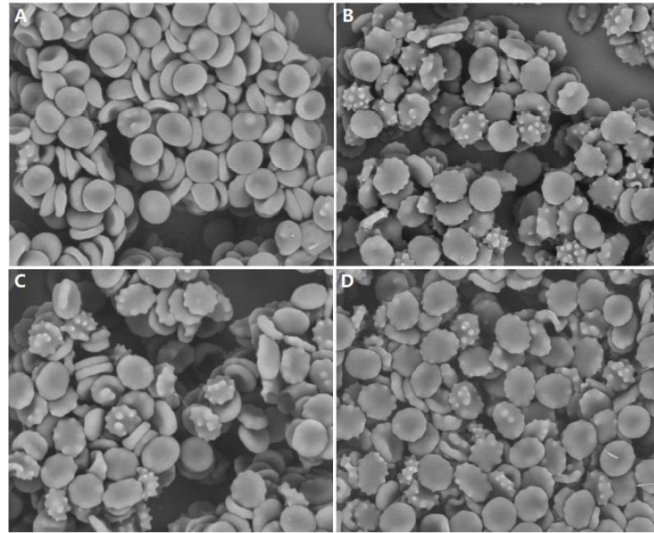


Fig. 1.3: Scanning electron microscopy examination of fresh peripheral blood samples from four patients (A, B, C, and D) revealing the presence of echinocytes. Observed at a magnification of x1800. Taken from [46].

Continuing the discussion about the complexity surrounding the pathological shapes of RBCs observed in HD, Peikert *et al.* [48] commented that this confusion has been documented in the past. For years, efforts have been made to clarify this issue, especially concerning the presence of acanthocytes as a means of classifying and diagnosing HD. They also referenced the recommendations provided by the International Council for Standardization in Hematology regarding the visual classification of stained blood films [49]. While less precise, these recommendations have paved the way for automation in diagnosis (as proposed by Kamentsky [50]). The objective is to streamline this often intricate and time-consuming classification process typically carried out by human observers.

To this day, there is still no cure for HD, and the available therapeutic strategies primarily address the symptoms. The current treatment approach aims to manage motor, cognitive, and psychiatric symptoms, with the ultimate objective of enhancing the quality of life for individuals affected by this condition. The pursuit of biomarkers is gaining significance in the context of Huntington's disease (HD), despite the current limitations in treatment and the emphasis on symptom management. This is exemplified by the work of Podlacha *et al.* [51], who conducted a

study utilizing R6/1 mice, a model that exhibits characteristics similar to HD in humans. The study aimed to analyze blood biomarkers in these mice with the objective of identifying indicators that could be translated into clinical settings for the diagnosis and monitoring of HD. Podlacha *et al.* suggested that blood biomarkers, such as gene expression profiles, protein markers, and metabolites, hold immense potential for detecting HD-related changes. These biomarkers could serve as valuable tools in the identification and tracking of the disease's progression, offering insights for clinical applications.

### Sickle cell disease

Sickle cell disease is attributed to the production of Hemoglobin S (HbS), a type of hemoglobin protein that arises from a substitution of nucleotide in the gene responsible for  $\beta$ -hemoglobin synthesis [52]. When HbS molecules are deoxygenated in the microcirculation, they undergo polymerization by associating hydrophobic residues of HbS molecules with adjacent molecules, forming rigid fibers that distort and damage the RBC membrane and cytoskeleton [53, 54]. The repeated damage caused by the crystallization leads to the formation of irreversibly sickled cells, hemolysis, and imparts biomechanical properties to the RBC that contribute to the vaso-occlusions commonly seen in sickle cell disease (SCD). In [53] is proved that the shape of sickle RBCs is greatly influenced by the arrangement of the HbS crystal inside the cell, leading to a varied spectrum of cell morphologies. By using a technique to measure the alignment of hemoglobin fibers, it was demonstrated that there are at least four different classes of sickle cells: single domain cells, multiple domain cells, central constriction cells, and spherulite cells, as displays Figure 1.4. Single domain cells involve HbS fibers clustering into a single group of continuous fibers, while multiple domain cells have crystalized HbS fibers clustering in at least two clusters of continuous fibers. Central constriction cells have a few crystalized HbS fibers in the center of the cell, but these increase rapidly in number towards the edges of the cell in one direction, forming the dumbbell shape. Spherulite cells are similar to central constriction cells but differ in the direction of the spreading of the crystalized HbS fibers, occurring outward in multiple directions.

The diverse range of sickle cell shapes was assessed in [55] as a biomarker for diagnosing and monitoring SCD, recognizing that conventional techniques such as peripheral blood smears under hypoxic conditions can be both time-consuming and biased by the subject interpretation. The study also suggests utilizing a combination of microfluidic devices and automated classification of RBC morphologies as a reliable method to assess the impact of novel therapies on the morphology of individual sickle cell RBCs. This approach has been successfully demonstrated in other studies [56, 57]. Despite the advances in diagnosing SCD, the lack of an

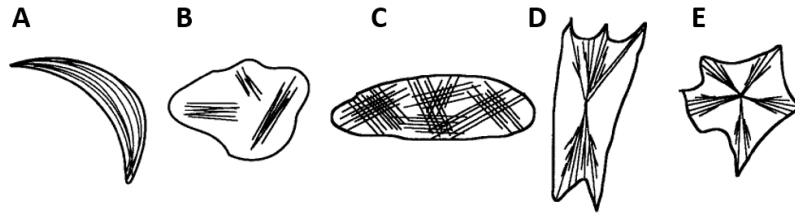


Fig. 1.4: Shows five different sickle cell shapes. (A) single domain cell, (B) three domain cell, (C) multiple domain cell, (D) central constriction cell, and (E) spherulite cell. Taken from [53].

objective method to measure clinical severity or prognosis, including the ability to predict vaso-occlusive crisis (VOC), is presently a major constraint, impairing even the drug development in SCD.

VOCs are responsible for approximately 95% [58] of hospitalizations related to SCD and contribute significantly to the disease's morbidity. These crises occur when sickle cells block capillaries, and their occurrence typically increases from 1 to 3 days before the onset of clinical symptoms. Despite the significant impact of VOC management on patients' lives, there is a lack of reliable methods to measure the severity and frequency of these crises. Darbari *et al.* [58] have identified several blood biomarkers, including higher neutrophil counts, platelet hyperactivity, hemolysis, and lactate dehydrogenase levels, that may indicate the severity of SCD. However, relying solely on these parameters is insufficient to predict the severity and frequency of VOCs. This limitation underscores the need for additional markers and a better understanding of the factors influencing VOCs. Identifying such markers would be crucial for identifying potential therapeutic targets and developing effective treatments for VOCs in SCD.

According to Ware *et al.* [59], the two most commonly used treatments for reducing symptoms of SCD are transfusion therapy and pharmacological induction of fetal hemoglobin (HbF). Transfusions are often given to adult patients, both for acute complications and as a long-term treatment. While transfusions provide immediate benefits by improving oxygen-carrying capacity and blood flow, they can lead to complications such as liver iron overload, which limits their long-term use. Hydroxyurea, approved by the Food and Drug Administration (FDA) in 1998 [60], is commonly used to increase HbF levels, making rounder and more flexible RBCs and resulting in reduced frequency of VOCs and the need for transfusions. However, there are multiple challenges impeding the utilization of hydroxyurea in individuals with SCD, and research has revealed that many patients struggle to adhere to this treatment, as discussed in [60] in their investigation of current and emerging therapies for SCD. Another treatment mentioned by Lynne *et al.* [60] is voxolotor, which

directly targets the polymerization of HbS, delaying the process of sickling. However, the most promising therapeutic approach is gene therapy and gene editing technologies, which offer the potential for a cure in SCD. Despite ongoing clinical trials [61, 62] and considerable promise, gene therapy still faces technological and regulatory challenges and is likely to be an expensive treatment option.

Treating SCD can be particularly costly for severe patients that experiences recurrent VOC. As stated in [60], VOC constitutes over 90% of acute hospital admissions and 85% of all acute medical care provided to individuals with SCD. The lifetime hospital expenses for patients with severe cases range from approximately 461,000 € to nearly 8.3 € million. Additionally, the costs associated with transfusions can amount to 55,000 € per year. These numbers further underscore the necessity for affordable, reliable, accurate, robust, and accessible characterization devices to maximize outcomes in SCD.

#### 1.2.4 Stored Blood

Around 85 million units of stored RBCs are transfused annually worldwide [63], with Europe accounting for 26% of global donations in 2018 according to the WHO Global Status Report on Blood Safety and Availability [64]. To ensure the safety and quality of blood products, Europe follows the standards set by the European Union's 2004 regulation (Directive 2004/23/EC) [65]. This regulation outlines specific requirements for the collection, processing, testing, storage, and distribution of blood and blood components. Its aim is to safeguard the recipients of blood transfusions and minimize associated risks. The regulation emphasizes various measures to achieve these goals. It imposes the proper identification of each blood unit throughout the donation-to-administration process. Rigorous screening and testing of blood donors for bloodborne diseases such as HIV, hepatitis B and C, and syphilis are also essential. The regulation establishes clear guidelines for the processing and storage of blood units to maintain their quality. Another significant aspect of the regulation focuses on quality assurance for blood products. It includes the standardization of procedures for processing, storage, and distribution of blood bags. Additionally, the regulation mandates the performance of laboratory tests to ensure the integrity, purity, and viability of the collected blood components. Overall, the regulation plays a crucial role in ensuring the safety, quality, and traceability of blood products in Europe, with a comprehensive framework covering various aspects of blood transfusion processes.

The World Health Organization (WHO) has recommended the standardization of "blood cold chain equipment" in its Manual on the management, maintenance, and use of blood [66]. According to the manual, after donation, RBCs are separated



from other blood components and should be stored in a specialized bag. This bag contains an additive solution that includes essential anticoagulants to prevent blood clotting. The recommended storage temperature for RBCs is between +2 °C to +6 °C, ensuring the preservation of their quality and effectiveness. Blood units can be stored for up to 42 days, but on average in Europe, they are transfused to patients by the 16<sup>th</sup> day of storage, as observed in the study by Relevy *et al.* [67]. However, a significant percentage of units, reaching 37%, are still transfused after the 3<sup>rd</sup> week of storage, according to [67,68]. This indicates that a considerable number of blood units undergo extended storage before being administered to patients.

Another significant regulation that focuses on ensuring the integrity, purity, and viability of blood units is REGULATION (EU) 2017/745 OF THE EUROPEAN PARLIAMENT AND OF THE COUNCIL [69]. This regulation specifically addresses the design and manufacturing of blood bags to minimize the release of harmful substances into the RBC. According to Larsson *et al.* [70], the commonly used blood bags for storing RBCs are typically made of polyvinyl chloride (PVC) plasticized with di(2-ethylhexyl) phthalate (DEHP). DEHP is released when it comes into contact with stored blood components and becomes incorporated into the RBC membrane, contributing to its integrity. However, concerns regarding the toxicity of DEHP have prompted regulations to limit its concentration in blood bags. The DEHP regulation [69] stipulates that the maximum permissible concentration of DEHP in a blood bag should not exceed 0.1% weight/weight. Consequently, there is a growing interest in replacing DEHP with a non-toxic plasticizer in blood bags, as long as this substitution does not compromise the quality of the blood components.

Continuing with the focus on maintaining the integrity, purity, and viability of blood units, another crucial factor to consider is the additive solution (AS). The AS plays a vital role by providing essential nutrients like glucose, adenine, and salts to support the metabolism and viability of RBCs during storage. According to WHO [66], RBCs can be stored for a duration of up to 42 days (6 weeks) in the AS. However, Chen [71] explains that although the AS helps in preserving RBCs, it alone is not sufficient to maintain their integrity, leading to their rupture. The changes and degradation that occur in RBCs from the initial blood collection to the rupture of their membrane are referred to as storage damage [71]. In our body, RBCs derive their energy from the anaerobic metabolism, but when they are separated and stored, they rely on the nutrients provided by the AS. However, this process gradually changes the pH of the solution, impacting the production of Adenosine triphosphate (ATP) and impairing the RBC's ability to counter oxidative damage. The acidification of RBCs and the decrease in ATP levels have observable effects on their shape, as highlighted in [66], where the formation of spherocytocytes is observed instead of the characteristic biconcave disc shape.

Figure 1.5 shows the spheroechinocytes described in [71].

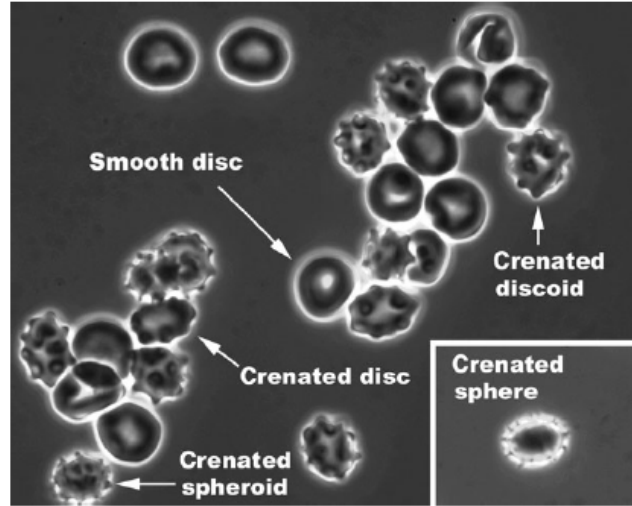


Fig. 1.5: It shows the healthy shape of the RBCs as smooth discs, and the appearance of spheroechinocytes on day 23 of storage at 4°C in SAGM. Taken from [71].

Although SAGM (saline-adenine-glucose-mannitol) is widely used as an AS in Europe, it leads to a decrease in ATP levels during cold storage, which can result in storage lesions. However, a new generation of AS solutions has emerged to address this issue and maintain the biochemical parameters of RBCs. Lagerberg *et al.* [72] highlights AS-7 (Additive Solution 7), phosphate-adenine-glucose-guanosine-gluconate-mannitol (PAG3M), and Erythro-Sol (E-Sol) as innovative AS solutions that can effectively mitigate the decline in RBC quality parameters in vitro, potentially improving the safety and efficacy of transfusions. They conducted a study comparing SAGM, PAGGSM, PAG3M, E-Sol 5, and AS-7 for 56 days of cold storage, monitoring the occurrence of storage lesions on a weekly basis. The study not only demonstrated that PAG3M, E-Sol-5, and AS-7 exhibited significantly higher levels of key ATP metabolites compared to control RBCs stored in SAGM, indicating a reduced development of storage lesions, but also discussed the use of DEHP in the bags. It is to be noted that the current AS may not be suitable for use with DEHP-free plastics. Therefore, replacing SAGM with the new generation of AS in DEHP-free systems could be a viable solution to enhance RBC preservation.

Moreover, the development of storage lesions is followed by alterations in the aggregability and adhesion of RBCs to the endothelial cells lining the inner walls of blood vessels. These changes disrupt the flow of RBC and can potentially harm transfusion recipients. Relevy *et al.* conducted a study [67] to investigate the im-

impact of storage on RBCs flow by observing changes in aggregability and adhesion of stored RBCs. Normally, healthy RBC flow is strong enough to disperse cell clusters. However, after storage, these cell aggregates become more resistant, increasing the risk of microcapillary vascular occlusion. This can result in insufficient tissue oxygenation, ischemia, and even infarction in recipients of these RBCs. The increased adherence of stored RBCs also heightens the risk of post-transfusion complications. While healthy RBCs exhibit minimal adhesion to endothelial tissue, stored RBCs adhere more strongly, impeding blood flow and preventing disaggregation. Relevy *et al.* measured the deformability, aggregability and adhesion to endothelial tissue of stored RBC every 7 days for a duration of 35 days, providing evidence that the flow properties of RBCs are impaired by storage as early as the second week.

Several studies [9, 39, 41, 43, 73] have shown an increasing focus on analyzing the damage to RBCs caused by storage lesions, with one identified form of impairment being the loss of RBC deformability. In [39], it shows that RBC membrane damage becomes noticeable after the second week and intensifies as storage time increases. Furthermore, [40] states that RBC exposure to plasticizers and oxygen during storage results in the accumulation of metabolic residues and subsequent acidification, which causes damage known as storage injury. Furthermore, [43] investigated the deformability of RBCs stored at 4°C for 8 weeks. Stored RBCs were sampled at different times (on the same day of collection and also at weeks 2, 4, 6 and 8) and were assessed for deformability using a microfluidic ratchet device and the stiffness score (SR). The authors observed a decrease in RBC deformability at the different time points, suggesting that the RBC deformability loss profile may be a useful biomarker for degradation. And they conclude that this finding could guide the selection of blood units for transfusion and help investigate challenges related to RBC product quality.

### 1.2.5 Artificial Intelligence

Artificial Intelligence (AI) is a multidisciplinary field that focuses on creating intelligent machines that can simulate human intelligence. It combines principles from statistics, computer science, technology, and neuroscience to develop systems capable of performing tasks that typically require human intelligence [74]. AI techniques encompass a wide range of strategies, including decision trees, "if-then" rules, and machine learning algorithms. Machine learning (ML) is a specialized branch of AI that empowers computers to recognize and analyze patterns and correlations within datasets. ML algorithms are designed to learn from the data they are exposed to, enabling them to improve their performance and make accurate predictions or decisions. A subfield of ML, called Neural networks, have garnered significant attention for their remarkable success in diverse domains. Inspired by

the structure and functionality of biological neural networks, these networks consist of multiple layers that enable the learning of complex and abstract representations. By leveraging this architecture, neural networks have demonstrated their effectiveness in medical applications [75]. Figure 1.6 illustrates the different levels of artificial intelligence, culminating in the neural networks.

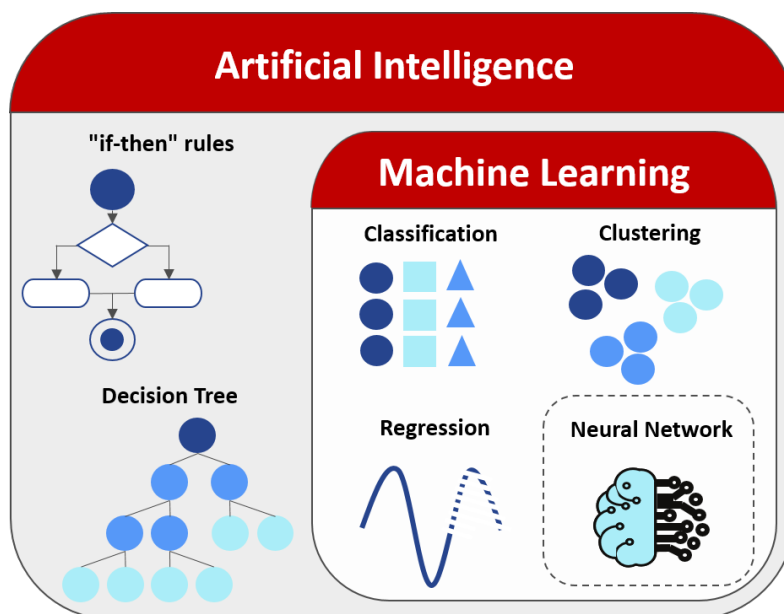


Fig. 1.6: The relationship between artificial intelligence, machine learning and neural networks.

ML has made significant advancements in hematology, with positive impacts across patient management, from diagnostic predictivity to personalized treatments based on genetic profiling [76]. The field of hematology has witnessed progress in quantitative techniques, particularly in the parameterized description of RBC shapes, which has advanced through methodological developments and clinical trials. These techniques when used to RBC flow analysis, 2D and 3D RBC shape analysis, erythrocyte sedimentation rate (ESR) calculation, and elongation index (Elmax) calculation, contribute to achieving a higher level of RBC disease diagnosis. When combined with AI, point-of-care (PoC) devices can monitor therapy progress and adjust treatments. As described by Kaestner [76], AI and ML have become integral to the professional life of healthcare practitioners, working alongside doctors in data generation, analysis, and the integration of hematological parameters. This collaborative approach provides a fresh perspective on individual patient health and holds implications for public health systems.

## Artificial Neural Network

Artificial Neural networks (ANN) are software programs that are inspired by the structure and function of the human brain, allowing computers to learn and make decisions in a human-like manner. The Artificial Perceptron Neural Network [77] is the earliest model, capable of handling linearly separable problems, using a single “artificial neuron” called perceptron, nodes or units. In the human brain, neurons receive external stimuli through their dendrites, process the information in the cell body, convert it into an output, and transmit it along the axon to the next neuron.

The transmission of a signal from one neuron to the next takes place through a functional connection known as a synapse. Within the synapse, the next neuron’s response hinges on the intensity of the received signal, determining whether it is accepted or rejected. In artificial neurons, this process is mathematically represented, with inputs corresponding to the dendrites, units representing the cell body, weights representing the synapses, and the output representing the axon, as show in Figure 1.7.

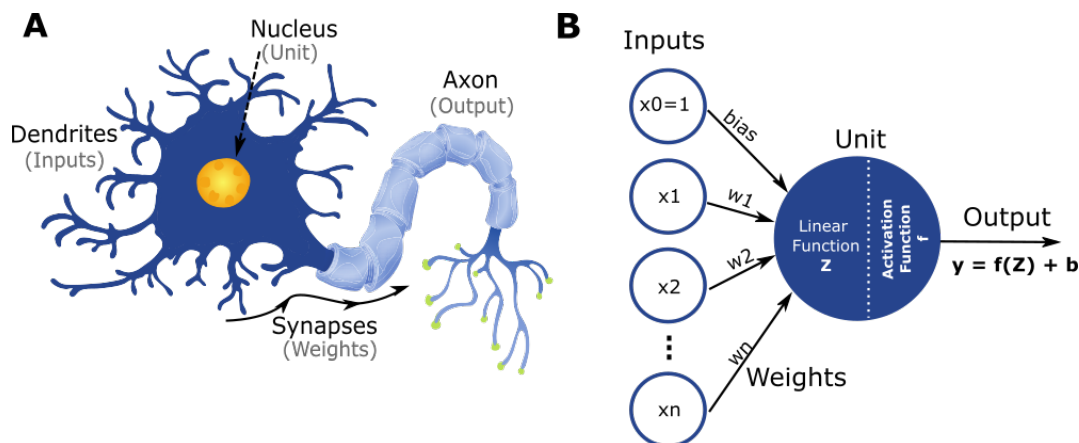


Fig. 1.7: (A) Biological neurons receive input stimuli from other neurons through dendrites and process them before transmitting the information through the axon to synapses, where connections with other neurons are formed. (B) In an artificial neuron, the inputs ( $x_1, x_2, \dots, x_n$ ) are multiplied by their respective weights ( $w_1, w_2, \dots, w_n$ ), and a bias term ( $b$ ) is added. The resulting values are used to compute the linear function ( $z$ ), which is then passed through an activation function ( $f$ ) to produce the output ( $y$ ).

Expanding on the idea of artificial neurons, the Multi-Layer Perceptron (MLP) [78] enhances the functionality of a single neuron by introducing multiple interconnected layers of neurons. This extended architecture allows the MLP to effectively address non-linearly separable problems, as depicted in Figure 1.8. The MLP consists of

an input layer to receive signals, an output layer responsible for decision-making or predictions, and between these layers, any number of hidden layers.

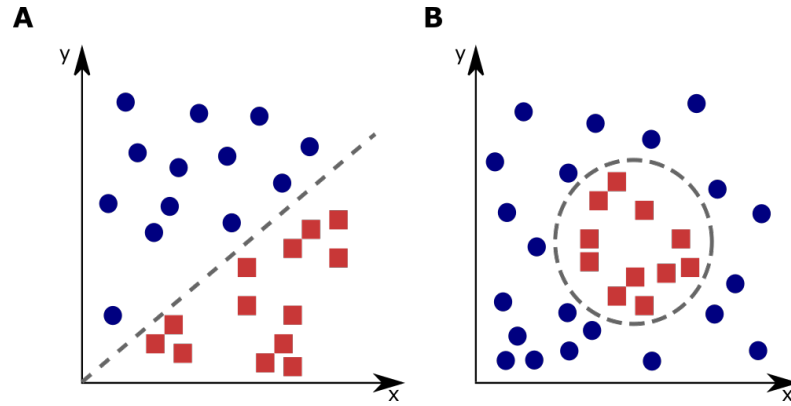


Fig. 1.8: Schematics for linear (A) and nonlinear (B) separation problems.

MLPs are widely utilized in supervised learning, where they are trained using input-output pairs to learn the underlying relationships between the variables. During training, the weight parameters of the model are adjusted in a feedforward [79] manner to minimize the discrepancy between the desired and predicted outputs. The backpropagation [79] technique is then employed to fine-tune the model by making further adjustments based on the calculated error, often measured using the root mean square error (RMSE). Thus, during the feedforward phase, the processing in an MLP focuses only on capturing the relationship between the current input and its corresponding true output. In contrast, during the backward phase, the MLP propagates the partial derivatives of the error function with respect to the weights, using the chain rule.

This propagation generates an error gradient, which guides the adjustment of the weights towards minimizing the MLP's overall error. Optimization algorithms based on gradients, such as stochastic gradient descent, are employed to perform these weight adjustments. The MLP iteratively repeats this process until the error can no longer be reduced, achieving a state known as convergence. The architecture of the MLP, as well as its training process is schematized in Figure 1.9. Moreover, an MLP can predict continuous values in a sequence or cluster data into classes.

Through the utilization of feedforward propagation, the backpropagation algorithm [80], and the gradient descent algorithm [81], the neural network is able to minimize the discrepancy between input and output, leading to the acquisition of patterns from the input data. This iterative procedure is commonly referred to as training. In supervised learning models, as previously mentioned, it is imperative to furnish the network with class labels corresponding to each input image.

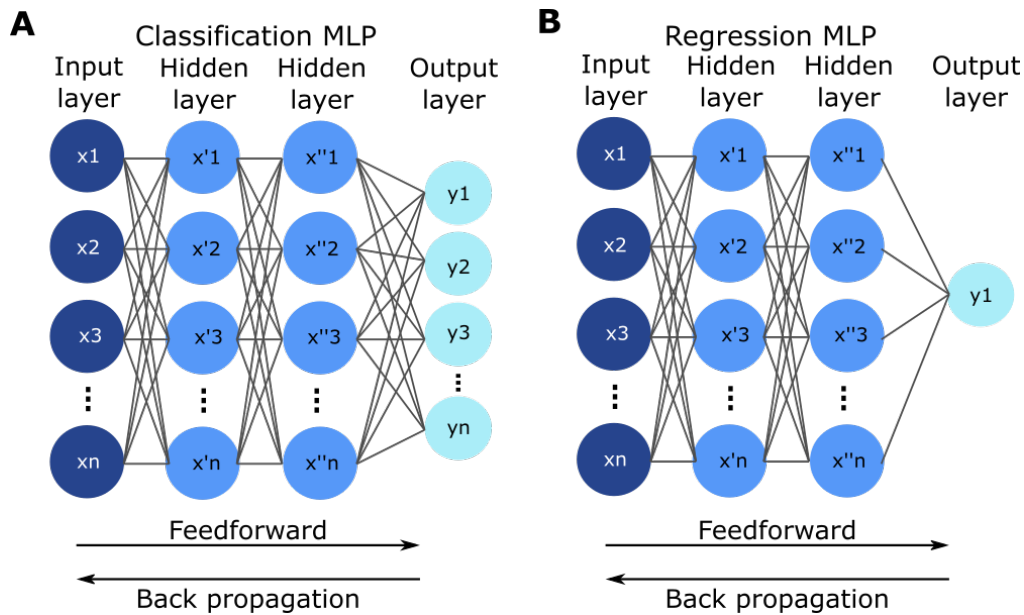


Fig. 1.9: The MLP consisting of multiple layers of interconnected neurons. It involves two main steps: Feedforward and Backpropagation. In a classification task (A), the MLP takes input data and produces an output representing the predicted class. Backpropagation updates the network's weights based on the error between the predicted and true classes, improving performance. In a regression task (B), the MLP predicts continuous values, and Backpropagation adjusts the weights using the error between predicted and actual values to improve approximation of the target.

## Variational Autoencoder

Autoencoders are a type of feedforward neural network that aims to reconstruct the input data at the output layer. Unlike traditional MLPs that focus on classification or prediction, autoencoders are designed for dimensionality reduction. They compress the input data using an encoder component, resulting in a lower-dimensional code, and then reconstruct the original data using a decoder. The compressed representation of the data is referred to as the latent space.

Autoencoders provide a valuable approach for identifying classes or subclasses within unlabeled data. By reducing the dimensionality of the data to a smaller number of output neurons, the autoencoder model becomes adept at effectively partitioning the data into distinct subgroups or clusters. This capability proves particularly useful in scenarios where the goal is to uncover meaningful patterns or clusters within a large dataset, enabling better understanding and analysis of the underlying structure. The encoder, typically a fully-connected ANN with mul-

multiple layers, takes the input data and produces a new representation of the data through feature selection or extraction. This process reduces the dimensionality of the data by compressing it into a lower-dimensional code. The decoder, which has a mirrored architecture of the encoder, reverses this process by reconstructing the original data from the code. The dimensionality reduction occurs in the middle layer between the encoder and the decoder. The number of neurons in this layer determines the dimensionality of the code, with fewer neurons resulting in more compression in the latent space. The latent space is a fixed-size vector representation that is learned through unsupervised learning, where the network learns to encode and decode the data without the need for explicit class labels.

While traditional autoencoders are effective for reducing the complexity of a dataset without prior classification, they have limitations. Depending on the data distribution, the size of the latent space, and the design of the encoder, the data compression can be lossy, meaning that some information may be lost during the encoding process and cannot be fully recovered during decoding. To address this limitation, a probabilistic approach to the latent space was introduced, leading to a modified version of autoencoders called Variational Autoencoders (VAEs) [82]. VAEs incorporate probabilistic modeling techniques to capture the underlying distribution of the data in the latent space. This allows for more flexibility in generating new samples and enables better control over the generation process. The distinction between a traditional autoencoder and a VAE can be observed in Figure 1.10.

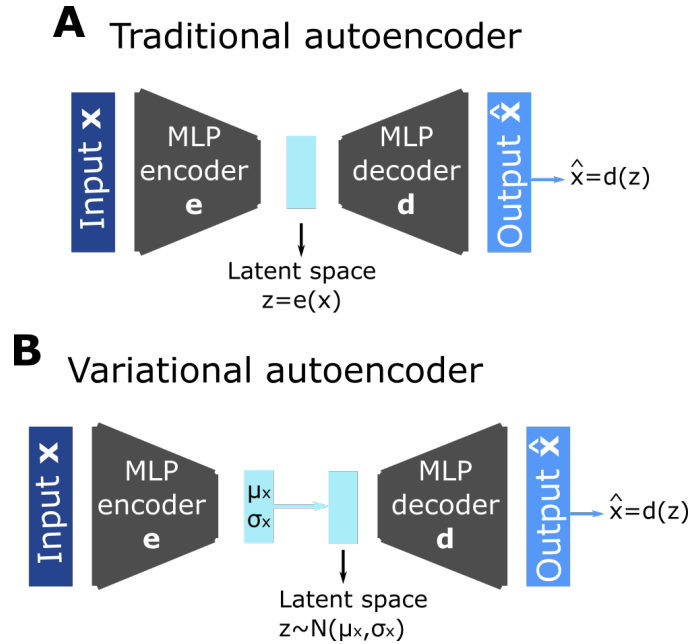


Fig. 1.10: Architecture of a conventional autoencoder (A) and a variational autoencoder (B), emphasizing the distinction in how the latent space is formed.



In a traditional autoencoder, the encoder takes the input data and maps it to a latent space representation. This mapping is typically deterministic, where each input is mapped to a unique point in the latent space. The decoder then reconstructs the input data directly from the latent representation. On the other hand, in a VAE, the encoder takes a slightly different approach. It assumes that the latent space follows a Gaussian distribution, meaning that each point in the latent space is not a single value but a probability distribution. Instead of directly mapping the input data to a point in the latent space, the encoder outputs the parameters of the Gaussian distribution, such as the mean and variance. From these parameters, a point in the latent space is then sampled probabilistically.

### Convolutional Neural Network

Convolutional Neural Networks (CNN) [83] are similar to the MLP model, but they are specialized for pattern recognition in images. MLP models are typically limited in scalability, meaning that while they can yield satisfactory results for non-graphical data or images with few color channels, their effectiveness decreases as the size and complexity of an image grows. As the demand for computational power and resources rises with larger and more intricate images, there arises a need for more robust neural network architectures capable of handling such challenges.

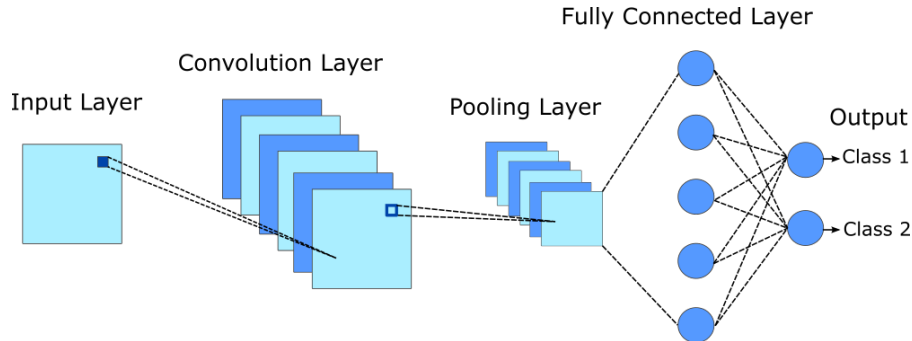


Fig. 1.11: CNN architecture schematic. The illustrated model consists of an input layer, a convolutional layer, a pooling layer, a fully connected layer with 5 neurons, and two output neurons which assign a class as the final result.

By using image-specific features in their architecture, CNNs can reduce the number of parameters needed for the model to learn. Their architecture, as shown in Figure 1.11, consists of an input layer that maintains the pixel values of the image, followed by two sub-layers, a convolutional and a pooling layer, focused on creating a new representation for the image. The convolutional layer determines the output of neurons connected to local regions of the input by computing the scalar product [84], and the pooling layer reduces the spatial dimension of the input [84]. In a row

comes a fully connected layer, such as an MLP, which produces class scores from the activations. The Neuron activation occurs through an activation function, which introduces non-linearities to the processing of its input signal, thereby enabling the network to solve complex problems. One of the most commonly used activation functions is the Rectified Linear Unit function (ReLU) [85], which only activates neurons with positive input in the MLP. Together, the activation function and the MLP extract meaningful features from the images.

According to Kim *et al.* [86], CNNs have emerged as the primary model for medical image analysis. However, CNNs typically require a substantial amount of training data, which poses challenges due to limited data availability and the cost associated with expert-preclassified data [86]. To address the issue of data scarcity, transfer learning (TL) techniques started to be employed in this field. TL is a machine learning technique introduced by Pan and Yang [87] that is based on the concept of transferring knowledge from related tasks to enhance performance on a new task. The objective of TL is to enhance learning in a target domain by leveraging knowledge from a source domain and task. By doing so, TL mitigates the need for large annotated datasets and extensive training time by utilizing existing knowledge. Overall, TL facilitates improved performance by transferring knowledge from one task to another, thereby addressing the challenges posed by limited data availability and the high costs associated with expert-labeled datasets.

TL applied to CNNs involves the transfer of knowledge at the parameter level [86]. In this approach, well-trained CNN models utilize the learned parameters of the convolutional layers for a new task in the medical domain. For instance, a CNN that has been trained on a diverse dataset containing hundreds of thousands of images to recognize objects like cars, people, and animals, can be leveraged to learn a new task such as classifying RBC images. Among the various transfer learning approaches in CNN models, fine-tuning plays a vital role in enabling a CNN to classify a different set of images than its original training set. In the fine-tuning process, the parameters of the pre-trained CNN, including the parameters of the convolutional layers, are updated during the adjustment of the model for the new task. Typically, this involves retraining the model by incorporating additional images that are relevant to the new task. By fine-tuning the model, the CNN can adapt its learned features to the specific characteristics of the new task, leading to improved performance. And in addition to dealing with data sparsity, Fine-tuning also offers the advantage of reducing the time and computational resources required to train a CNN model from scratch.

### AI for shape classification

Since the 1960s, researchers have developed various technologies to measure RBC deformability as it has the potential to be a physical biomarker. These methods include micropipette aspiration, ektacytometry, and cell transit analyzer techniques. According to [88], traditional methods for measuring RBC deformability can be classified into two types: the one that measures the average deformability of thousands of cells [89, 90], called bulk flow methods. And the other called as single-cell techniques, which provide precise measurements of individual cells with low throughput [91, 92]. Microfluidic devices fall under the category of single-cell techniques. With their diverse architectural designs, ranging from narrow, straight channels to conical constrictions and tight channels for transition and deformation [73], have significantly advanced the field of RBC deformability measurement when coupled with high-speed imaging and automated image analysis.

The crucial advancement in automated RBC image analysis, particularly in the investigation of RBC deformability, was made possible through the application of artificial intelligence-based methods. The manual classification of 2D images based on a portion of the cell surface [18] used to be the sole method for investigating RBC shapes, leading to subjective and time-consuming evaluations. The use of artificial intelligence to perform such tasks has now become a faster and automated solution, overcoming the difficulties of manual procedures. This method results in fast, unbiased, and efficient morphological assessment with accuracy values comparable to those obtained by different human experts as shown in several studies [93–95]. The study [94] introduces a method to detect and image single RBC in microfluidic flow using AI and optical modulation. A binary modulation mask is employed to simulate the image of each passing RBC and a correlation sequence (called “fingerprint”) is obtained to encode its features. An artificial neural network (ANN) then decodes the fingerprints to reconstruct the cell image. The proposed ANN architecture is a multilayer perceptron with an input layer, three hidden layers, and an output layer. The size of the input layer corresponds to the length of the correlation sequence for each cell, while the output layer corresponds to the number of pixels in each reconstructed image. The mean square error (MSE) and Adaptive Moment Estimation (Adam) [96] were chosen as loss function and optimizer —element that adjusts the learning rates of each parameter, adapting them as the training progresses— to train the ANN. The research revealed that accurate reconstruction of RBC images requires binary masks with 2D modulation schemes. Furthermore, the findings indicate that this technique could be an effective and direct approach for various RBC disease characterization applications.

Kihm *et al.* [93] investigated the use of a regression-based Convolutional Neural Network (CNN) to differentiate between the two stable and transient RBC

shapes in microfluidic channels. The CNN was trained through supervised way with single-cell RBC images, resulting in a classification system and statistically derived thresholds. The classification and thresholds were utilized to construct a phase diagram, which was automatically generated and then compared to manual evaluations of RBC shape transitions. It was demonstrated that this method removes the necessity for subjective user input and enables an accurate and efficient evaluation of RBC geometries in microchannels and opening future perspectives to predict phase diagrams under the influence of certain drugs or blood diseases. Moreover, to evaluate if RBCs can be automatically classified by their deformability in microfluidic channels, Lamoureux *et al.* [95] used a microfluidic ratchet device to sort RBCs and capture images of deformed cells using brightfield microscopy. A CNN was trained and validated using these images to classify RBCs based on their shape. Initially, the CNN was trained in a supervised manner using single-cell image and its true deformability labels determined by microfluidic sorting, which resulted in misclassification due to imbalanced data. To improve accuracy, different deformability labels were grouped into two classes, resulting in binary classification into deformable and rigid cells with an accuracy of  $81\% \pm 11\%$  on average across ten donors. The authors also highlighted the potential benefits of combining microfluidics with AI, such as the ability to diagnose and monitor diseases related to abnormal RBC deformability, in addition to demonstrating the potential of deep learning for fast and precise assessment of RBC deformability.

In addition, Rizzuto *et al.* [57] employed a microfluidic device to simulate spleen slits and investigate rare hereditary hemolytic anemia (RHHA) by analyzing RBC shape through machine learning. The CNN neural network AlexNET [73] was used for transfer learning to convert each RBC image from the microfluidic filter to a feature vector for a second stage of pattern recognition analysis. An automatic classifier, the Support Vector Machine (SVM), was then trained in a supervised way to discriminate between "healthy" and "unhealthy" cells, as well as between healthy and three RHHA subtypes (sickle cell disease, thalassemia, and Hereditary spherocytosis). The AI-based classification method successfully distinguished RHHA patients from healthy donors with 91% accuracy and between specific diseases with 82% accuracy. Thus, the authors suggest that this method is useful for patient screening or monitoring disease progression. Further, [97] proposed an unsupervised network to classify RBC storage lesions, which learns the morphological properties of RBCs without relying on the visual categories defined by experts. The ResNet50 [98] neural network architecture is used to predict the storage duration of the blood unit from which each cell was taken. An intermediate layer of the network is then employed to compute features that capture morphological changes in response to storage, and the Uniform Manifold Approximation and Projection (UMAP) dimensionality reduction method is used to map cells onto a linear map that captures the lesions. The resulting 1D UMAP ranges from healthy to un-

---

healthy RBCs and was used as the basis for a new blood unit quality metric, called self-learned morphology index (SMI), which can assess the quality of blood units over time. The authors concluded that their proposed artificial intelligence method provides a simple, label-free sample preparation, which enables non-experts to assess the quality of stored blood, based on the 76.7% agreement with human expert classification for seven clinically relevant RBC morphologies associated with storage lesions.



## 2 Materials and Methods

Within this chapter, the materials and methods employed in this study are comprehensively outlined. It covers the detailed description of the experimental materials used and the methodology adopted for conducting the research, serving as a guide for the subsequent analyses.

### 2.1 Sample preparation

For the *in vitro* experiments various blood samples from heparin tubes utilized, and for transfusion samples, from blood units, as specified in Table 2.1. The research followed the guidelines of the Declaration of Helsinki and was approved by the local ethics committee (Ärztchamber des Saarlandes) for all blood sample analyses (permit number 51/18 and reference #20-643, #20-982). The protocol to prepare the blood solutions is outlined in the following steps i-v and it is illustrated in Figure 2.1:

- (i) Blood samples were centrifuged at  $1500\times g$  for 5 min to separate RBCs and plasma.
- (ii) Plasma was removed and stored in a second Eppendorf tube for future use if needed.
- (iii) Sedimented RBCs were resuspended in 1 mL of phosphate-buffered saline (PBS) or Tyrode solution, depending on the type of experiment. The solutions used are resumed in Table 2.2.
- (iv) The centrifugation and washing steps were repeated three times.
- (v) The washed RBCs were resuspended in a final solution with a hematocrit of 0.5%.

It should be noted that the final suspension needs to be compatible with the solution used for cell washing. Therefore, when the cells were washed with PBS, the final cell suspension solution consisted of PBS with 0.1% bovine serum albumin (BSA) or pure plasma. However, when the cells were washed with Tyrode, the final

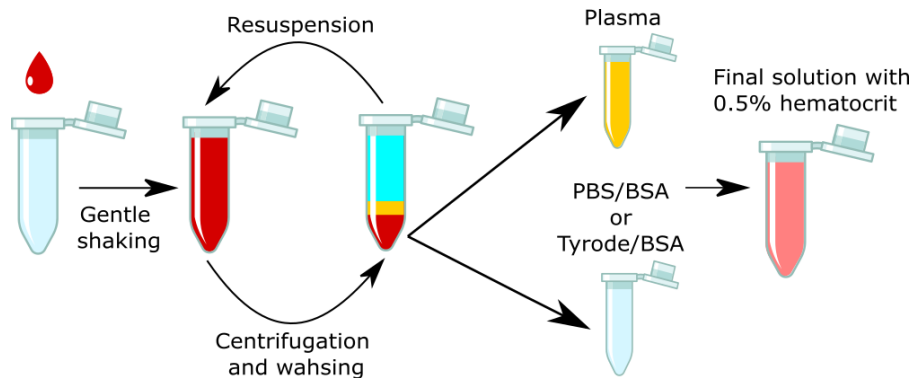


Fig. 2.1: The blood washing process (from left to the right) involves taking 100  $\mu\text{l}$  of a blood sample and adding it to a buffer, followed by gentle agitation and centrifugation and dilution in a buffer for three times. After the last centrifugation, the 6  $\mu\text{l}$  of sedimented RBC is diluted with 1 ml of buffer and 1 mg of BSA to obtain the final solution.

Tab. 2.1: Information regarding the blood samples

Samples type	Sample source	Storage Type	Sample amount
COVID-19	Intensive Care Unit at the Frankfurt University Hospital	Heparin tube	13
Stored blood	Institute for Clinical Hemostasiology and Transfusion Medicine, Saarland University, Homburg/Saar	Erythrocyte concentrates	6
Neuroacanthocytosis syndromes	Neurodegeneration Section "Albrecht-Kossel", Department of Neurology, University Medical Center Rostock, University of Rostock, Rostock, Germany	EDTA tubes	9
Huntington's Disease	Huntington Center South, Taufkirchen/Germany	EDTA tubes	7
Sickle Cell Disease	Hospices Civils de Lyon, Lyon/France	Heparin tube	4



Tab. 2.2: Solution and Reagent Concentrations

<b>Solution</b>	<b>Reagent</b>	<b>Concentration</b>	<b>Provider</b>
PBS	PBS	1 X	Gibco Life Technologies
	NaCl	130 mM	
	KCl	5 mM	
Tyrode	Glucose	5 mM	-
	HEPES	10 mM	
	MgCl <sub>2</sub>	1 mM	
	CaCl <sub>2</sub>	1.3 mM	

solution consisted of Tyrode with 0.1% BSA. Also, in certain experiments, the effect of plasma on RBC shapes was studied by performing plasma exchange between patients and controls. Additionally, it is important to mention that in cases where plasma was used to resuspend the RBCs, it underwent a similar washing procedure as depicted in Figure 2.1. Following separation from the RBCs, it underwent centrifugation for 5 minutes to ensure the elimination of platelets.

This involved suspending RBCs from patients in the control plasma of matching blood groups (ABO and Rh), and control RBCs in patient plasma, resulting in four sample groups: control RBCs in control plasma, patient RBCs in patient plasma, control RBCs in patient plasma, and patient RBCs in control plasma, as demonstrated in [10].

## 2.2 Deoxygenation stage

To accurately study the characteristic shapes of RBC in SCD samples, it is essential to replicate the hypoxic conditions that occur in our body following tissue oxygenation. In order to achieve this, a specific procedure is followed. After the samples are prepared, they are placed inside a glove box for an incubation period of 8 hours. This glove box is a sealed container equipped with gloves that allow manipulation of the samples while maintaining a controlled environment.

Inside the glove box, the sealed environment is adjusted to contain 3% oxygen ( $O_2$ ) and 97% nitrogen ( $N_2$ ) gas mixture. This is achieved by introducing nitrogen gas into the glove box until the desired composition is reached. The experimental setup has been adapted to operate within the glove box to ensure that the conditions are maintained throughout the duration of the experiment.

To create the necessary internal gas conditions, a liquid nitrogen tank is employed.

The cover of the tank incorporates an electric resistance that, when heated, accelerates the evaporation of liquid nitrogen. The resulting vapor is then directed into the glove box through a hose. Simultaneously, another hose is used to expel the oxygen from the glove box, as illustrated in Figure 2.2. This setup allows for the establishment and maintenance of the desired hypoxic conditions required for the experiment.

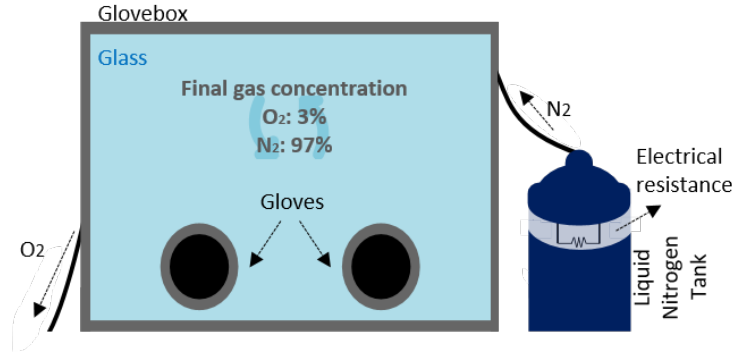


Fig. 2.2: Diagram illustrates the functioning of the glove box. The process involves heating a resistance to convert the liquid nitrogen stored in the tank into steam. The generated nitrogen gas ( $N_2$ ) is then directed into the glove box, where the oxygen ( $O_2$ ) is expelled, resulting in the creation of hypoxic conditions.

Throughout the execution of the experiment, the glove box ensures that the samples remain in an environment with a controlled oxygen level, mimicking the conditions that occur in the body during deoxygenation. By replicating these conditions, it is possible to observe and study the different shapes acquired by sickled RBCs.

## 2.3 Microfluidic chips preparation

In this study, straight and parallel microcapillaries embedded in an elastomer substrate (“microfluidic chips”, see Figure 2.3A) were utilized. The microfluidic channel chips were manufactured using soft lithography [99], a technique that prints a inversed (“negative”) micro-structures onto a silicon mold using a photoresist of controllable structure height.

The silicon mold allows for identical copies of the architecture to be replicated using elastomers [100]. The molds were filled with polydimethylsiloxane (PDMS) in a component ratio of 10:1 and then placed in an oven at  $70^{\circ}\text{C}$  to harden. Once hardened, the PDMS was removed from the mold, resulting in the positive shapes of the microfluidic structures. Holes were then punched in the inlet and outlet

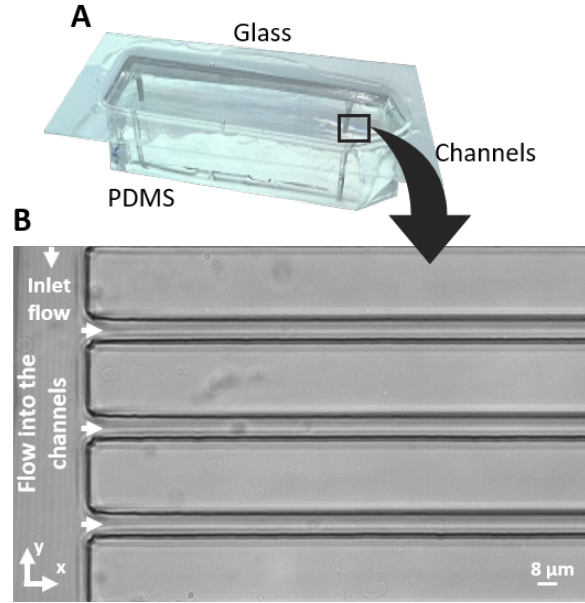


Fig. 2.3: (A) An actual image of the microfluidic channel mold filled with PDMS (the microfluidic channel structure is located at the bottom of the mold). (B) Microscopic images of the channel captured with a 10X objective.

reservoirs of the microchannels to allow for connecting tubes to the channels. Finally, the PDMS chip and a glass slide were activated in a plasma-cleaner to be bonded [101], completing the chip production process.

The microfluidic chip design chosen consists of 10 straight and parallel channels, each with a rectangular cross-section measuring  $8 \mu\text{m}$  in height and  $11 \mu\text{m}$  in width, and a total length of 40 mm. At both ends of the chip, the 10 channels are connected, and share common fluid inlet and outlet reservoirs. Figure 2.3B illustrates the architecture of the microfluidic chip utilized.

## 2.4 Microfluidics experiment

The experimental setup comprises a series of intricate steps. As detailed in [4, 6] and illustrated in Figure 2.4, a microfluidic chip is first connected via medical-grade polyethylene tubing to an Eppendorf tube containing the RBC suspension and to a waste Eppendorf tube. This chip is then affixed to a Märzhäuser Wetzlar Scanning Stage SCAN IM 120 x 100, a computer-controlled motorized stage, which, in turn, links to a Nikon Eclipse TE2000-S inverted microscope.

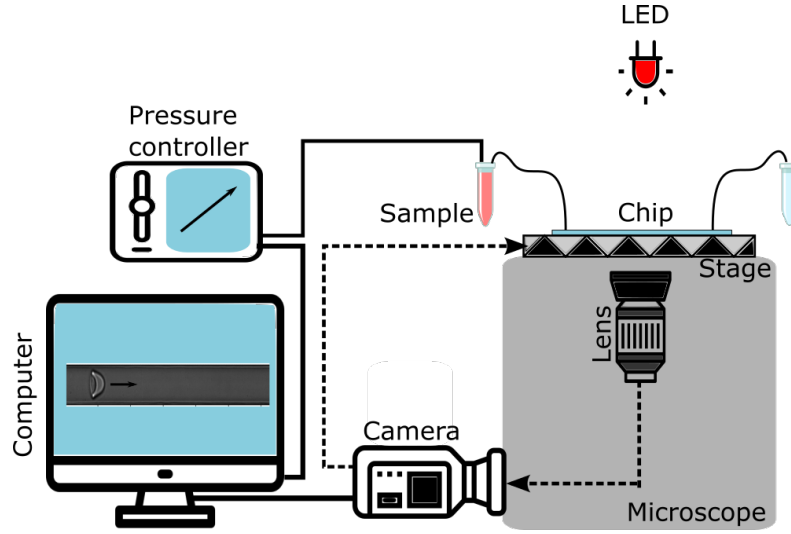


Fig. 2.4: The schematic shows experimental setup to study RBCs in microcapillary flow.

Equipped with a 60X oil immersion objective lens (Nikon Plan Apo VC 60X), an LED illumination system, and a USB 3.0 camera (The Imaging Source DTK 23U1300), the microscope records single RBC flow through the channels, maintaining a fixed at half the width of the channel. The flow of single cells is regulated by a high-precision pressure device (Elvesys Elve Flow OB1-MkII), ensuring a consistent pressure drop within a range of 100 to 1000 mbar. Recorded images in AVI format depict a field of view of  $1280 \times 140 \text{ pixels}^2$ , covering an area of  $435 \times 34 \text{ } \mu\text{m}^2$ . These captured images, recorded at a frame rate determined by the applied pressure drop (100 Hz, 200 Hz, or 400 Hz), are the basis for subsequent video processing.

## 2.5 Tracking and cropping toolbox

A self-written Python [102] script is used to process the video obtained in the previous step. The purpose of the script is to track the position of each individual cell as it moves within the channel, and to calculate some descriptor, such as its velocity of movement, area, the position of its center of mass, and the vertical offset of the y-axis of the cell center of mass relative to the channel middle. The tracking of individual cells is accomplished by examining all frames in the analyzed video. To generate a binary image from each frame, a binary filter is applied that selects pixels with an intensity equal to or greater than a specified threshold. This image

binarization is necessary for cell detection and differentiation from the background. Figure 2.5 illustrates the application of the filter in an empty frame and a frame that contains an RBC.

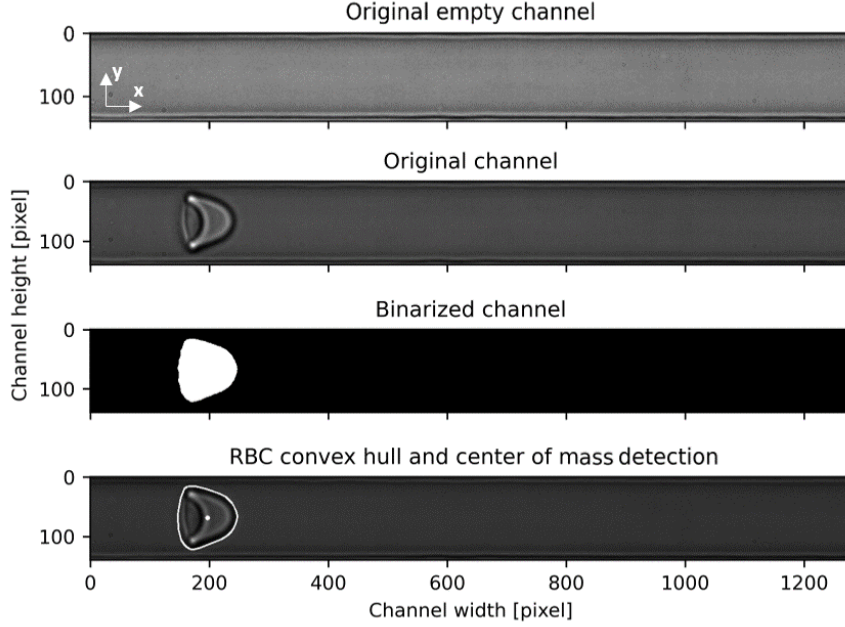


Fig. 2.5: Process of tracking a RBC as it crosses the microfluidic channel. The upper frame shows a channel without RBCs, whereas the second frame displays the moment when a RBC enters the channel. The third frame shows the binary representation of the channel with the RBC, and the final frame indicates the detection of the RBC by its center of mass and contour.

The gray scale intensity threshold, which is set at 25, represents the pixel intensity used in image processing. All pixels with an intensity greater than or equal to 25 are selected as part of the cell (second plot of Figure 2.5) and not the background. The binarization is applied to identify the cell edges through the convex hull contour technique [103], which describes the smallest convex polygon  $P(x_j, y_j)$  containing all the  $J$  points of the set  $j = 0, 1, 2, \dots, J - 1$ , and  $(x_0, y_0) = (x_J, y_J)$ . The cell area is calculated as states in Equation 2.1:

$$A(P(x_i, y_i)) = \frac{1}{2} \sum_{j=0}^{J-1} (x_j y_{j+1} - x_{j+1} y_j) = \sum_{i=1}^J x_j (y_{j+1} - y_{j-1}) \quad (2.1)$$

The OpenCV package [104] provided in Python are used to calculate both the cell

area and the cell center from the convex hull polygon. The vertical offset between the center of mass of the cell and the middle of the channel is then calculated using the variables related as described in Equation 2.2:

$$Y_{\text{offset}} = \text{channel middle}_y - \text{center of mass}_y + \text{upper channel wall}_y \quad (2.2)$$

The algorithm "crops" each scanned RBC image into a 160x140 pixel sub-image centered on the cell's center of mass and assigns descriptors to it. Figure 2.6 illustrates the single cell identification procedure descriptors obtained by the analysis and the final image for both low Figure 2.6A and high RBC velocity Figure 2.6B. This technique can detect and describe the cases where only one cell crosses the channel, multiple cells cross the channel without interacting, and a group of interacting cells follows the same path, as shown in Figure 2.6C. If the last case is identified, the program discards the results since analyzing the interaction between RBCs crossing a microfluidic channel is beyond the scope of this study.

After being cropped, each new single cell image is marked with the frame number in which it appears, in addition to its descriptive parameters. The marked RBC images are then analyzed using the Structural Similarity Index (SSI) [105], which takes into account luminance, contrast, and structure of the image, to compare the images in subsequent frames. The SSI values range from 0 to 1, with a value of 1 indicating a perfect match between the analyzed images. A selected SSI threshold of 0.7 was applied. Therefore, when performing image comparisons, if the SSI was greater than or equal to 0.7, the compared images were designated as belonging to the same RBC. The SSI method is already implemented in the scikit-image package [106] in Python. After identifying all the images of a single cell, the velocity of the RBC can be calculated using the x-coordinate of their center of masses through a linear regression. The following estimate is used for the Equation 2.3:

$$\hat{y} = \hat{m}x \quad (2.3)$$

Where the estimated variable *haty* corresponds to the sample points, the predictor variable *x*, to the positions of the cell center, and *hatm* is the slope of the relationship between the estimated variable *haty* and the predictor variable *x*. Thus, the velocity in mm s<sup>-1</sup> of each individual RBC is given by the Equation 2.4:

$$V = \frac{\text{pixel size} \times \hat{m}}{\text{magnification}} \times \frac{1}{\text{FPS}} \quad (2.4)$$

The pixel size, magnification, and frame-per-second rate (FPS) parameters are

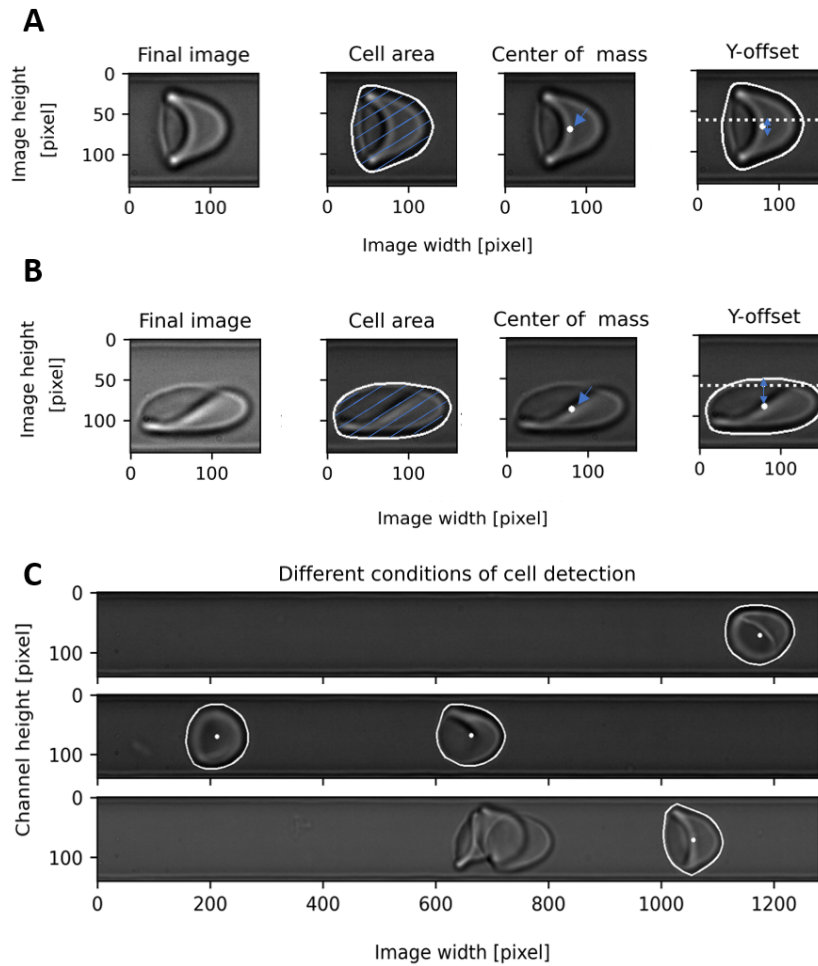


Fig. 2.6: RBC flow parameters. The final image generated by the tracking and cropping algorithm for a RBC at low velocity is shown in frame A, followed by its area (within the white outline), center of mass, and Y-offset relative to the channel walls. Frame B presents the same measurements for a RBC at high velocity. Frame C presents some conditions that are considered for cell identification and analysis when crossing the microfluidic channel, with an emphasis on the exclusion of groups of interacting cells (cell clusters).

Tab. 2.3: Fixed values in the experiment

<b>Fixed values</b>	<b>Values</b>
Pixel size	$4.8 \times 10^{-6} \mu\text{m}$
Magnification	$60\times$
FPS	100 mbar, 200 mbar, or 400 mbar

fixed values describes in Table 2.3. Once these descriptors are calculated, a detailed information on the behavior of the cell as it crosses the entire microfluidic channel is obtained.



## 3 Results

This chapter provides an outline of the results obtained from the implementation process of the toolbox proposed in this study and the subsequent analyses derived from it.

### 3.1 Methodology development

#### 3.1.1 RBC shape miniaturization

In order to categorize the classes of RBC shapes within the dataset derived from the tracking and cropping algorithm, an initial strategy was employed involving the miniaturization of RBC shapes [94]. This approach was proposed as a viable alternative to utilizing flow cytometers and drew inspiration from the functioning principles of autoencoders. Considering that the RBC images morphology changes as the velocity increase, this approach exhibits potential in automatically differentiating the RBC shapes in the flow, all while maintaining low computational resources.

The proposed method suggests utilizing optical and spatial modulation of RBC images through a mask. This method replicates the effect of a mask positioned between the channel and the light sensor to capture visual data as cells pass through this area. The mask comprises both opaque and transparent regions, which modulate transmitted light, generating signals dependent on the mask's pattern, the cell's inherent characteristics, and its velocity. Consequently, the mask is capable of encoding the fundamental morphological attributes of the cells into a singular signal, acting as a unique fingerprint  $S(x)$  for each cell. Figure 3.1 shows the technique to be simulated.

The simulated mask is binary pattern consisting of black and white sections, where black areas are represented by pixels with a value of 0, and white areas are represented by pixels with a value of 1. In this pattern, black areas indicate optically blocked regions, while white areas denote non-blocked regions. To generate the  $S(x)$  signal, the process involves pixelwise multiplying each RBC image by the binary

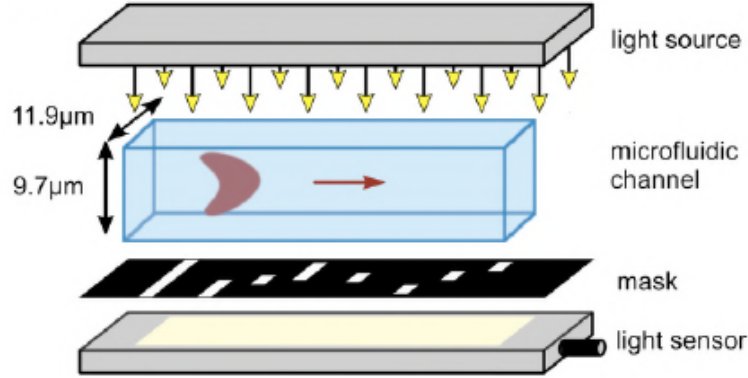


Fig. 3.1: Simulated set up. A single cell crosses a microfluidic channel, encounter light source, and the transmitted light is subject to modulation by a binary amplitude mask situated between the channel and a light sensor. The modulated signal acts as a unique fingerprint  $S(x)$  for the single cell. Taken from [94].

modulation mask, integrating the resulting intensities, simulating cell motion via displacement, and calculating the correlation signal using the masked sub-images. Additional steps such as truncation are applied to enhance the quality of the correlation signal, ultimately yielding a final correlation sequence or fingerprint.

The characteristics of the generated fingerprint signal are intricately linked to the design of the mask, leading to the experimentation with various mask designs. Among them, the barrel organ design demonstrated the most favorable outcome in signal generation. The mask design, along with the fingerprint signals for a slipper and a croissant are illustrated in Figure 3.2.

In the process, the mask acts as an encoder, producing an encoded signal for each image, while an Artificial Neural Network (ANN) serves as the decoder to reconstruct the cell image based on its fingerprint. The encoder was provided with a set of 1853 images of a healthy control, resulting in the generation of an equal number of signals that were subsequently employed as training data for the decoder. The Figure 3.3 illustrates the outcomes of the image reconstruction for slippers, croissants and trilobes shapes.

The quality of image reconstruction was found to be greatly influenced by the specific mask pattern utilized. It became evident that the barrel organ mask could generate a fingerprint containing the essential shape information of the cells, leading to a reasonable reconstruction, as demonstrated in pairs I and IV of the Figure 3.3.

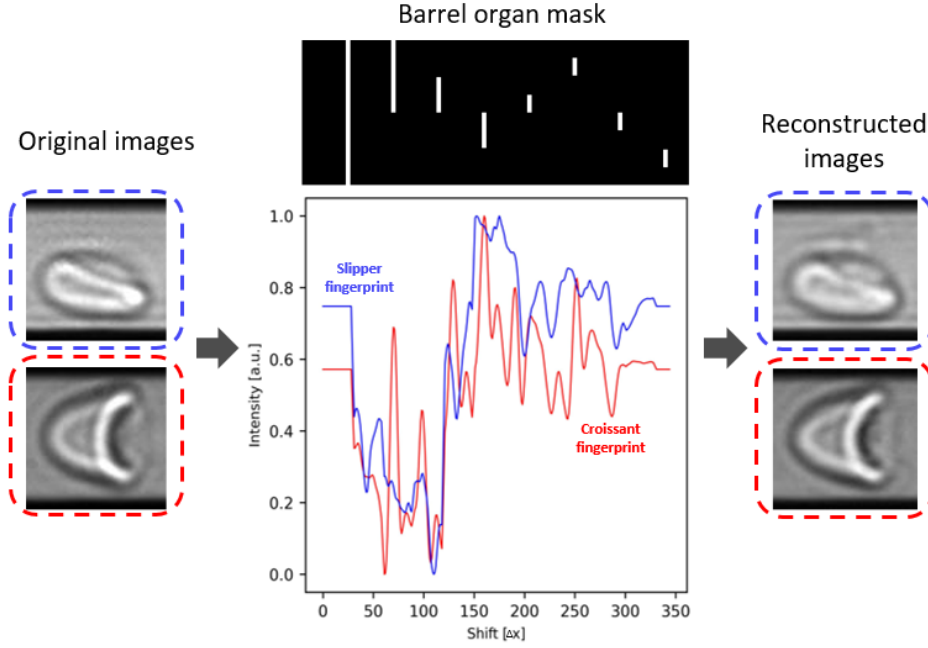


Fig. 3.2: Process of associating digital signals with images of healthy cells, specifically a slipper (highlighted in blue) and a croissant (highlighted in red), using a binary mask. This is followed by the reconstruction of the original images from the digital signals. Adapted from [94].

However, it was also observed that the reconstruction fell short for other images, as seen in pairs II, III, V, VI, and VII. This issue was attributed to the miniaturization phase of the images within the encoder, indicating that a more complex mask design would be necessary to enhance the encoding process. In order to validate this observation, the original and reconstructed images were subjected to benchmarking using the toolbox developed by Kihm *et al.* [93]. This toolbox enabled the classification of the original and post-reconstruction shapes of slippers and croissants. The results revealed that only 52% of the RBCs retained their original classification for croissants, while the corresponding figure for slippers was 54%.

Although the current method reduced the reliance on sophisticated optics (as it doesn't involve capturing the cell flow but focuses solely on the fingerprint signal using a photodiode and a light sensor), there was room for improvement. To address this, a decision was made to transition from the mask approach to a real encoder, thereby transforming the system into an autoencoder. This alteration aimed to enhance the performance of the method and overcome the limitations observed in the previous implementation.

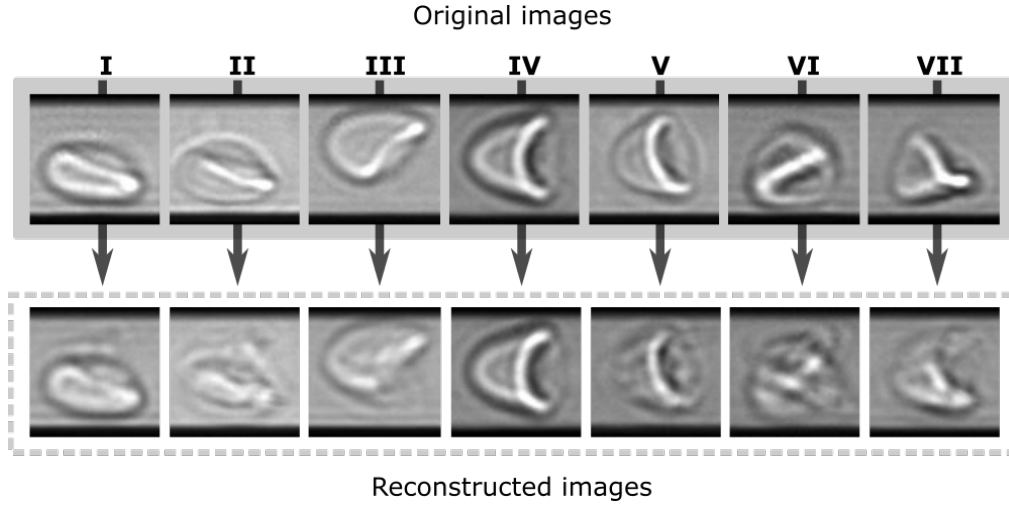


Fig. 3.3: The top images show the original images of RBC flowing through a microchannel, while the bottom ones display the reconstructed images. The reconstruction process, using a barrel organ mask, introduces ambiguities in the resulting images, particularly for cells positioned asymmetrically with respect to the horizontal off-axis. Adapted from [94].

In addition, it is essential to clarify that the initial approach and baseline methodology were designed by Martin-Wortham *et al.* [94], providing a solid foundation for subsequent enhancements. My specific contribution to the work are outlined in the Declaration of Author Contributions section, under DECLARATION 4.

### 3.1.2 Variational Auto-Encoder (VAE)

To further enhance the image reconstruction process and overcome the limitations encountered with the mask approach, a new methodology was adopted, replacing the setup mask-decoder with a VAE. The VAE offered a promising alternative by leveraging the power of deep learning. This approach aimed to address the challenges faced during the miniaturization stage of the images in the encoder and improve the encoding process. By employing a VAE, the system could learn the underlying distribution of the cell images, allowing for more accurate and efficient reconstruction. The incorporation of a VAE in place of the mask approach offered the potential for enhanced performance and the ability to capture intricate details in the reconstructed images.

At this stage, the RBC images still had no prior classification. Hence, a random subset of 100 RBC images from a healthy control was selected randomly to train the VAE model. The RBC images, which are gray scaled and have dimensions of

Tab. 3.1: Details of Encoder-Decoder Layer Setup

Layer	Kernel size	Stride	Padding	Activation function	Sub-image size (px <sup>2</sup> )
<i>Encoder</i>					
Convolution layer 1	3	2	SAME	ReLU	130 x 130
Convolution layer 2	3	2	SAME	ReLU	65 x 65
Fully connected layer				Z	
<i>Decoder</i>					
Fully connected layer				Z	
Trans convolution 1	3	2	SAME	ReLU	65 x 65
Trans convolution 2	3	2	SAME	ReLU	130 x 130

130x130 *pixels*<sup>2</sup>, underwent compression to represent each of them as a point in a 2D space, specifically denoted by the coordinates (x, y). Additionally, modifications were made to the VAE model to position each cluster of stable RBC shapes in a specific quadrant of the 2D vector space. The architecture of the neural network used as the encoder and decoder is described in Table 3.1.

The VAE model takes two-dimensional images as input and utilizes a CNN architecture with two convolutional layers and one fully connected layer as an encoder to process the input. The encoder then produces the mean and variance parameters, which form a Gaussian probability distribution for the latent space Z. In the decoder component, the latent space Z is fed as input. It employs a mirror CNN architecture of the encoder to reconstruct the mean and variance from a Gaussian probability distribution, resulting in the output representing the reconstructed image. The latent dimension size, denoted as |Z|, is set to 2. Figure 3.4 illustrates the latent space Z(x,y) obtained for 400 RBC images.

The training set for the VAE consisted of an equal number of slippers and croissant images, ensuring a balanced and diverse dataset. However, upon visual inspection of the latent space, it became apparent that this balance was not accurately reflected. Additionally, the stable RBC shapes were successfully positioned in the first, second and fourth quarters quadrants of the latent space. However, the transition shapes between slippers and croissants did not align with the shapes observed in the *in vitro* experiment as well and they are not described in the literature. As a result, the VAE approach was deemed ineffective, prompting the exploration of alternative solutions.

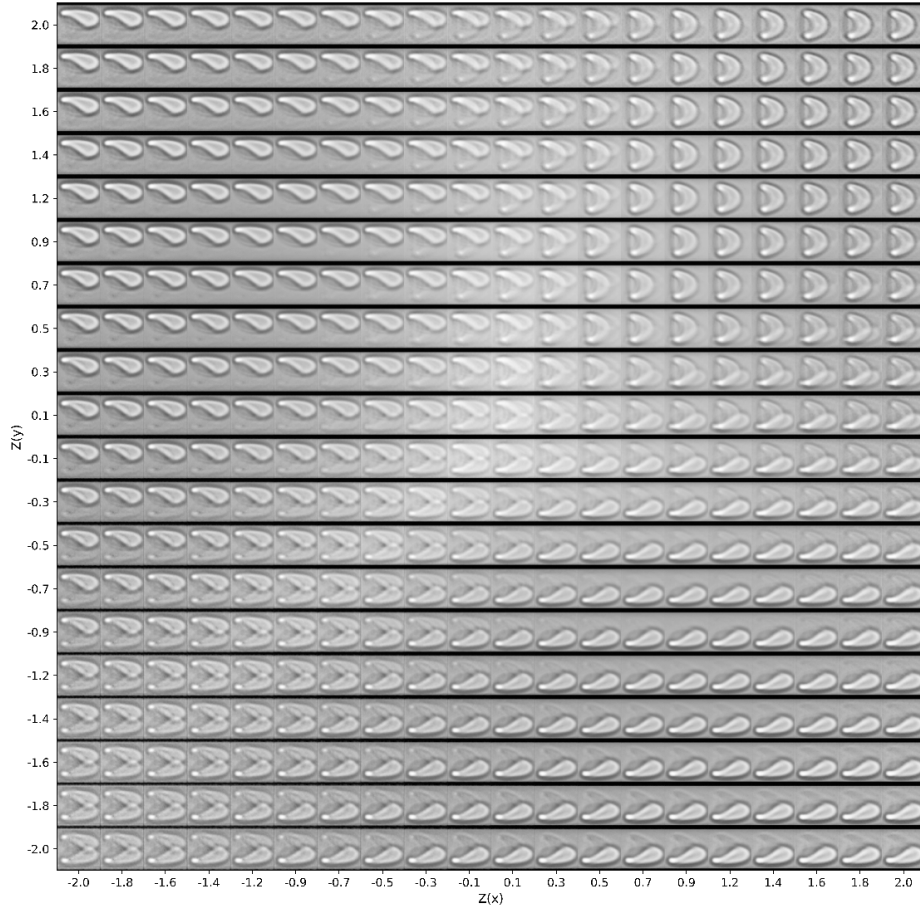


Fig. 3.4: The latent space, denoted as  $Z(x,y)$ , consists of 400 RBC images. The vertices of  $Z(x,y)$  represent the healthy and stable shapes, while the images connecting these vertices demonstrate a range of transformations between the shapes.

### 3.1.3 CNN-based decision tree

In order to address the identification of pathological RBC forms, it became evident that a simple scaling or clustering of stable forms such as croissants and slippers was no longer sufficient. Traditional machine learning architectures often require retraining the entire model when introducing new classes or data. To overcome this limitation, a 4-stage CNN-Tree model was implemented. The tree-CNN approach addresses the problem of incremental learning in image recognition, as it utilizes a hierarchical structure that expands as new classes are added, enabling the network to utilize existing knowledge while accommodating new information. By incorporating new classes as leaves, the model can effectively differentiate between similar

features of both old and new classes. This approach enables ongoing improvement and adaptation as new data becomes available. The architecture of the proposed CNN-tree is shown in Figure 3.5.

All CNNs employed in the decision tree adhered to this model, differing only in the final layer, which determined the number of classes predicted by the model. The input layer received images with dimensions of  $160 \times 140$  *pixels*<sup>2</sup>. Subsequently, three convolutional layers were incorporated, each followed by a max pooling layer, responsible for extracting essential image features. The ReLU activation function was applied to introduce non-linearities within these layers. Following the convolutional and max pooling layers, the data was flattened and passed through a dense layer comprising 64 neurons. The ReLU activation function was also employed in this layer. Finally, the output layer employed the Softmax activation function [107] to generate classification probabilities for the desired classes. The model was trained using the Adam optimizer with a learning rate of 0.00001, and the categorical cross-entropy loss function was employed for measuring the model's performance. Such architecture is described in Table 3.2.

Tab. 3.2: Architectural Details of Implemented CNN

Layer	Kernel size	Kernel initializer	Padding	Activation function	Sub-image size (px <sup>2</sup> )
Convolution layer 1	3	Uniform variance scaling	SAME	ReLU	158 x 138
Convolution layer 2	3	Uniform variance scaling	SAME	ReLU	77 x 67
Convolution layer 3	3	Uniform variance scaling	SAME	ReLU	36 x 31
Fully connected layer			Number of classes		

The tree-CNN first-stage is the seed, consisting of a CNN responsible for distinguishing between stable RBC shapes and shapes that are not considered stable, disregarding pathological deformations in the membranes. Thus, the initial classification splits RBC dataset into three categories: croissant-shaped, slipper-shaped, and shapes-not-stable.

The first branch of the tree-CNN represents the second stage of classification. For

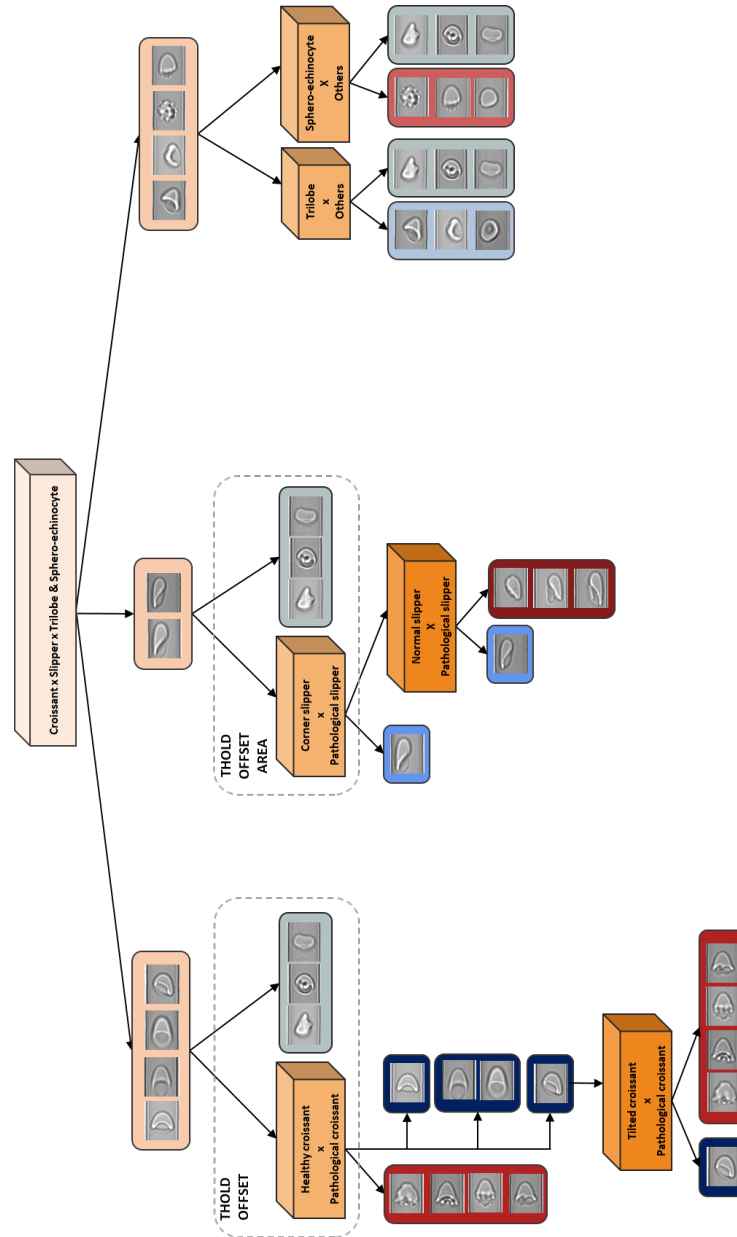


Fig. 3.5: The architecture of a tree-shaped CNN design. The initial stage consists of a CNN that can differentiate between croissant, slippers, and non-stable RBC shapes. In the subsequent step, offset and area criteria are applied to separate RBCs belonging to the "Others" class. Finally, the second stage of the CNN is responsible for distinguishing between healthy and pathological RBC shapes, as in the following stage.



RBCs initially classified as croissant-shape, the distribution of the y coordinate of the center of mass shift (y-offset) is calculated, and threshold values, defined as two standard deviations around the mean, are applied. Any cells with an offset value outside these thresholds are directly classified as "other", which means that they are not described in the literature. The remaining images within the thresholds undergo a second round of classification using another CNN, which further differentiates between healthy croissants and pathological croissants with membrane deformity. While symmetrical healthy croissant-shaped RBC show clear differentiation from pathological ones, imperfectly symmetric croissants present confusion in classification. To solve this, an additional leaf is added to the tree, incorporating a CNN capable of distinguishing between pathological croissants and healthy not perfectly symmetrical croissants. This completes the croissant branch of classification.

The slipper branch begins after the seed CNN with cells classified as the stable form of slippers, regardless of membrane deformations. A threshold is applied based on y-offset and area distributions to separate stable RBC from shapes not described in the literature. RBC within two standard deviations around the y-offset mean and area mean distributions are retained as slippers, while others are classified as "other." The remaining cells classified as slippers proceed to the next stage of classification, where a CNN differentiates between slippers with healthy membranes and those with membrane deformations. Larger slippers can be easily distinguished from the damaged ones, but smaller slippers pose challenges. Therefore, an ultimate classification leaf is added to the slipper branch, facilitating the distinction between healthy slippers with smaller areas and pathological slippers. Within the branch of cells categorized as "shapes-not-stable," three prevalent shapes emerge from the initial seed classification: trilobes, spherocytocytes, and "other" shapes. To finalize this branch, a classification leaf is incorporated, containing two CNNs. One CNN distinguishes trilobes from "other" shapes, while the other CNN separates spherocytocytes from the "other" category.

After the entire classification process within the tree, a comprehensive model is achieved, capable of classifying healthy and pathological croissants, healthy and pathological slippers, trilobes, spherocytocytes, and "other" shapes. This hierarchical approach ensures the accurate differentiation of various RBC forms, addressing the limitations of previous methods and providing a more comprehensive solution for RBC shape classification. Figure 3.6 and Figure 3.7 show a few examples of the outcomes of the branches in the CNN-tree. For the testing phase, a total of 6,143 images comprising healthy (stable and non-stable) and pathological RBC shapes were utilized.

The croissant branch was responsible for classifying 998 images from the seed. In the second stage, where thresholding was applied to separate the "others" category,

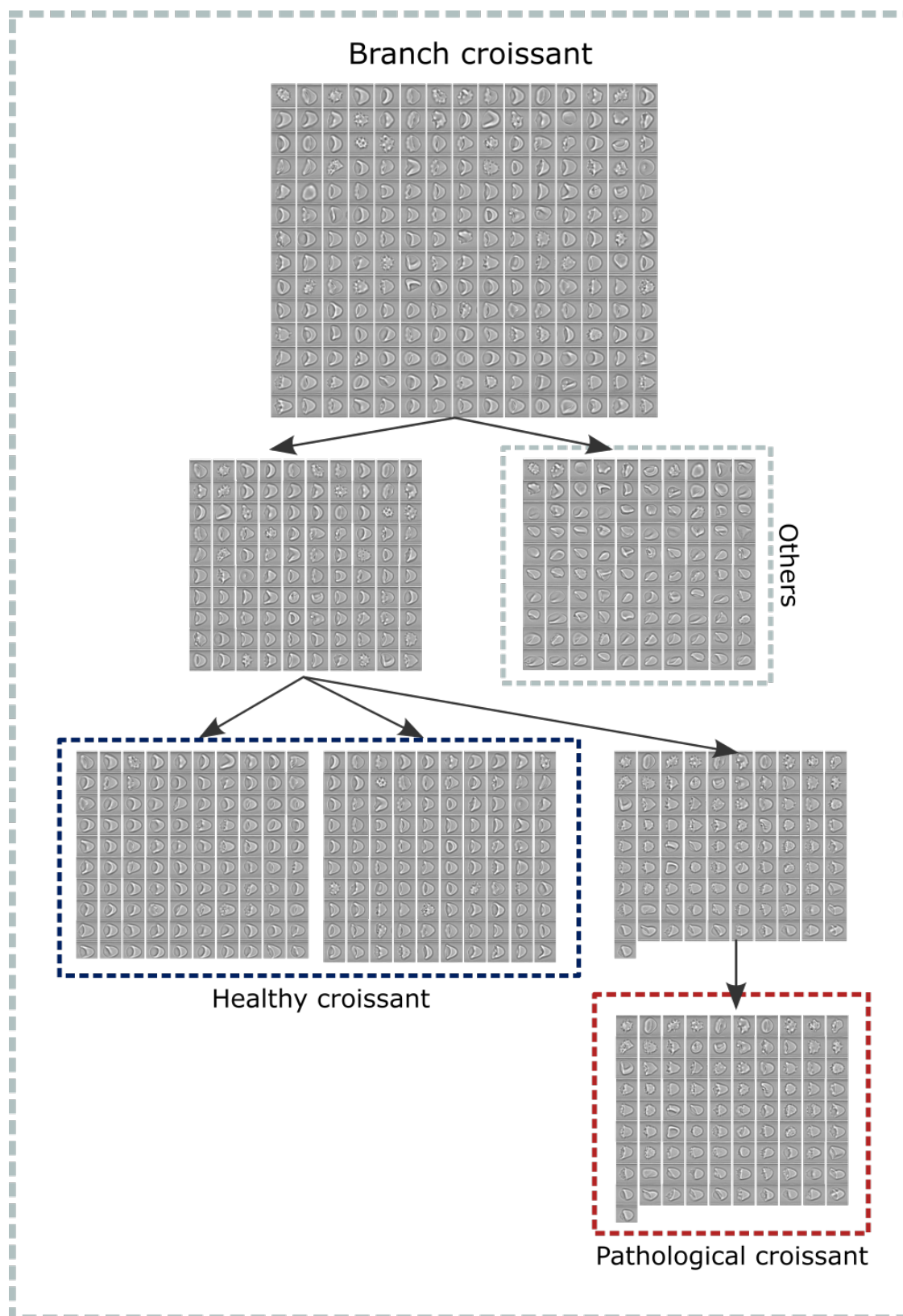


Fig. 3.6: The croissants classification is applied to a set of RBC images, resulting in an example of classification outcomes.

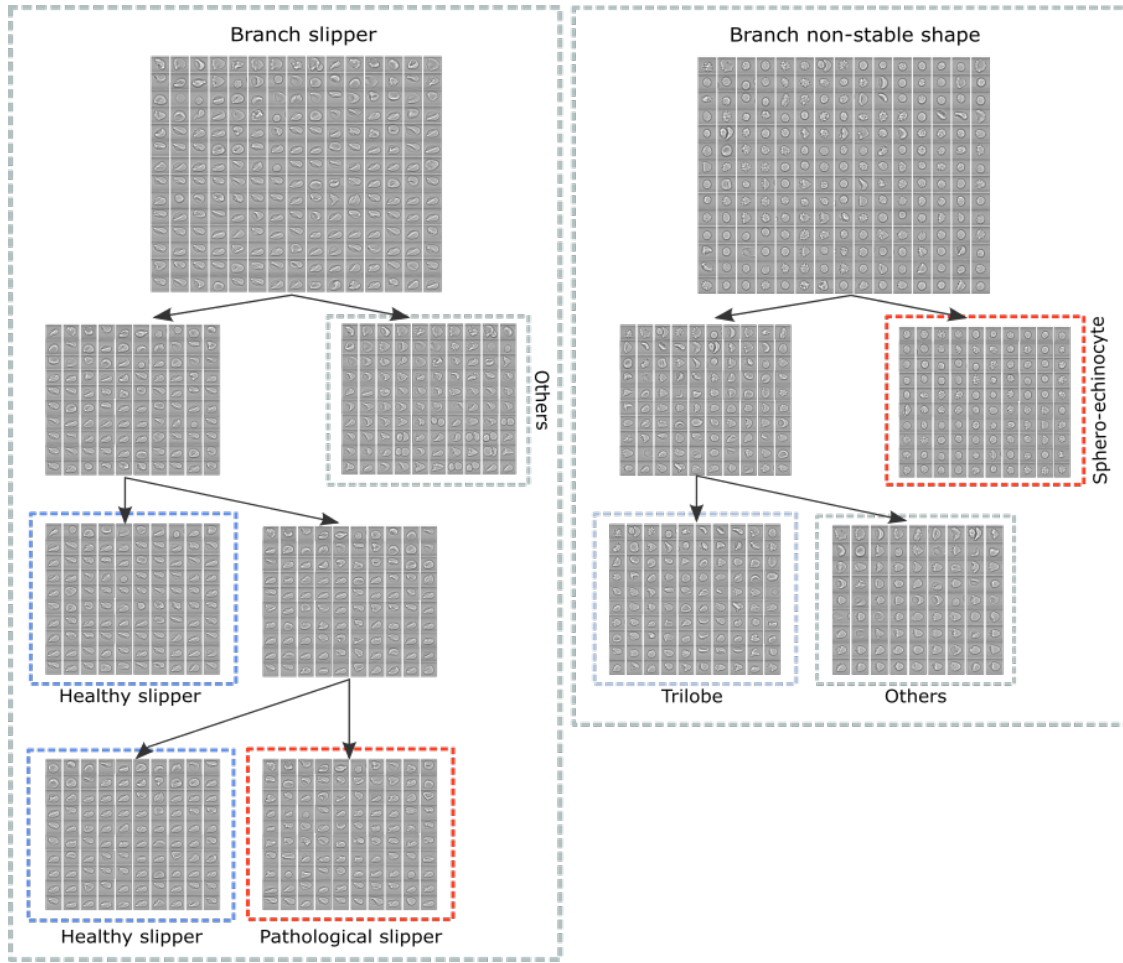


Fig. 3.7: The slipper and non-stable shape classification is applied to a set of RBC images, resulting in an example of classification outcomes.

161 images were correctly assigned to the others class, while 837 remained in the croissant class. In the subsequent stage, aimed at distinguishing between symmetric croissants, large croissants, inclined croissants, and pathological croissants, there was considerable confusion not only between inclined croissants and pathological croissants but also among various shapes of healthy croissants and pathological croissants, resulting in an approximate classification error of 30%. In the final stage, where inclined croissants were incorrectly differentiated from pathological croissants, no healthy croissants were identified. Overall, the performance of this branch was unsatisfactory, as it was not possible to clearly distinguish between healthy croissant shapes and pathological ones at the end of the tree process.

In the branch dedicated to unstable forms, a total of 2232 RBCs were classified as neither croissants nor slippers. Among these images, 1964 were identified as

sphero-echinocytes and 187 as trilobes in the second stage of classification. In the third stage, a significant portion of the cells initially labeled as trilobes (79.7%) were misclassified. This highlights the considerable confusion between the shapes of sphero-echinocytes and trilobes. Regarding the Sphero-echinocyte cells, approximately 11% of the images were misclassified at the end of the third stage, with confusion arising between the "other" shape and sphero-echinocytes shape. The third branch, dedicated to slippers, demonstrated the best performance among the branches. Out of the 2913 images initially classified as slippers, 16.3% were misclassified during the application of thresholds in the second stage of the tree. Among the remaining images classified as slippers, only 2% were misclassified in the third stage. In the case of pathological slippers, a significant portion (87.4%) remained as healthy slippers in the subsequent stage, while 50% of the RBCs identified as pathological were, in fact, healthy. These findings indicate that the tree-CNN approach did not achieve satisfactory results. A more robust and effective methodology is required to address these challenges.

### 3.1.4 Transfer-learning

Unlike the CNN-tree design, which involves hierarchical growth and adaptation, the transfer learning technique provides a more flexible and efficient method for integrating prior knowledge into new tasks. By fine-tuning a pre-trained model to the specific task of RBC classification, it becomes possible to achieve improved performance, with reduced misclassification between RBC shapes, using fewer data samples and computational resources. Rather than starting from scratch as in the CNN-tree approach, transfer learning leverages the learned representations from a related task or a large dataset, which can greatly enhance the accuracy and efficiency of the classification process for RBCs.

The chosen pre-trained model was YOLO (You Only Look Once) [108,109], version five, which is a pioneering object detection model. YOLO revolutionized object detection by integrating bounding box prediction with class labels in input images, and it's renowned for its ability to deliver real-time, high-speed, and high-precision results. YOLO's architecture is composed of three key components: a base network, a neck network, and a head network. The base network plays a crucial role in extracting meaningful features from the input image. It utilizes the CSPDarknet53 (Cross Stage Partial Network) [109,110] backbone, which consists of multiple convolutional layers and residual links. These components work together to facilitate efficient feature extraction at different scales, enhancing the model's ability to capture diverse visual patterns. To further improve feature representation and detection accuracy, a neck network is incorporated. The PANet (Path Aggregation Network) [109,111] neck is employed, leveraging side links and feature fusion

to combine features from various scales. This mechanism enables the model to effectively handle objects of different sizes, resulting in improved object localization and classification performance. The head network takes charge of the final object detection predictions. It consists of convolutional layers followed by a final detection layer. Within the detection layer, the model predicts the coordinates of the bounding box ( $x$ ,  $y$ , width, height), objectivity (confidence) scores, and class probabilities for different anchor boxes at distinct spatial locations. By making predictions at different grid scales, the model can effectively capture objects of varying sizes, providing comprehensive and accurate detection results. Such architecture is exemplified in Figure 3.8.

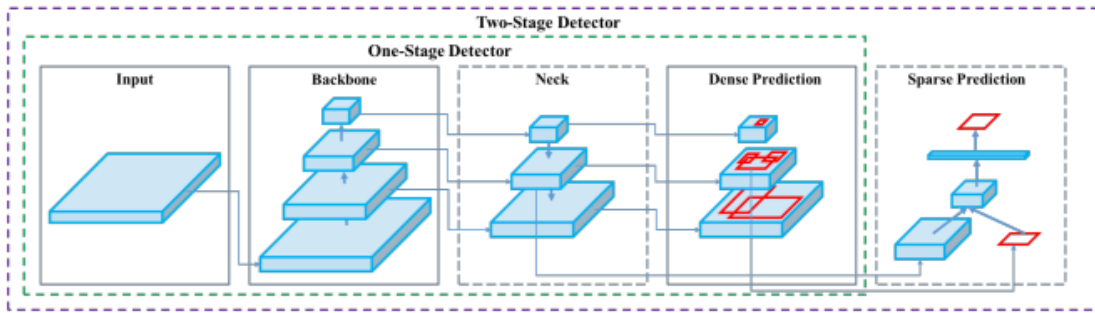


Fig. 3.8: The trained model architecture is structured with three main components: the Backbone, Neck, and Head. Taken from [109].

Considering the specific architecture of the selected neural network, a thorough process is implemented to ensure the effective detection and classification of the RBC data. Thus, the training process begins by labeling the dataset with the different RBC shapes. However, it is not sufficient to solely label the images with the corresponding class labels. It is also necessary to create bounding boxes that precisely indicate the location of the RBC in each image.

In the specific case of the dataset, where the images represent single cell images, the image itself can be considered as the bounding box. This eliminates the need for additional annotation tools or manual bounding box creation. Instead, a standardized etiquette can be used to label the images uniformly. Thus, the same fixed etiquette, such as "shape class 0.5 0.5 1 1," is assigned to all images in the dataset. This etiquette signifies that the entire image is treated as the bounding box, with the coordinates (0.5, 0.5) representing the center of the image and the dimensions (1, 1) representing its width and height. This simplifies the labeling process and ensures a standardized representation of the single cell images, allowing the model to learn from the data accordingly.

Once this labeling process is completed for all the images in the dataset, the dataset needs to be organized in a specific format that is compatible with the chosen pre-

trained model. This format involves creating a JSON file for each image, which includes the coordinates of the bounding box as well as the corresponding class labels. By structuring the dataset in this way, it ensures that the model can accurately identify and locate the RBC objects during the training phase. Furthermore, the dataset is divided into training and validation sets to assess the model's performance during the training process. As the dataset and training parameters (image size: 640, batch size: 8, epochs: 300) are prepared, the training process starts. The pre-trained model's weights are loaded, and the model is trained using the RBC dataset. The model utilizes CNNs and is optimized for error reduction using Stochastic Gradient Descent (SGD) and Adam. SGD modifies function parameters proportionally to its gradient to minimize loss, while Adam adapts learning rates by combining SGD principles with first and second order moments, allowing more dynamic and effective parameter adjustments in the neural network.

### 3.1.5 Training and validation set

As supervised learning is used in this study, which requires labels for each cell for the training process, a random subset of 6111 training images was selected from the original image data set for manual classification according to the parameters specified in [112]. The training and the validation set consists of this group of images and their corresponding labels. The identified classes can be seen in Figure 3.9. The CNN was trained on a dataset of RBCs that was divided into 10 distinct classes, allowing for accurate classification based on their morphology as observed in the experiments.

Each class was identified by specific characteristics and assigned a unique nomenclature, as follows:

- (i) Normal croissant shape: this class consists of RBCs that exhibit a symmetrical and centered shape with a concave front and a convex back, as explained in item 1.2.1.
- (ii) Tilted croissant shape: this class includes the croissant-shaped RBCs that are not aligned with the Y-axis of the microfluidic channel. However, it is important to note that this class serves as an auxiliary category and is not included in the phase diagram.
- (iii) Sheared croissant shape: Similar to the previous class, this category is also considered as an auxiliary class, and comprises croissants with slight deformations. The croissants in this class still possess a symmetrical shape but have an elongated "tail".
- (iv) Slipper shape: This class, as explained in section 1.2.1, consists of RBCs that

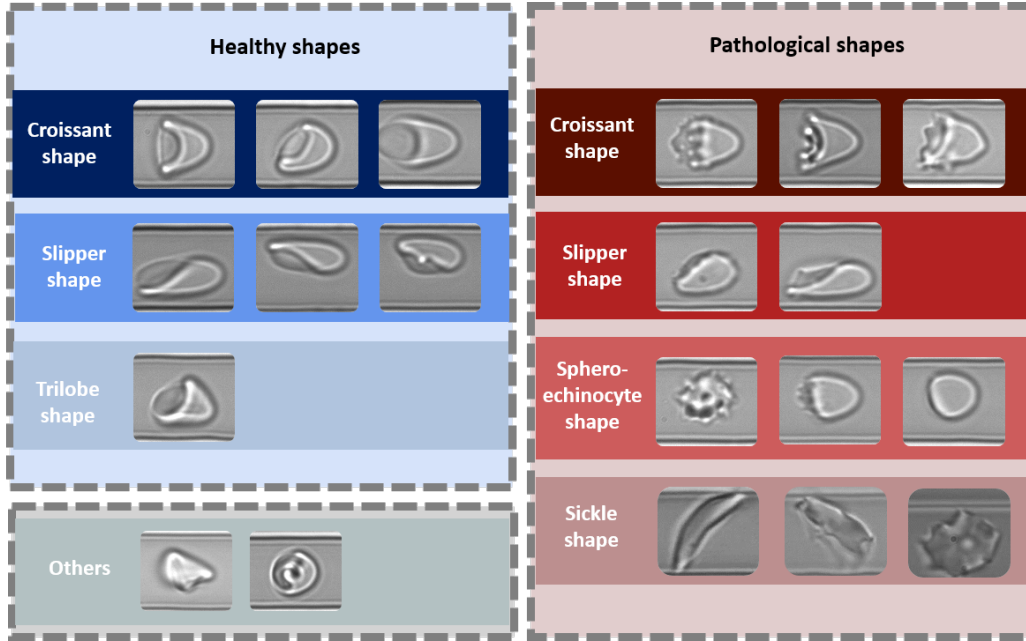


Fig. 3.9: The dataset includes healthy RBC shapes such as normal croissants, tilted croissants, sheared croissants, slippers, tank tread slippers, and trilobes, which are described in the blue box. The reddish frame displays pathological croissants and slippers, as well as Sphero-echinocytes and sickle cells, which are found only in pathological samples. Additionally, the gray frame shows examples of RBC classified as other as they do not belong to any of the previous classes.

are off-center and asymmetric, with a pointed front and a flat back, and are positioned close to the walls of the channel.

- (v) Trilobe shape: this category includes RBC images exhibiting large lobes on their surface, in this case, three lobes and their rotation around their own axis while crossing the channel.
- (vi) Pathological croissant shape: this class includes RBC images that exhibit characteristics of the three previous croissant-classes, but with visibly damaged cellular membranes.
- (vii) Pathological slipper shape: this class includes RBC images that exhibit slipper-class but with visibly damaged cellular membranes.
- (viii) Sphero-echinocytes shape: this class includes a type of RBC that are smaller in size compared to other RBC shapes, but are also characterized by rounded shapes with spike deformations on their surface.

- (ix) Sick cell shape: This class encompasses the RBCs that undergo deformation in their membrane due to the crystallization of HbS (as described in section 1.2.3.4 Sick Cell Disease and illustrated in Figure 1.4).
- (x) Others shape: this class of images contains a variety of red blood cell forms that do not fit into the previous classes.

It should be noted that the class of pathological slippers was observed in the training or validation dataset; however, due to its rarity, it was not included in the training set. When this class appeared, it was identified manually after the initial classification performed by the CNN. This adjustment was essential due to the training requirements for ANNs, including the CNN utilized in this investigation, which require a consistent number of images per class (a minimum of 2.5k images in this instance). Despite employing augmentation techniques, achieving this balance was unattainable for the pathological slippers. Furthermore, images within the same class must exhibit a uniform visual appearance. Failure to meet this criterion, although classified identically in human interpretation and the literature (as seen in the case of all the different sick cell shapes), makes their categorization as the same class of images for ANNs unfeasible. Consequently, manual identification of these discrepancies became also necessary.

Additionally, it is important to note that a separate class was not created specifically for acanthocytes. Instead, their detection was achieved through the classes of pathological croissants and spherocytocytes. Since these classes encompass a wide range of shapes, the acanthocyte shapes closely resembled those already included, obviating the need for a distinct class. Figure 3.10 showcases RBC images captured at different velocities from MLS, CHAC, and HD patients, demonstrating instances where acanthocytes were identified.

Furthermore, considering the extensive spectrum of membrane deformities resulting from HbS crystallization within the SCD class (see Figure 1.4), and due to the limited number of experiments conducted during the training of the neural network, the sick cell class was not included in the training process for practical reasons. Instead, sick cells present in the dataset were identified and manually classified, similar to the pathological slippers.

To improve the robustness of the model and prevent overfitting, data augmentation techniques such as flipping (up/down, left/right) and brightness adjustment were employed to expand the training set. A detailed description of these application techniques in the training set can be found in Table 3.3. Thus, to train the model, we used a total of 10,990 images and ran the training process for 300 epochs, while employing the SGD optimizer with a learning rate of 0.01 and confidence threshold at 90%. In addition, 4,943 images were used for validation.



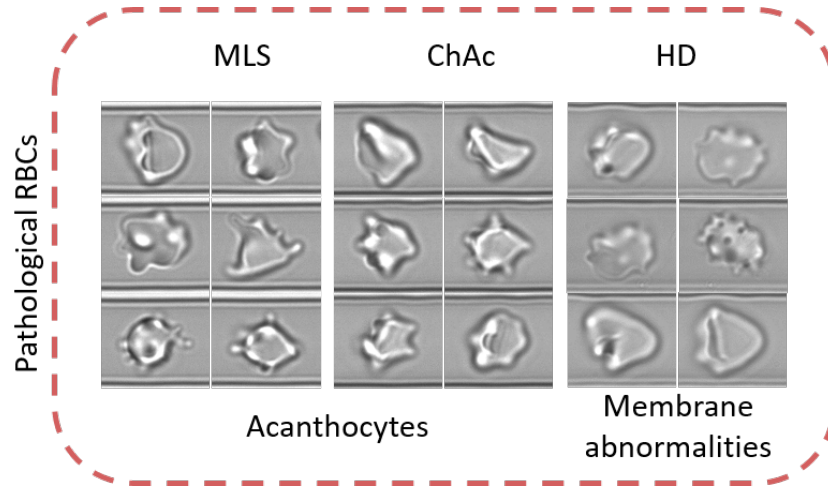


Fig. 3.10: Pathological-shaped RBCs images from MLS, ChAc, and HD patients. Adapted from [9]

. See section Author's declaration of contributions, DECLARATION 2.

### 3.1.6 Training and validation metrics

A confusion matrix is an  $N \times N$  matrix employed to assess the classification model's performance, where  $N$  corresponds to the number of target classes. It juxtaposes the actual target values (rows) with the predicted ones (columns) generated in the classification. The confusion matrix is constructed using four key combinations of predicted values: true positives (TP), false positives (FP), true negatives (TN), and false negatives (FN). These values are interpreted as follows:

- TP: This happens when the prediction is positive for the actual class of the classified object.
- TN: Occurs when the prediction is negative for classes other than the actual class of the classified object.
- FP: Occurs when the prediction is positive for classes other than the actual class of the classified object, representing a type 1 error.
- FN: Occurs when the prediction is negative for the actual class of the classified object, representing a type 2 error.

In cases such as the one presented in this study, where there is a multi-class classification problem, the values of TP, TN, FP, and FN are calculated class by class, as an example illustrated in the Figure 3.11.

Observing the confusion matrix derived from the YOLO model's classification of the RBC images, it is evident that the classification performance is quite satisfactory.

Tab. 3.3: Image Details by Class

Class	Number of images	By rotation	By brightness increase	By brightness decrease	Total of images
Normal Croissant	645	Yes	No	Yes	5160
Tilted Croissant	265	Yes	Yes	Yes	4757
Sheared Croissant	1052	Yes	No	Yes	4208
Slipper	2300	No	No	Yes	4600
Trilobe	276	Yes	No	Yes	4692
Pathological Croissant	315	Yes	Yes	Yes	2520
Sphero-Echnocyte	194	Yes	No	Yes	5684
Others	1064	Yes	No	Yes	4256
<b>TOTAL</b>					<b>10,990</b>

The correct classification rates (TP) for most classes exceed 80%, as indicated by the values along the main diagonal of the matrix in Figure 3.12.

However, while the model was capable of achieving the required task, the Sphero-Echnocyte and "others" classes had lower accuracy rates due to the significant variation in shapes within each category. Examples of RBCs from the "others" category are presented in Figure 3.13 to illustrate this variability.

Furthermore, high misclassification rates were observed among the three sub-classifications of healthy croissants. However, since these sub-classes are only used to identify missing croissants in the dataset and are auxiliary, they will be merged into a single class called "Croissant" in the next stage. Thus, these sub-classes will be retained only for the purpose of illustrating the multi-class performance of the proposed CNN and will be treated as a single class in the final evaluation of the model.

The model's performance was evaluated using various metrics derived from the TP, TN, FP and FN values obtained from the confusion matrix. Precision, defined in Equation 3.5, was used as the first metric to measure the model's reliability in classifying positive samples. It determines the proportion of correctly classified positive samples out of all samples predicted as positive. The second metric, called recall, defined in Equation 3.6, measures the model's ability to detect positive

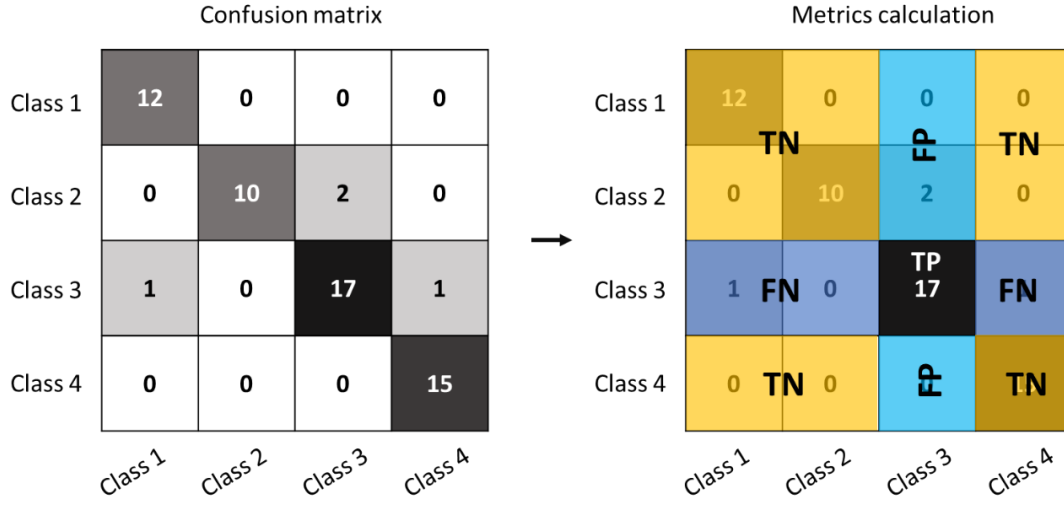


Fig. 3.11: The table on the left shows an example of a confusion matrix for a 3-class classifier, while the table on the right shows how the TP, TN, FP and FN metrics are calculated for class 3.

samples, also taking in account the false negatives. It determines the proportion of correctly classified positive samples out of all samples. Finally, the F1 score, defined in Equation 3.7, measures the harmonic mean of precision and recall, providing an overall measure of the model's performance.

$$\text{Precision} = \frac{T_P}{T_P + F_P} \quad (3.5)$$

$$\text{Recall} = \frac{T_P}{T_P + F_N} \quad (3.6)$$

$$\text{F1} = \frac{2 \times (\text{Precision} \times \text{Recall})}{\text{Precision} + \text{Recall}} \quad (3.7)$$

Therefore, A multi-class precision-recall curve was generated in Figure 3.14, showing good performance, with the AUC (area under the curve) almost reaching 1 in all cases. The AUC also represents the Average Precision for each class. The micro-parameters analysis considering the auxiliary classes will not be further elaborated since all the classes are equally significant for the final model classification.

Predicted	Normal Croissant	63.30%	4.42%	6.25%	-	-	1.92%	-	-
	Tilted Croissant	32.98%	93.81%	3.96%	-	-	4.30%	-	3.10%
	Sheared croissant	1.60%	1.77%	80.00%	-	-	4.30%	-	2.14%
	Slipper	-	-	-	91.12%	-	-	-	4.06%
	Trilobe	-	-	-	-	89.82%	-	6.25%	14.42%
	Pathological Croissant	1.60%	-	6.46%	-	-	85.07%	5.00%	7.37%
	Sphero-Echnocyte	-	-	-	-	1.25%	-	74.37%	0.96%
	Others	0.53%	-	2.92%	8.69%	8.93%	3.73%	14.37%	66.88%
		Normal Croissant	Tilted Croissant	Sheared Croissant	Slipper	Trilobe	Pathological Croissant	Shepro-Echnocyte	Others
		True							

Fig. 3.12: The confusion matrix displays the percentage of cells that were correctly classified (true positives) along the main diagonal, while the percentage of false negatives and false positives are shown in the rows and columns, respectively.

Table 3.4 presents the performance of the model, showing that all object categories are detected with more than 80% accuracy. Moreover, the model achieved an overall precision and recall higher than 85%. A lower precision indicates that the model sometimes predicts a class that is not present in the image. On the other hand, a higher recall indicates that if a class is present in the image, there is a high probability that the model will predict that class. The relatively higher recall of the slipper and trilobe class (92.8% and 94.5%, respectively) can be attributed to the high similarity between the sample shapes. However, the low recall of the "others" class (67.8%), as mentioned before, is due to the high variability of samples in this class. The F1-score metric, which considers both precision and recall, provides an overall assessment of the model's performance. The F1-score of 85.3% indicates that the model achieved a good result.

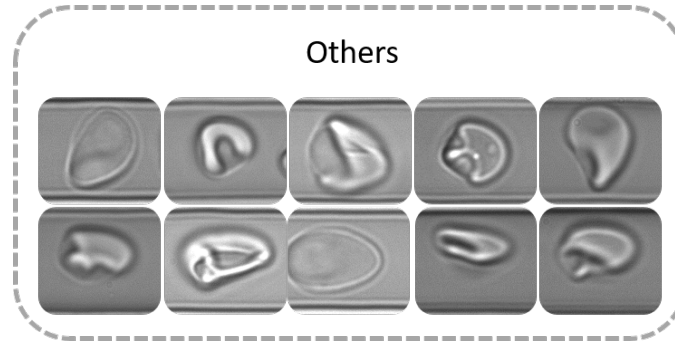


Fig. 3.13: RBC images selected from the CNN training set to illustrate the significant variation in shapes present within the "Others" class.

Tab. 3.4: Standardized validation metrics of the trained CNN for each cell shape category and global result.

Metrics	<i>Croissant</i>	<i>Slipper</i>	<i>Trilobe</i>	<i>Pathological Croissant</i>	<i>Sphero-Echnocyte</i>	<i>Others</i>	<i>Global average</i>
Precision	85.23%	99.90%	96.20%	93.60%	91.90%	80.90%	85.20%
Recall	84.40%	92.80%	94.50%	81.40%	70.40%	67.77%	85.40%
F1	84.81%	95.45%	89.72%	85.89%	79.42%	72.22%	85.30%

## 3.2 Biological Investigation

To conduct a comprehensive analysis of the experimental results obtained using the methodology proposed in the previous section, it was done a detailed investigation into the flow behavior of RBC disorders. This study specifically involves the development and utilization of phase diagrams that encompass all the various morphologies of RBCs detected through AI.

The RBC characteristic structure plays a vital role in enabling a comprehensive understanding of the intricate interactions between their distinct morphologies and the surrounding fluid characteristics, particularly factors like velocity. Within this apparently simple structure, internal characteristics play a fundamental role [11,113], adding layers of complexity to our understanding. The large Surface Area-to-Volume Ratio, the intrinsic link between the hemoglobin presence and cytoplasmic viscosity and also the viscoelastic properties of the cell membrane, governed by the protein composition of the membrane skeleton, play a crucial role in upholding the distinctive discoid shape of the red blood cell, providing it with deformability,

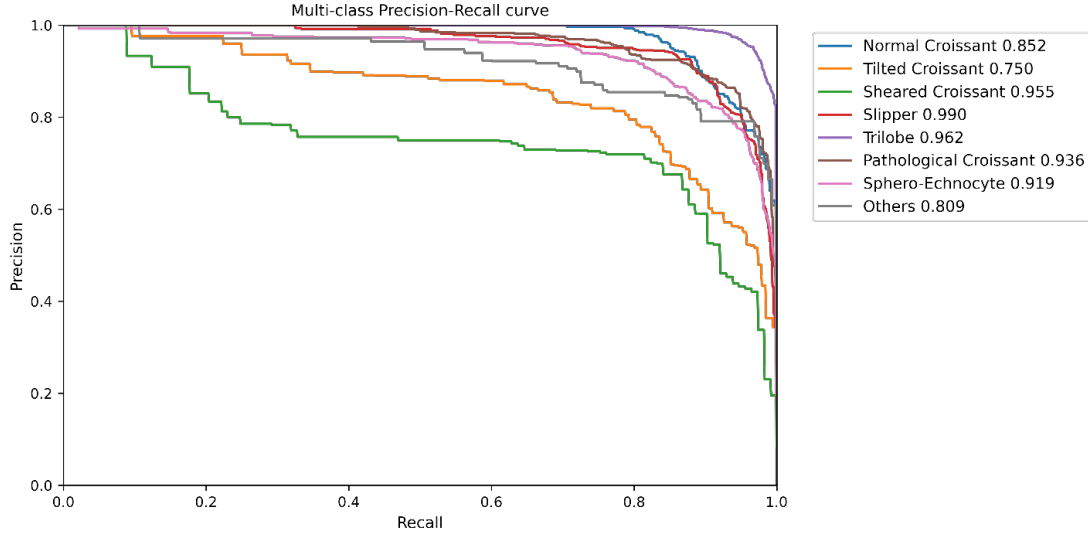


Fig. 3.14: The Precision-Recall curve for each category. The area under the curve indicates the Average Precision, calculated in the legend. A higher Average Precision indicates better detection performance.

flexibility, and durability. The interplay of these factors enables red blood cells to undergo deformation, a crucial process for their effective flow through the intricate network of microvessels. The manner in which the RBC membrane deforms, responding to the flow itself, becomes an indicative marker of the cell's functional status [11]. This deformation pattern is subject to change, especially in disease states or in response to environmental stimuli, contributing valuable insights into the dynamic health of the cell. By closely examining the RBC morphology and its relationship with fluid dynamics, valuable insights can be gained regarding the behavior and deformability of the RBC. The phase diagram obtained through this RBC study acts as a critical link to RBC deformability. It provides a visual representation of the different RBC morphologies observed under varying conditions, and their corresponding fluid characteristics. By mapping out these relationships, the phase diagram holds significant potential as a key component in the development of a characterization tool designed to detect pathological parameters in the blood.

### 3.2.1 Control

In order to gain insights into the dynamics of various diseases, it is essential to first investigate the conditions in a healthy individual. Thus, a preliminary step involves studying the normative conditions of healthy individuals.

For this, blood samples were collected from 15 different healthy individuals. The proposed designed protocol was carefully implemented, following which a final sample of 1ml PBS containing 0.1% BSA with 0.05% RBC concentration was prepared for each control. These samples were then subjected to experimentation using the proposed experimental setup, which involved applying pressures ranging from 100 to 1000 mbar, in a 100 mbar step. Subsequently, the collected data was analyzed using an AI-based toolbox developed specifically for this study, leading to the generation of a phase diagram. The Figure 3.15 depicts the phase diagram obtained from the analysis of three control samples. This diagram serves as a valuable visual representation of the relationships between different velocities, shedding light on the normative conditions and dynamics of healthy blood.

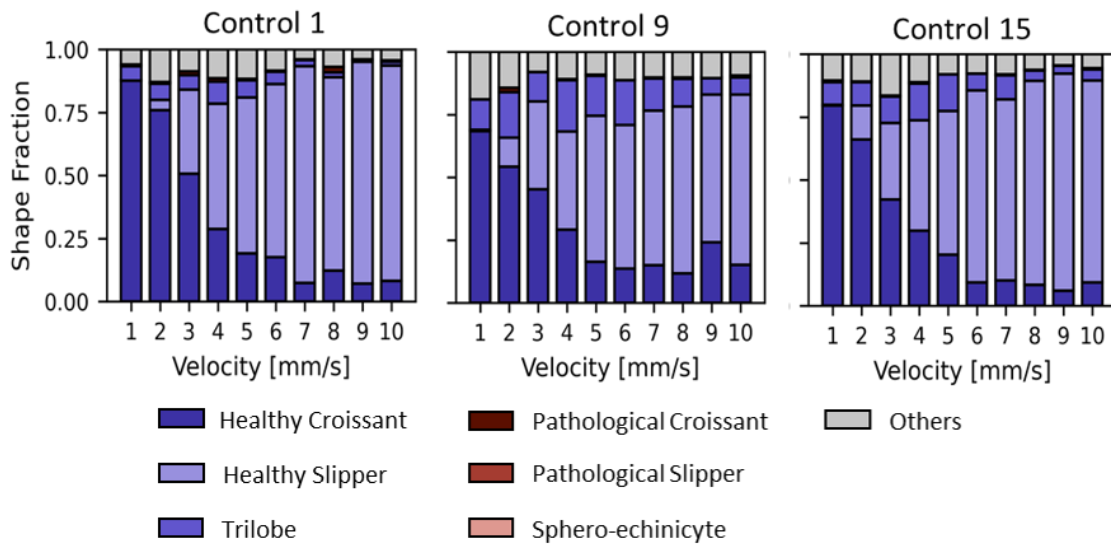


Fig. 3.15: The phase diagram for controls 1, 9, and 15 (representative selected). The x-axis represents the velocities at which the experiments were conducted, while the y-axis represents the fraction of each RBC shape, providing a visual representation of how the distribution of RBC shapes changes with varying velocities.

The phase diagram of a healthy individual, as observed in controls 1, 9, and 15, exhibits specific characteristics. The dominant fractions in the phase diagram correspond to the stable healthy shapes, namely the healthy croissants and healthy slippers. It is expected that the largest fraction of healthy croissants will be found at the lowest speeds, indicating their prevalence under conditions of reduced flow. Conversely, for healthy slippers, their highest concentration is showed at higher speeds, indicating their stability under increased fluid velocities. In contrast, the occurrence of pathological shapes in the phase diagram is relatively minimal compared to the healthy forms. The pathological croissant or slippers shapes may

arise due to factors such as the storage time or transportation method of the blood samples. Furthermore, the phase diagram also reveals the presence of other forms that are not explicitly described in the existing literature. These "others" represent distinct shapes that are observed in lower concentrations across all velocities. It's important to note that all RBCs from the control samples are healthy, even those displaying deformations. However, in order to simplify and standardize in the study, the terminology "pathological cells" has been retained. This is because the deformities observed in them resemble those found in blood samples from patients with diseases.

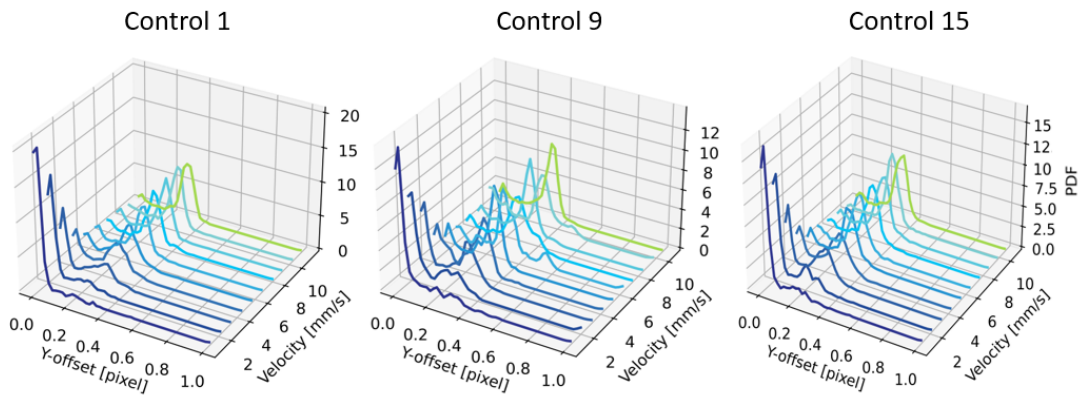


Fig. 3.16: The y-offset distribution (PDF) for different velocities in the phase diagram was analyzed for control samples 1, 9, and 15. At a velocity of 1mm/s, the distribution peak is observed at zero, while at 10mm/s, the peak is shifted to a value greater than zero for the three controls.

Overall, the phase diagram provides valuable insights into the distribution of RBC shapes in healthy individuals, with dominant fractions belonging to stable healthy shapes, limited occurrence of pathological ones, and the presence of "others" class. These findings contribute to our understanding of RBC dynamics and have the potential to aid in the development of characterization tools for assessing blood parameters and detecting abnormalities. Moreover, using the phase diagram as a basis, the distribution of the absolute value of the value of the position y offset was computed for all RBCs at each velocity point on the phase diagram. In the case of healthy individuals, it is expected that at low velocities, the RBCs would exhibit a healthy croissant shape, characterized by stable forms flowing centrally through the microfluidic channel. Conversely, at high velocities, slipper-shaped RBCs are more prevalent, with their center of mass shifted either upward or downward along the microfluidic channel. Figure 3.16 displays the probability density distributions (PDFs) of RBCs for controls 1, 9, and 15 across a range of mean velocities from



1 mm/s to 10 mm/s. The samples selected to demonstrate the controls were as follows: the first sample (Control 1), the last sample (Control 15), and a mid-point sample (Control 9).

As anticipated, the pdfs reveal that at low velocities, the majority of RBCs assume a croissant shape, aligning themselves in the center of the channel, resulting in  $|y\text{-offset}|$  values around 0. On the other hand, at higher velocities, slippers become the predominant shape, exhibiting an off-centered equilibrium position with  $|y\text{-offset}|$  values greater than 0. As the velocity increases between these two extremes, the distributions progressively shift from an equilibrium position from  $|y\text{-offset}| = 0$  to an equilibrium position with  $|y\text{-offset}| > 0$ . The distribution of RBC  $y\text{-offset}$  positions at different velocities serves as a characteristic indicator of single-cell flow in microchannels. It provides valuable biomechanical insights into the behavior of RBCs and can serve as a reference point for detecting pathological changes in RBC flow patterns at specific cell velocities.

In addition to the inherent flow parameters, the concept of the shape ratio was introduced to quantify the proportion of pathophysiological RBC shapes relative to healthy ones. The shape ratio provides a quantitative measure of the presence and significance of pathological RBC shapes. In the case of a healthy control, where the occurrence of pathological shapes is minimal, the shape ratio is significantly less than one, indicating a predominance of healthy RBC shapes. Figure 3.17 illustrates the shape ratio for the 15 controls, displayed on a logarithmic scale.

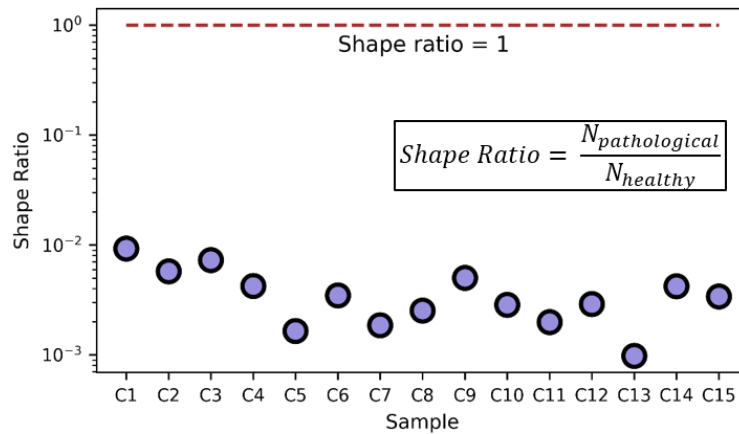


Fig. 3.17: The shape ratio for the 15 analyzed controls plotted in logarithmic scale, indicating the proportion of pathological RBCs to healthy RBCs. The definition red line represents the point where the number of pathological RBCs equals the number of healthy RBCs.

The shape ratio values are compared against a reference red line set at 1. When

the value equals 1, it indicates an equal presence of healthy and pathological cells in the same sample, signifying a substantial proportion of sick RBCs. In such cases, the sample cannot be classified as healthy. The logarithmic scale allows for a clear visualization of the smallness of the shape ratio values in comparison to the reference line. This emphasizes the relatively low occurrence of pathophysiological RBC shapes in the healthy controls, as indicated by the shape ratio values falling significantly below the threshold of 1. The shape ratio values are compared against a reference red line set at 1. This emphasizes the relatively low occurrence of pathophysiological RBC shapes in the healthy controls, as indicated by the shape ratio values falling significantly below the threshold of 1.

Therefore, through a comparison between the phase diagram, the y-shift distribution, and the shape ratio with the established standards for healthy individuals, any deviations from these norms can be identified. These deviations have the potential to serve as characterization markers for detecting abnormal RBC flow behavior, which could be indicative of various pathologies. By analyzing the deviations and understanding their significance in relation to specific health conditions, valuable insights can be gained, leading to improved characterization capabilities and a better understanding of the underlying mechanisms contributing to these deviations. Ultimately, this knowledge can aid in the early detection and management of various diseases related to RBC flow abnormalities.

### 3.2.2 COVID-19

First and foremost, it is important to clarify that the results presented in this section are based on the research conducted by Recktenwald, S. M. and *et al.*. My specific contribution to the work, along with those of the other co-authors, is detailed in the Author's Statement of Contributions section, under STATEMENT 3.

The next phase of the study focused on evaluating the flow properties of RBCs in individuals with COVID-19. It is known that COVID-19 can lead to significant alterations in the physical and rheological properties of RBCs, including their shape, size, and deformability. These changes are believed to play a role in the severity of the disease [12]. To investigate this further, the flow properties of RBCs were examined in severe COVID-19 patients who were admitted to the intensive care unit. The study followed a predefined protocol to assess the RBCs in both autologous (patient's own) and allogeneic (from other donors) plasma. This involved analyzing four different sample groups: (i) control RBCs in control plasma (CinC), (ii) control RBCs in patient plasma (CinP), (iii) patient RBCs in patient plasma (PinP) and (iv) patient RBCs in control plasma (PinC). Figure 3.18 provides an

overview of the scheme used to combine the different samples.

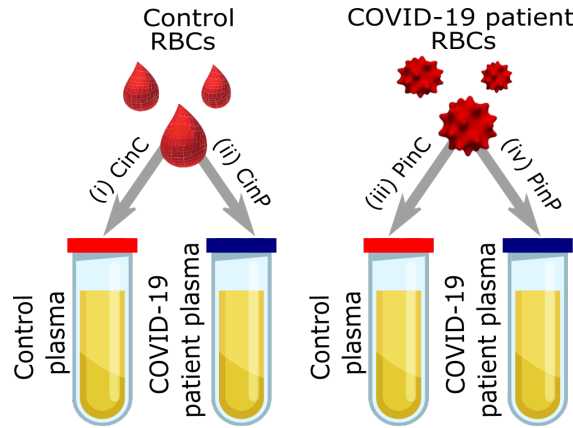


Fig. 3.18: Overview of the four sample groups, referred to as ‘X RBCs in X plasma’, e.g. CinC for Control RBCs in Control plasma, and so on for PinP, PinC, and CinP.

The sample preparation process followed the established protocol, involving the use of 1ml of plasma with a hematocrit of 0.05%. In total, we obtained 5 control samples (CinC), 14 patient samples (PinP), and 18 exchange plasma samples (CinP and PinC). All 36 samples underwent experimental testing. To illustrate one of these combinations, Figure 3.19 shows the phase diagram representing the interaction between RBCs from a control sample in its own plasma (i), RBCs from a COVID-19 patient in its own plasma (iv), RBCs from the control sample in the patient’s plasma (ii), and RBCs from the patient in the control’s plasma (iii).

The CinC sample (i) displays the typical behavior of healthy RBCs in a healthy plasma environment. The RBCs in plasma reach velocities of up to 6 mm/s, with the majority of croissant-shaped RBCs observed at lower velocities. As the velocity increases, the concentration of croissant-shaped RBCs decreases, while the concentration of healthy slippers-shaped RBCs increases. There is also a minimal presence of pathological cells, which may be attributed to storage or transportation factors affecting the sample. In the PinP sample (iv), which consists of RBCs from COVID-19 patients in contact with their own plasma, distinctive pathological shapes of croissants and slippers can be observed, accompanied by pronounced spicules on the cell membrane. Additionally, the phase diagram of the PinP sample reveals the presence of RBC in the sphero-echinocyte shape, representing irreversible transformations of RBCs. Overall, the phase diagrams for samples CinC and PinP highlights a significant difference in the distribution of RBC shapes between healthy controls and COVID-19 patients, considering a predominance of pathological shapes and sphero-echinocytes at all velocities in the PinP sample.

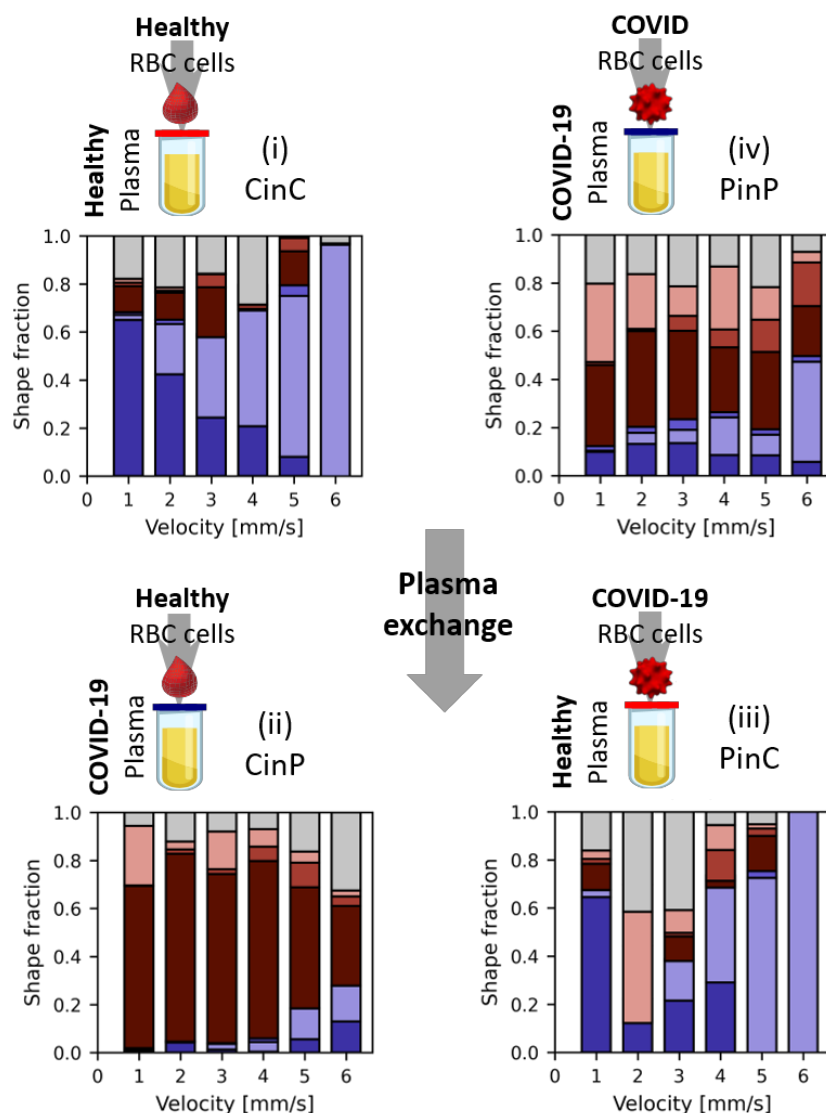


Fig. 3.19: Representative shape phase diagrams for two donors, (i) one control and (iv) one patient, in the four sample groups. The upper panels (i, iv) depict the phase diagrams of the donors in autologous plasma, while the lower panels (ii, iii) illustrate the same donors in allogeneic exchanged plasma. Adapted from [12].

However, when patient RBCs undergo plasma exchange with healthy control plasma, what means sample PinC, they exhibit a shape reversal, resembling the phase diagram of healthy controls. On the other hand, control RBCs in allogenic plasma exchanged from COVID-19 patients (sample CinP) experience a notable deterioration in their shape, as evident from the phase diagram. This behavior is also

evident in the shape ratio of the four samples, as shown in Figure 3.20.

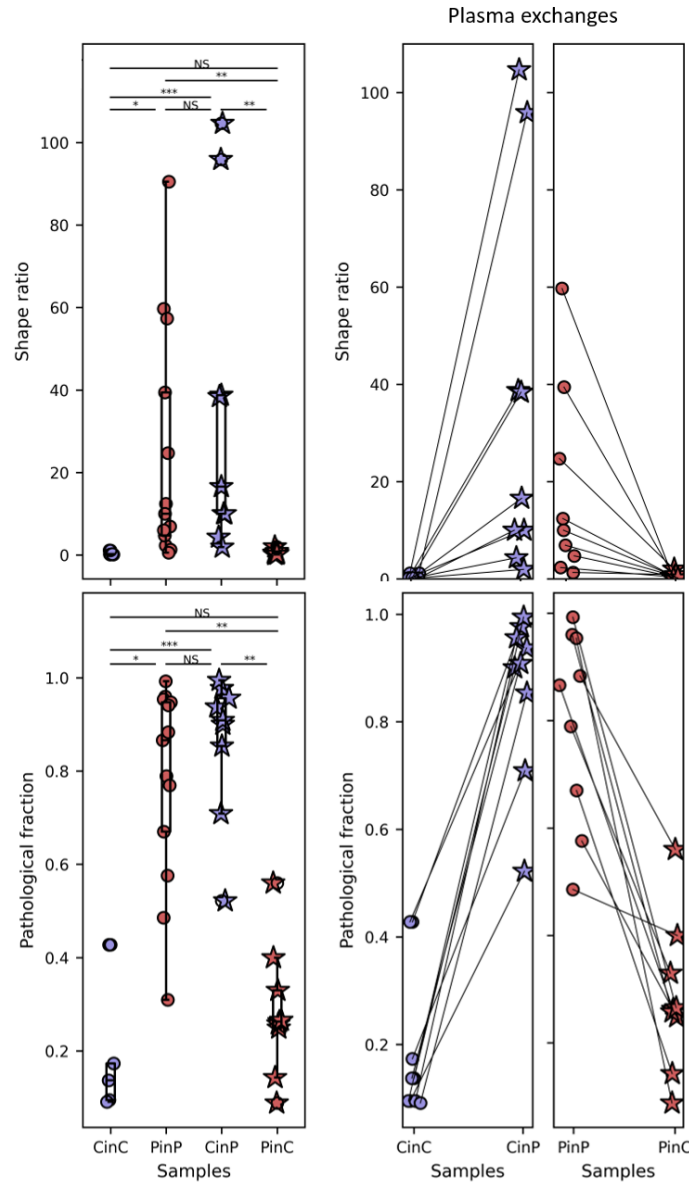


Fig. 3.20: The shape ratio (\* refers to a significance level of  $p < 0.08$ , \*\* to  $p < 0.03$ , \*\*\* to  $p < 0.01$  and NS stands for not significant.) and pathological fraction (\* refers to a significance level of  $p < 10^{-6}$ , \*\* to  $p < 10^{-8}$ , \*\*\* to  $p < 10^{-7}$  and NS stands for not significant.) for all samples, revealing a similar behavior between the CinC and PinC samples, as well as between the PinP and CinP samples. Adapted from [12].

The shape ratio, which quantifies the proportion of pathologically shaped cells

relative to healthy cells, provides insight into the extent of pathological changes in RBC shape. In the case of healthy controls (CinC), the shape ratio is consistently low. However, for patients with COVID-19 (PinP), the shape ratios are consistently greater than one, indicating a higher prevalence of pathological RBC shapes. When the RBCs from the healthy controls are suspended in the plasma of COVID-19 patients (CinP samples), there is a noticeable increase in the proportion of pathological RBC shapes compared to their original control condition (CinC), resulting in higher shape ratio values. Conversely, when the RBCs from COVID-19 patients are suspended in the plasma of healthy controls (PinC samples), all patients exhibit a decrease in shape ratio, indicating a reduction in the number of pathological RBC shapes.

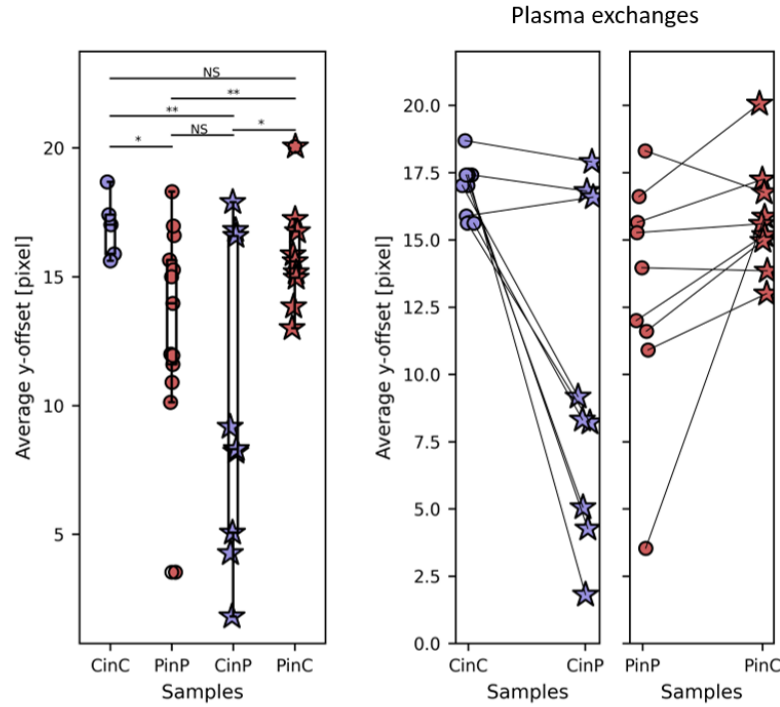


Fig. 3.21: The RBC center-of-mass shift regard to the middle of the channel, described as y-offset, in boxplot for all samples, followed by plasma exchanges with their correspondences for high velocities. \* refers to a significance level of  $0.005 < p < 0.08$ , \*\* to  $p < 0.025$ , and NS stands for not significant. Adapted from [12].

The pathologic fraction, defined as the ratio of pathological RBC shapes to all cells, confirms the finding. The CinC samples have a consistently low pathologic fraction, while the PinP samples consistently exhibit pathologic fractions greater than one.

There is a significant increase in the fraction of pathological RBC shapes in the samples CinP when compared to the original control condition (CinC). Conversely, the PinC samples show a decrease in the fraction of pathological shapes. Figure 3.21 displays the y-offset, a flow parameter that highlights this behavior, for both control and patient RBCs in both autologous and allogenic plasma.

The significant increased number of sphero-echinocytes in RBCs suspended in COVID-19 plasma significantly impacts the flow properties of the RBCs. These altered RBCs, with impaired deformability, result in the impairment of the emergence of stable slipper-shaped cells at high velocities. As a consequence, there is a noticeable deviation from the single-cell flow behavior observed in healthy cells. In healthy plasma, control RBCs exhibit an off-centered flow pattern, with an y-offset above zero. However, when these RBCs come into contact with COVID-19 plasma, their behavior changes significantly. They exhibit a distinct flow pattern with a smaller y-offset, indicating a more centralized flow compared to healthy RBCs in autologous plasma. And, although less pronounced, similar differences can still be observed when patient RBCs are suspended in healthy plasma. These distinct flow behaviors are become clear in the PDFs of the y-offset distributions when analyzing a set of CinC, CinP, PinP, and PinC combinations individually, as shown in Figure 3.22.

Quantifying the flow behavior disparity between pathological and healthy RBCs using the y-deviation parameter reveals a significant impediment for RBCs to adopt slipper-like shapes when exposed to COVID-19 patient plasma. The distinct shift in the PDF of the y-offset becomes apparent, with the prominent peak around 20 pixel for the samples CinC and around 15 for the sample PinC, indicating the deformation of RBCs at high velocities, being replaced by a smaller peak at the same position and the emergence of a second peak near zero when these RBCs are immersed in the plasma of COVID-19 patients.

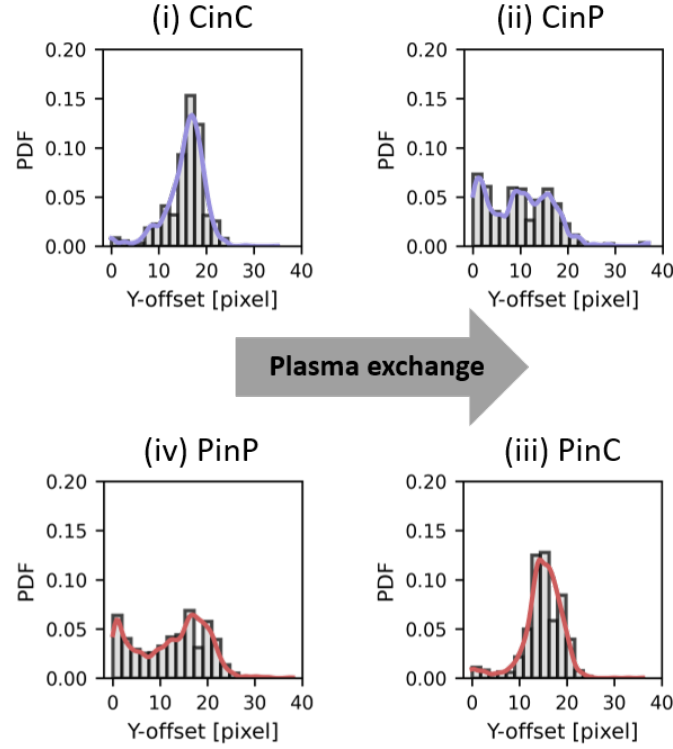


Fig. 3.22: Histograms and PDFs curves of the RBC y-offset absolute value at high velocities for a set of CinC, CinP, PinP and PinC exchanges. Adapted from [12].

### 3.2.3 Sick Cell Disease

In order to go deeper into the relationship between the ratio of HbS to normal hemoglobin increases and the disease severity, the study employed a predefined protocol to examine control and patient samples in both oxygenated and deoxygenated containing conditions. The samples were meticulously prepared following the study's protocols, which entailed creating 1 ml Tyrode solution supplemented with 0.1% BSA and containing 0.05% RBCs. Once prepared, the samples were incubated in a glove box under hypoxic conditions for 8 hours to induce the characteristic sickle-like appearance observed in SCD. And to maintain a controlled experimental environment, the entire procedure involving microcapillary flow was conducted inside the glove box. The phase diagrams obtained from one control and one patient in under normoxic and hypoxic conditions in show Figure 3.23.



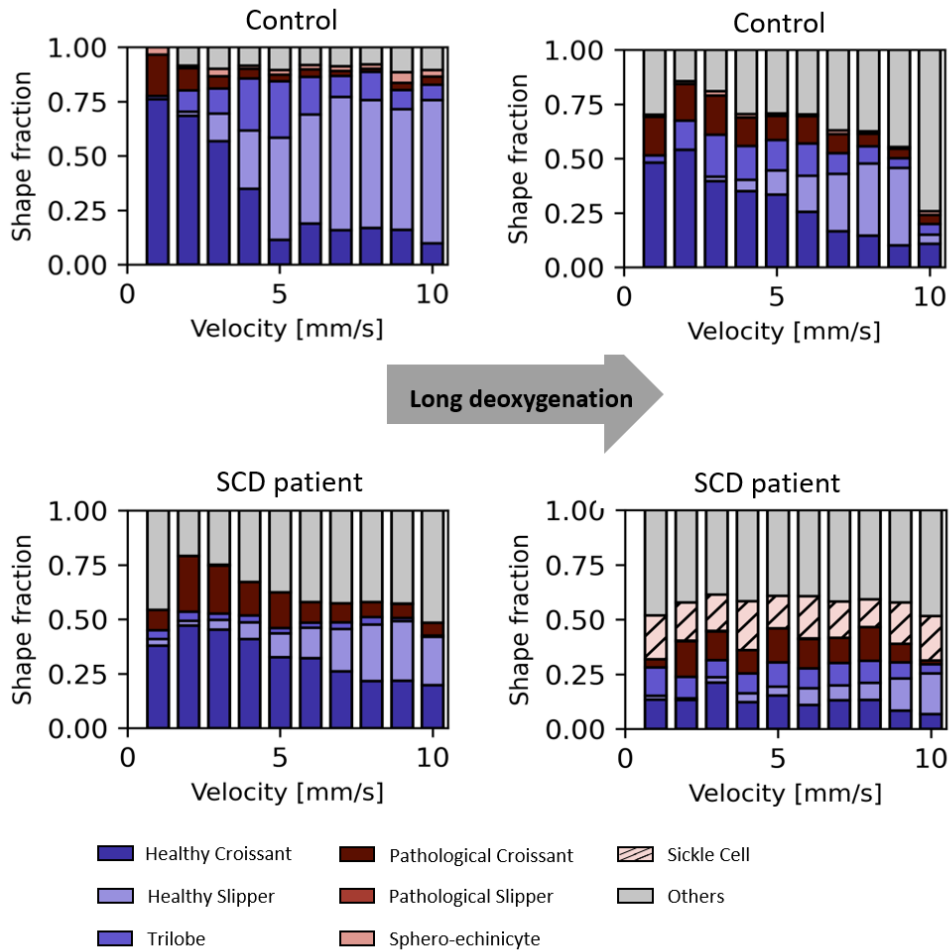


Fig. 3.23: Representative shape phase diagrams for one control and one SCD patient. The left panels depict the phase diagrams of the donors in oxygenated conditions, while the right panels illustrate the same donors after the long-deoxygenated condition.

In the presence of hypoxic conditions, the patient sample exhibits a significant presence of sickle cell shapes throughout the velocity range of 1 to 10 mm/s. Conversely, the control sample shows the absence of sickle cell shapes under the same hypoxic conditions. However, the flow behavior of the control sample does show some deviations from its normal state. Under normal oxygenation conditions, neither the controls nor the patients display the formation of sickle cells. However, there are observable differences between them. In the control sample under normal oxygen conditions, the expected behavior is observed, with healthy croissants and slippers appearing predominantly at low and high speeds, respectively. On the

other hand, the patient sample exhibits a relatively consistent presence of healthy croissants similar to the control sample, but a decrease in the occurrence of slippers at high speeds, accompanied by an increase in “others” shape. These observations are further elucidated in Figure 3.24.

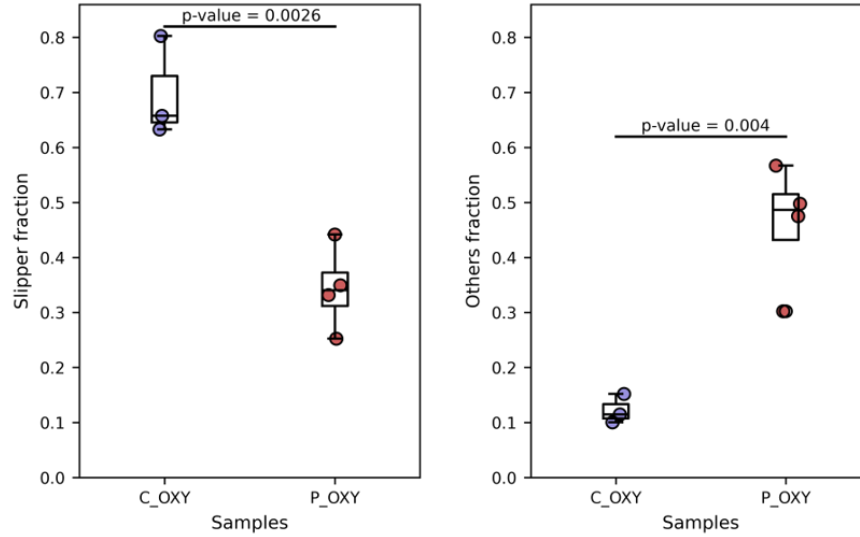


Fig. 3.24: Boxplot comparing the slipper and “other” fraction values at high velocities (8-10mm/s) between controls and patients under normal oxygenation conditions.

The slipper fraction, represented by the proportion of slipper-shaped RBCs over all RBC shapes at high velocities, exhibits the expected behavior in controls, with a higher concentration of slippers as the preferred shape at high velocities. However, in patients under oxygenated conditions, there is a significant decrease in the number of slipper-shaped RBCs compared to healthy individuals, indicating impaired deformability. Instead of the anticipated slippers, a notable percentage of RBCs assume an unidentified shape referred to as “others” at high velocities. This is quantified by the “others” fraction, which measures the ratio of “others” to the total number of all RBCs shapes at high velocities. Additionally, two other parameters, namely pathological fraction and % HbS, were employed to quantify the patient samples. Further details and visual representation of these measurements are in Figure 3.25 and in Figure 3.26.

While the relationship between the amount of RBCs that deform into slippers at high velocities, represented by the slipper fraction, and the presence of sickle hemoglobin (HbS) in SCD patients has not shown any clear link with the long deoxygenation process, as seen in 3.25, this changes when the pathological fraction is analyzed. The relationship between the pathological fraction of RBCs, deter-

mined by quantifying the abnormally shaped RBCs (including sickle cells) relative to the total number of RBCs, across a speed range of 1-10 mm/s, and the presence of HbS in SCD patients revealed a direct correlation between the amount of HbS in the patient's blood and the proportion of pathologically shaped RBCs under normal oxygen conditions. In other words, higher levels of HbS were associated with a greater fraction of abnormal RBC shapes, indicating an impaired ability of the RBCs to assume the healthy croissant shape and deform into slippers when subjected to flow.

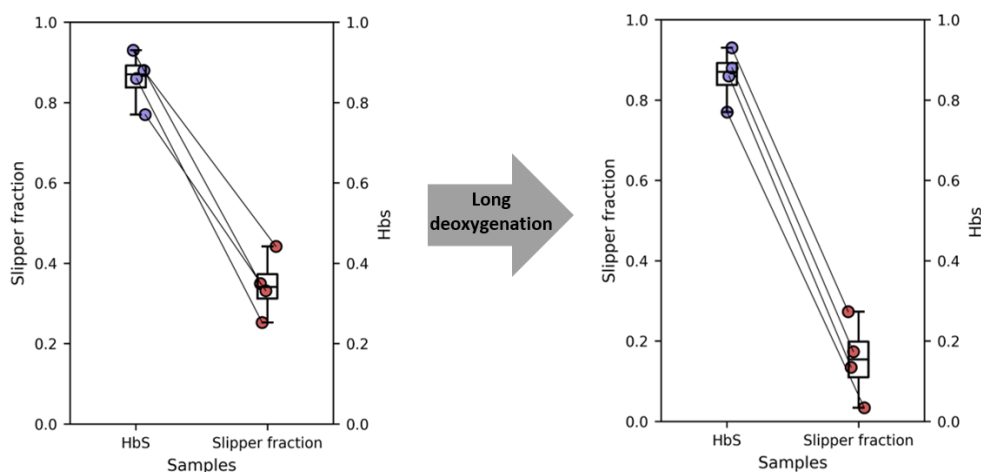


Fig. 3.25: Boxplot relating the HbS values of each patient and their slipper fraction, under both normal oxygenation and deoxygenation conditions for the range of high velocities.

Interestingly, the relationship between HbS levels and the pathological fraction was reversed when the samples were exposed to deoxygenation conditions for more than 8 hours. In this scenario, a higher HbS level in the patient's blood was associated with a lower fraction of pathological RBCs. This suggests that deoxygenation may influence the behavior of RBCs, leading to a reduced occurrence of abnormal shapes despite higher HbS levels. The relationship between the percentage of HbS and the occurrence of different sickle cell shapes is another aspect that warrants investigation. Figure 3.27 illustrates the presence of four distinct shapes of sickle cells identified during the analysis.

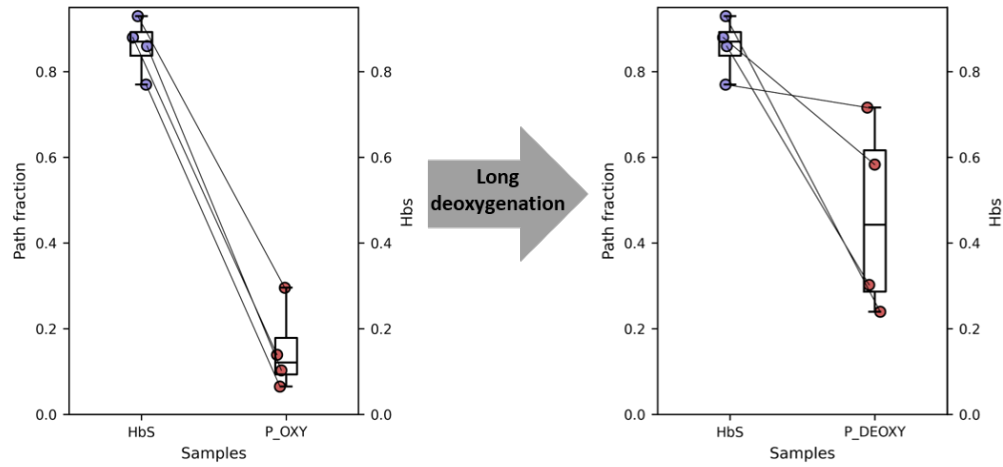


Fig. 3.26: Boxplot relating the HbS values of each patient and their fraction of pathological-shapes RBCs (including sickle cells), under both normal oxygenation and deoxygenation conditions for the whole range of velocities.

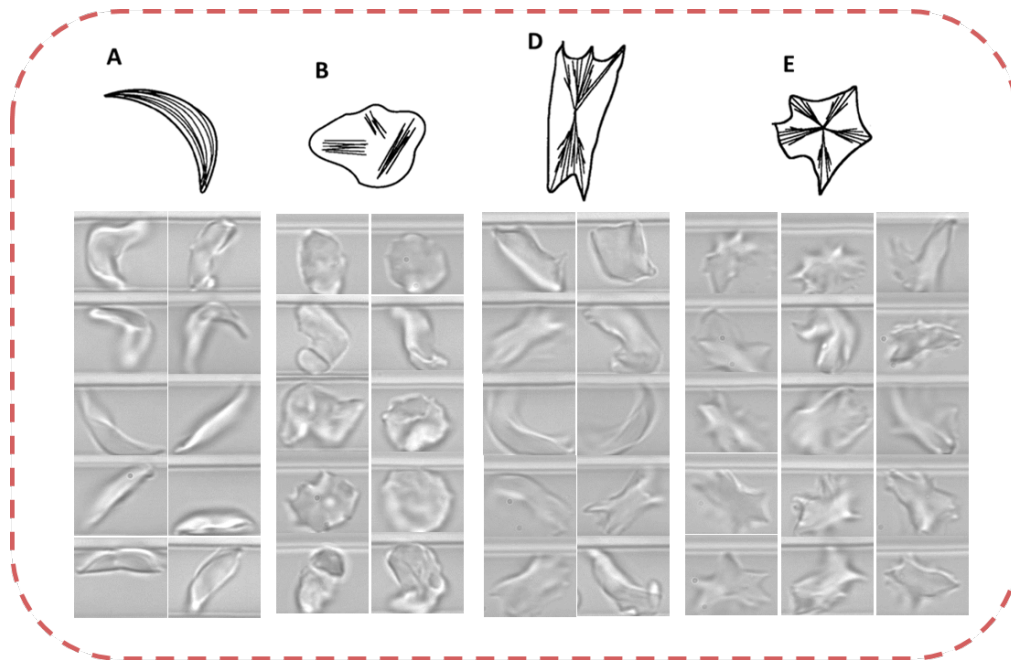


Fig. 3.27: Comparison between previously describe sickle cell shapes obtained from [45] and the images of sickle cells captured during the experiment across velocities ranging from 1-10mm/s. The observed shapes were categorized as follows: (A) single domain cell, (B) three domain cell, (D) central constriction cell, and (E) spherulite cell.

The analysis revealed the presence of four distinct shapes of sickle cells, namely the single domain cell (A), three domain cell (B), central constriction cell (D), and spherulite cell (E), in all patients analyzed across all the flow velocities (1-10mm/s). It is noteworthy that these shapes, although previously described in the literature under stasis conditions, exhibit different behaviors under hypoxic flow conditions. Specifically, they display variations in their flow characteristics, including y-offset, orientation, and positioning along the z-axis of the channel. In addition, the absence of the multiple domain sickle cell shape is noticeable.

### 3.2.4 Neuroacanthocytosis syndromes

Neuroacanthocytosis syndromes, characterized by the presence of acanthocytes, warrant investigation for the identification of acanthocytes beyond traditional blood smears, as they can be a potential biomarker for the characterization of the disease. In this study, nine carriers of neuroacanthocytosis syndromes, four with ChAc and another five with MLS, were included in the experimental testing using the proposed toolbox. The samples were prepared following the designated study protocol, resulting in a final sample volume of 1ml Tyrode solution with 0.1% BSA and 0.05% blood for each patient. The same procedure was carried out for a fresh control sample. The Figure 3.28 displays the phase diagram for all three cases.

Upon visual inspection, a notable observation is made when comparing NAS patients and controls. A higher number of pathologic RBC is observed, particularly at lower speeds. At higher velocities, both ChAc and MLS patients exhibit a lower occurrence of slippers. In the velocity range of 1 to 3 mm/s, the control group primarily consists of croissant-shaped cells, whereas the MLS patient displays a significant presence of acanthocytes and diseased croissants. The ChAc patients also show the occurrence of pathological shapes at low velocities, although in a smaller proportion. Despite the varying proportions, it is evident that the fraction of abnormal RBC in the patients is higher compared to the control group, which exhibits a near-zero fraction, as shown the shape ratio on Figure 3.29.

To emphasize the distinction between NAS patients and controls, the Shape ratio is plotted on a logarithmic scale. The statistical test enables the identification of significant differences. When comparing the differences between the control shape and ChAc SR, a p-value smaller than 0.02 is observed; between control and MLS, a p-value smaller 0.05 is identified, while the differences between ChAc and MLS demonstrate no statistically significant difference. Notably, both ChAc and MLS patients exhibit a higher proportion of pathological RBC across all the velocity range of 1-9 mm/s. Furthermore, healthy croissants and pathological croissants tend to flow closer to the center of the channel at lower velocities.

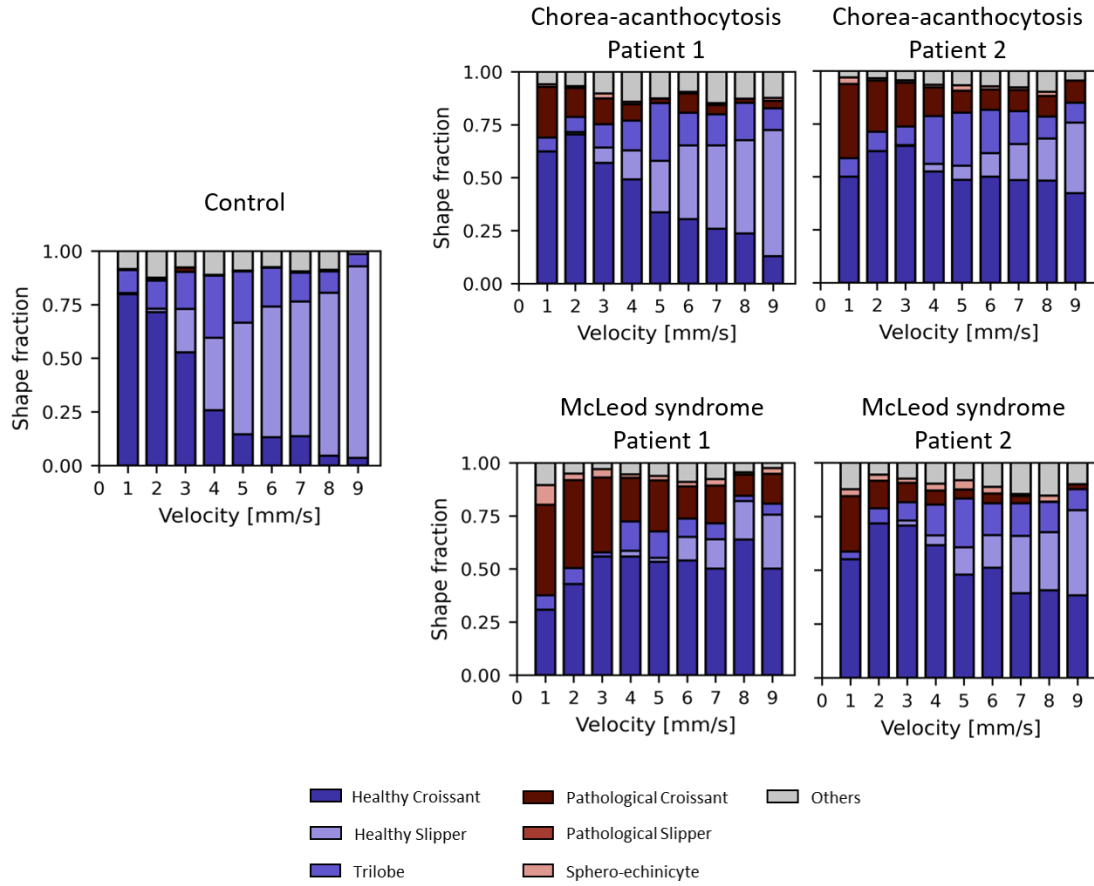


Fig. 3.28: Representative shape phase diagrams for two McLeod syndrome patients, two Chorea-acanthocytosis patients and one control. Adapted from [9]. See section Author's declaration of contributions, DECLARATION 2.

Acanthocytes, on the other hand, demonstrate a preference for central flow regardless of the velocity, resulting in varying impacts on the y-offset across different velocity ranges. As the acanthocytes, along with healthy and pathological croissants, tend to flow near the center of the canal, the y-offset average values of the MLS and ChAc patients closely resemble those of the controls. However, when examining higher velocities, the controls exhibit a higher mean y-offset compared to the patients. Figure 3.30 provides an illustration of the y-offset distributions for one MLS patient, one ChAc patient, and one control.

The y-offset distribution of the controls demonstrates a specific pattern. At low velocities, there is a concentration of healthy croissant-shaped cells flowing near the center of the channel, indicated by a y-offset close to zero. As the velocity increases, this concentration shifts towards higher values, causing the RBC to de-

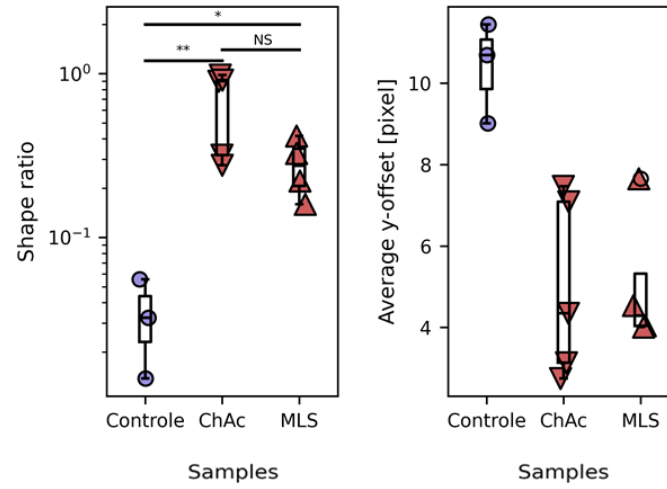


Fig. 3.29: The shape ratio is presented for the range of velocities from 1 to 9 mm/s, showcasing the data for five MLS patients, four ChAc patients, and three controls. Additionally, the average y-offset values are displayed for high-speed conditions (velocity above 6 mm/s) for the same samples. Highlighted in blue are also the RBC present in the controls for high and low velocities, as well as for the patients in red. Adapted from [9]. See section Author's declaration of contributions, DECLARATION 2.

form into slippers and flow away from the center, resulting in a y-offset greater than zero. Similar behavior is observed in ChAc and MLS patients at low velocities, as the acanthocytes and pathological croissants also preferentially flow in the center of the channel. However, a notable difference arises when comparing the y-offset distribution at high velocities. Instead of peaking at a value greater than zero, as seen in the controls, the patients' distribution shows the occurrence of pathological forms and acanthocytes even at high velocities, with the peak of the distribution remaining close to zero. This discrepancy highlights the presence of pathological croissants and acanthocytes persisting at higher velocities in the patients, contrasting with the shift towards slippers observed in the controls.

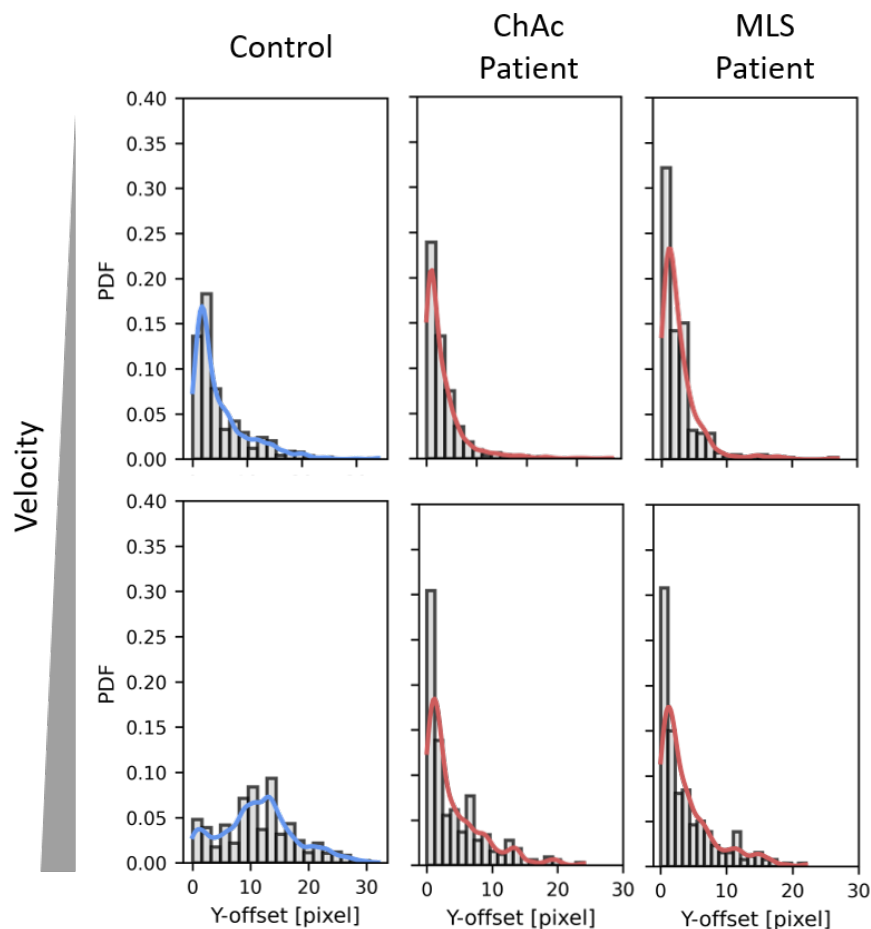


Fig. 3.30: The y-offset distribution at high and low velocities is compared for a control, a ChAc patient, and an MLS patient, emphasizing the contrasting behavior of the PDF curves at high velocity. Adapted from [9]. See section Author's declaration of contributions, DECLARATION 2.

### 3.2.5 Huntington's Disease

The diagnosis of Huntington's disease, a genetic neural disease, is a complex process that involves clinical evaluation, genetic testing, family history assessment, symptom analysis, and imaging. In this study, seven HD patients were analyzed using the proposed toolbox. The samples were prepared according to a designed protocol, resulting in a 1ml Tyrode, 0.1% BSA and 0.05% blood. Additionally, three fresh controls underwent the same procedure. Figure 3.31 illustrates the phase diagram generated by the toolbox for two distinct HD patients and one control.



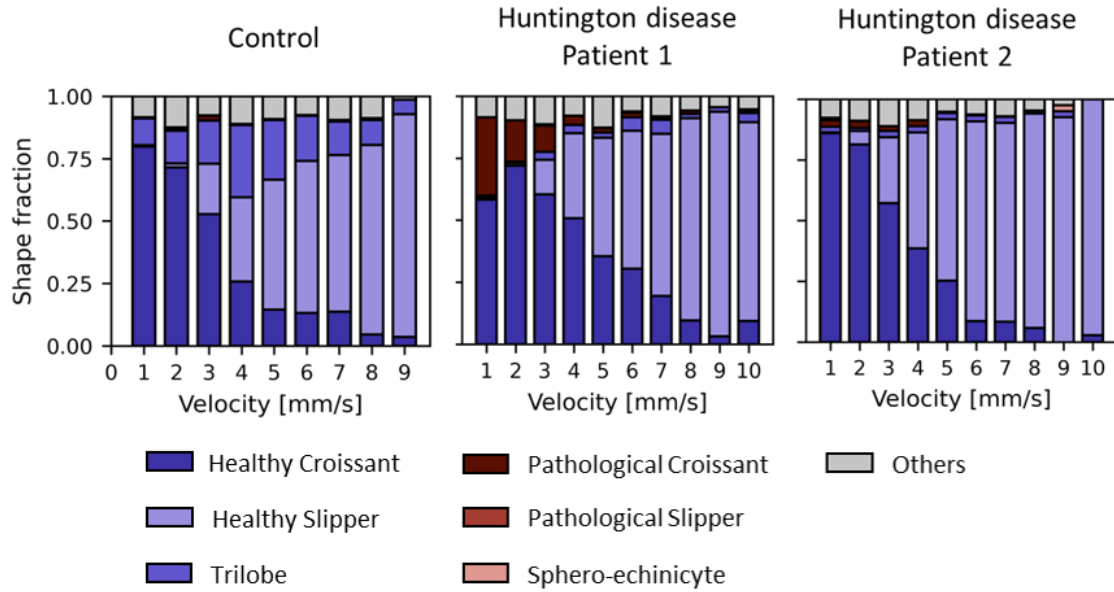


Fig. 3.31: Phase diagrams constructed to compare the RBCs behavior for one control and two HD patients, revealing a striking similarity in both cases. Adapted from [9]. See section Author's declaration of contributions, DECLARATION 2.

Both patient and control groups exhibit a high concentration of healthy croissants at low velocities, healthy slippers at high velocities, and a frequent transition between these two stable forms in the middle range of velocities (1-10 mm/s). However, a distinction between patients and controls arises at low velocities. Figure 3.32 provides insights into the shape ratio, y-offset, and mean projection area of RBCs for both controls and patients within the 1-3 mm/s velocity range.

At low velocities, the patients exhibit a slightly higher proportion of pathological RBCs compared to the controls, as indicated by the shape ratio. However, in accordance with the phase diagram, the pathological forms observed at low velocities do not exhibit any significant differences in their flow behavior. Both the shift of their center of mass, represented by the y-offset, and their projected area remain very close to the values of healthy RBCs within this range. Nonetheless, a minor distinction can be observed when examining the pathological forms of RBCs at low velocities in controls and HD patients, as depicted in Figure 3.33.

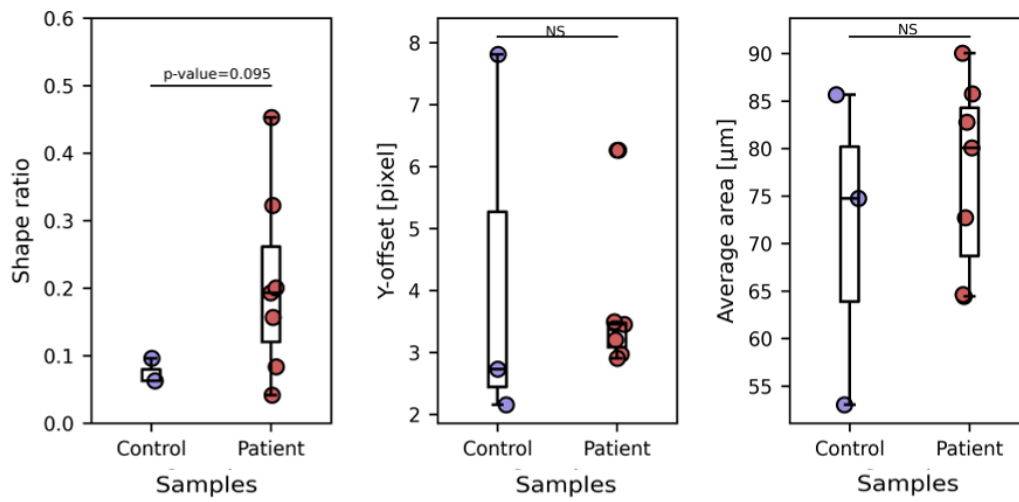


Fig. 3.32: The shape ratio, y-offset, and average projection area parameters assessed for three controls and seven HD patients in the velocity range of 1 to 3mm/s. NS stands for not significant. Adapted from [9]. See section Author's declaration of contributions, DECLARATION 2.

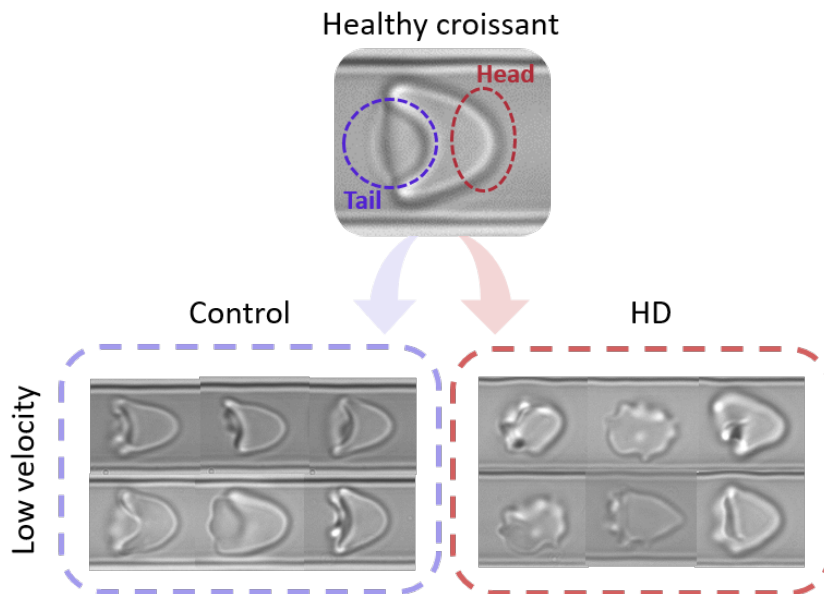


Fig. 3.33: A representation of a typical healthy croissant-shaped RBC, showcasing its intact head and tail. Subsequently, pathological croissant-shaped RBC images from both controls and HD patients, displaying visible membrane damage along their structure. Adapted from [9]. See section Author's declaration of contributions, DECLARATION 2.

The limited presence of pathological cells in the control samples is likely attributed to the storage and transportation time of the RBCs after collection from the donors. In these instances, the pathological RBC shapes observed during microfluidic flow are mainly croissant-shaped RBCs, which exhibit more pronounced membrane damage at the tail of the cell. In contrast, HD patients exhibit a distinct fraction of pathological RBCs. These pathological RBCs, bear resemblance to healthy croissants but feature "spicules" distributed across the entire membrane. This pattern is the same to what has been observed in NAS and is depicted in Figure 3.34.

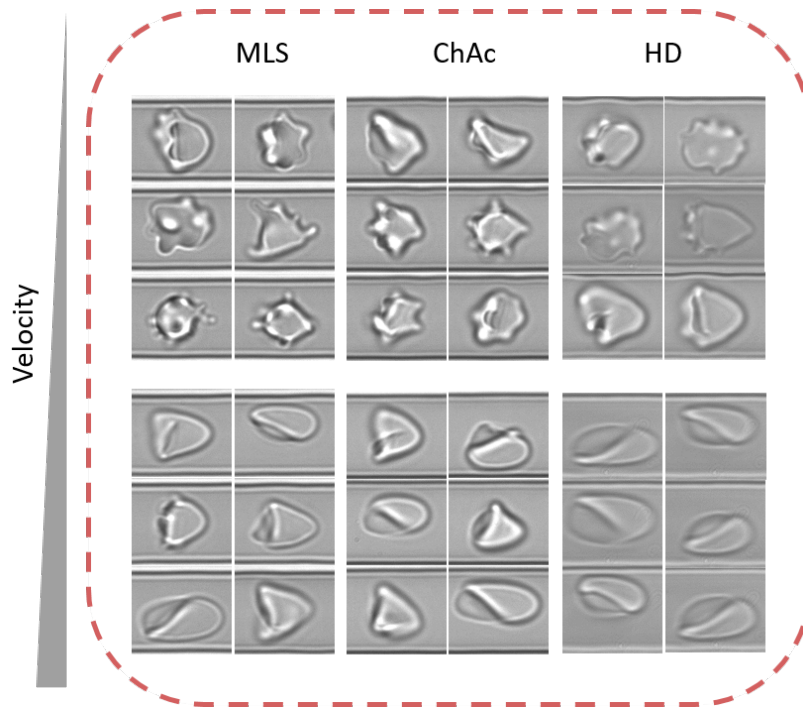


Fig. 3.34: Representation of pathological RBCs at high and low velocities. NAS patients have acanthocytes throughout this range, while HD patients have pathological RBCs, primarily at lower velocities, and a biggest number of slippers at higher velocities. Adapted from [9]. See section Author's declaration of contributions, DECLARATION 2.

Similar to MLS and ChAc patients, the HD patients also exhibit the presence pathological RBCs. However, there are some notable differences in the distribution of them. While in both NAS patients, acanthocytes are observed throughout the velocity range of 1-10 mm/s, as depicted in Figure 3.34, in HD patients, the pathological-shaped RBCs are predominantly found at lower velocities (1-3 mm/s), although in fewer quantities compared to NAS patients. And at higher velocities, the occurrence of pathological RBCs is absent in HD patients, distinguishing them from NAS patients. Additionally, the variation in the pathological fraction, as il-

illustrated in Figure 3.34, is corroborated by the values shown in Figure 3.35. This is evident at both low and high velocities, where it is shown that the proportion of the pathological fraction in HD patients is lower than in NAS patients.

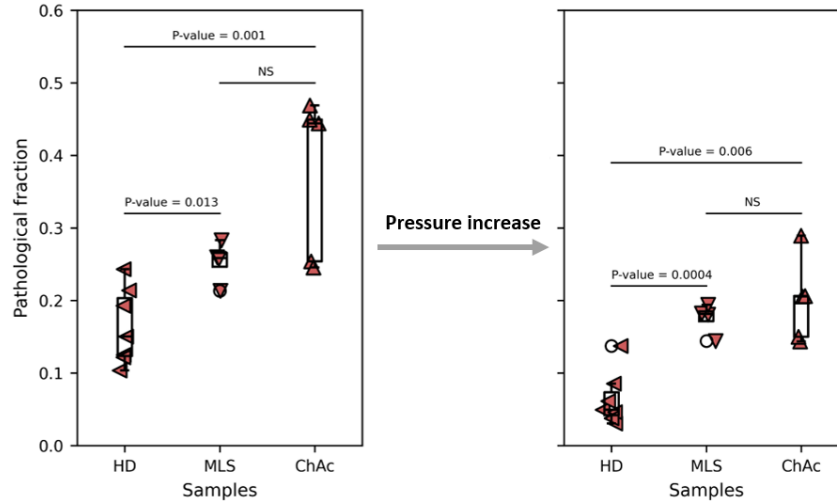


Fig. 3.35: The pathological fraction for seven HD patients, four MLS and five ChAc patients in both high (pressure > 400 mbar) and low (pressure < 400 mbar) velocities. NS stands for not significant.

### 3.2.6 Stored blood

The AI-based toolbox proposed in this study has a dual purpose, serving not only as a characterization tool for RBC diseases but also as a valuable resource for quality control of stored blood units. Its functionality is focused on identifying storage lesions that have the potential to damage the cell membrane of RBCs during the storage period. By the detection and analysis of these storage lesions, the toolbox enables early detection of potential issues and ensures the quality and integrity of stored blood units. To investigate this aspect, a total of six blood units were selected for experimental testing over a period of ten weeks. Each week, a small blood sample was extracted from the connecting tube of each blood unit, and then subjected to the established protocol as outlined in this study. To ensure a thorough and comprehensive analysis, ten samples were prepared and tested for each blood unit, corresponding to the different time points throughout the experiment. This process resulted in a total of sixty blood samples. All the samples were prepared using a solution of 1ml PBS + 0.1% BSA with a 0.05% blood aliquot. To visualize the impact of storage on RBC, the Figure 3.36 below shows the phase diagram for two of the blood units at three different time points throughout the experiment.

The selection of samples to represent the blood units was based on the work done by Recktenwald *et al.* [9] (see See section Author's declaration of contributions, DECLARATION 2.) and Lopes *et al.* [73].

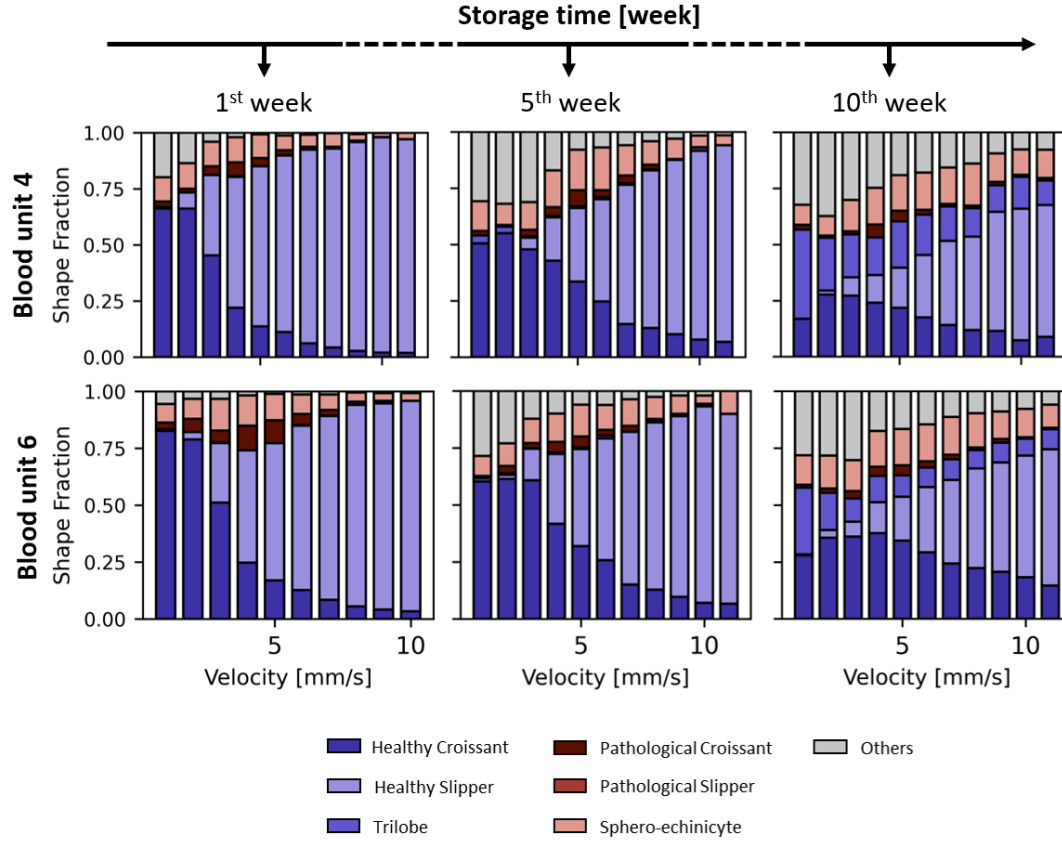


Fig. 3.36: Phase diagram for two units of blood at three different storage time points (one, five and 10 weeks), highlighting the increase in the occurrence of pathological shapes as the storage time increases. Adapted from [9]. See section Author's declaration of contributions, DECLARATION 2.

The first phase diagram represents the distribution of RBC shapes for blood unit after one week of storage. Similar to the phase diagram of a healthy individual, the majority of healthy croissants are concentrated at low velocities, while healthy slippers become more prominent as the velocity increases. Visually, the presence of pathological forms is minimal during this time. However, the second phase diagram, corresponding to the fifth week of storage for the same blood unit, reveals a noticeable shift in form distribution. The number of healthy slippers decreases, leading to an increased frequency of pathological forms throughout the distribution, particularly at higher velocities. Upon visual inspection of the third phase diagram,

corresponding to the tenth week of storage, significant changes in RBC shapes become apparent as the storage time progresses. The once abundant healthy, stable, off-centered shapes are significantly reduced, giving way to a prevalence of pathological shapes. Additionally, there is an increased frequency of pathological forms across all velocities in the diagram, indicating the impact of prolonged storage time on the morphological behavior of RBC. The changes in RBC shapes with increased storage time are also accompanied by notable alterations in the y offset distribution, as showed in Figure 3.37.

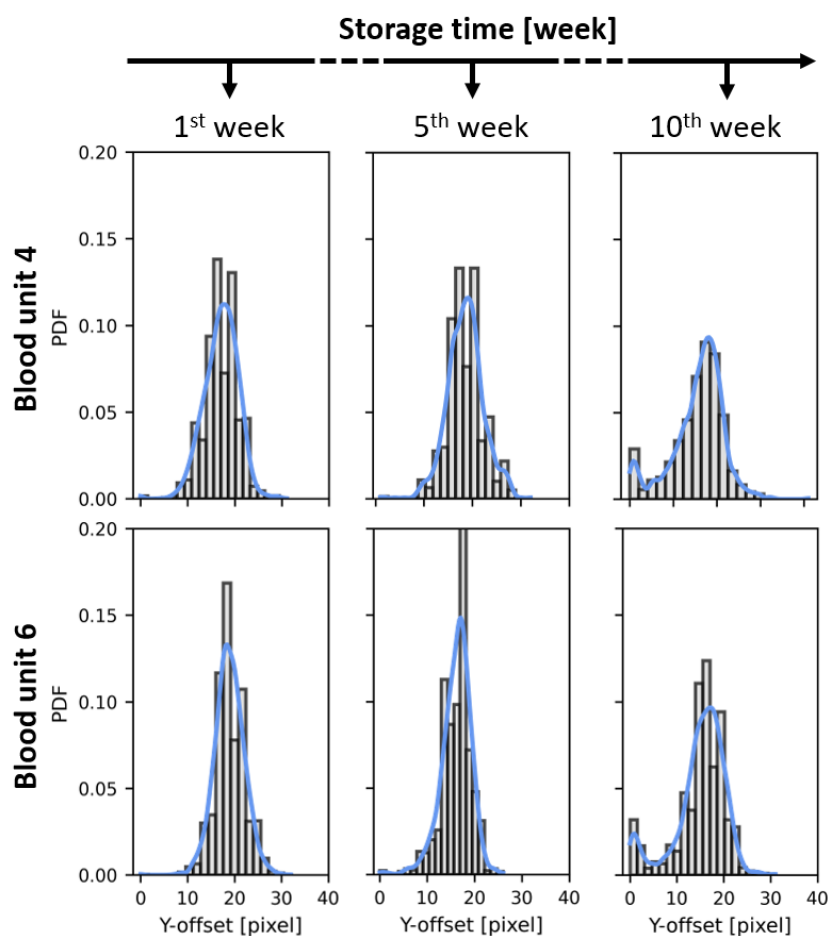


Fig. 3.37: PDF and histograms for the distribution of y-offset values for high-velocity RBC flow from two units at one, five and ten weeks of storage. Adapted from [9]. See section Author's declaration of contributions, DECLARATION 2.

Since the biggest the impact of RBC shape changes occurred in high velocities, the distribution of y-offset positions was specifically analyzed within the velocity

range of 8 to 10mm/s. In the first week of storage for both blood units 4 and 6 revealed that RBCs initially deformed into slipper shapes at these high velocities, as evident from the prominent off-center peaks observed in the PDFs. However, it is widely documented in the literature that RBC deformability decreases during the storage of blood units. This observation was consistent with the increasing peak in the distributions at  $|y\text{-offset}| = 0$  for both blood units as the storage time progressed. This suggests that an increasing number of cells were unable to deform to the stable slipper shapes and instead exhibited various other shapes that flowed closer to the middle of the microfluidic channel. It is also important to note that despite the simultaneous decrease in the frequency of slipper-shaped RBCs and the increase in more centralized shapes, the specific shapes observed differed between each blood unit, as the Figure 3.38 shows.

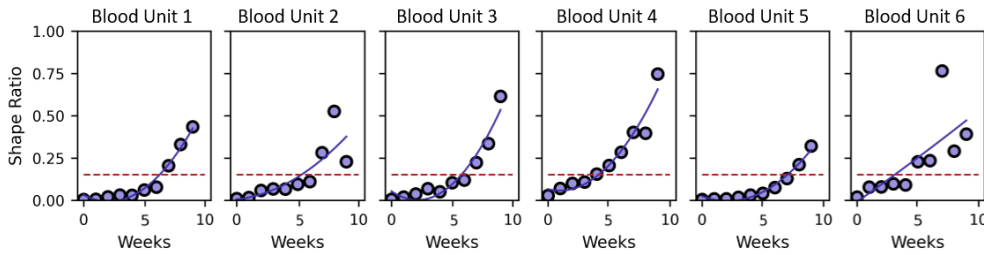


Fig. 3.38: Shape ratio for all donors as a function of time. The blue symbols correspond to the shape ratio and the blue lines represent polynomial fits. The red dotted line represents the average SR of healthy RBC units at 6 weeks (42 days) as reference. Adapted from [9]. See section Author's declaration of contributions, DECLARATION 2.

The shape ratio of RBC was employed as a parameter to assess the changes in flow behavior of RBCs during the 10-week storage period, and it was compared with the same parameter for a fresh control. Additionally, the average shape ratio of healthy RBC units at week 6 (42 days), which represents the storage threshold that conventional additive storage solutions support to store RBCs [114], was marked as a red dotted line as a reference. The shape ratio was plotted for each week of storage and adjusted polynomially over time for all blood units included in the experiment. Through visual examination of the results for all blood units, it is evident that they all eventually reached the reference threshold, although at different time points. While half of the samples (units 3, 4, and 6) exceeded the threshold between the fifth and sixth, units 1 and 2 only reached the same value in week 7, and unit 5 achieved the same point in the ninth week of storage. This observation underscores the heterogeneity and donor dependence of stored RBCs, indicating individual variations in their response to storage conditions.





## 4 Discussion

In recent years, single-cell assays have gained popularity in the field of human red blood cell research and diagnostics [68]. While traditional methods, such as live cell imaging, patch clamp, flow cytometry, and single-cell PCR, have proven valuable, they come with certain limitations. These include extensive and time-consuming pre-processing procedures and limited throughput when dealing with diverse RBC populations containing diseased cells. Moreover, analyzing RBC deformation presents another challenge. Deformability measurement techniques often require intricate experiments, typically manageable only by skilled personnel using specialized equipment. This complexity renders these techniques unsuitable for routine or point-of-care clinical analysis [57], as exemplified by the toolbox proposed in this work. In this context, microfluidic technologies are a promising solution to address the challenges associated with RBC deformability analysis. They offer a straightforward, fast, and cost-effective platform that emulates the properties of microvasculature, reflecting responses at cellular levels [57, 115].

The toolbox proposed in this study offers a rapid and unbiased assessment of RBC properties and shapes in capillary flow by combining microfluidic and machine learning technologies. Through the utilization of rectangular microfluidic channels with dimensions slightly larger than the RBC diameter, the simulation of capillary flow enables the evaluation of the flow characteristics of stable RBC shape configurations across a broad range of velocities. Consequently, the microscale flow behavior of the cells, with a specific focus on the position of the RBC center of mass relative to the channel width and the shape-ratio can be thoroughly examined as flow characteristic parameters for RBC.

Furthermore, the incorporation of machine learning algorithms enables the identification and characterization of pathological RBC morphologies under constant flow conditions. This capability facilitates the detection of morphological changes, serving as a distinctive parameter for specific diseases. And together with the y-offset and the shape ratio, the distribution of RBC shapes throughout the velocity spectrum, are proposed as potential biomarkers applicable to diverse medical and clinical applications.

Although incorporating machine learning algorithms significantly enhances the identification and characterization of pathological RBC morphologies under con-

stant flow conditions, there are several potential drawbacks and limitations to consider. One limitation is the dependence on high-quality data for training the algorithms; inaccuracies or biases in the dataset can lead to misclassifications. Additionally, the computational cost of implementing these machine learning models can be substantial, requiring significant time and processing power, which may not be feasible in all clinical settings. Finally, while the proposed biomarkers show promise, their validation and clinical acceptance necessitate extensive testing across diverse populations to ensure their reliability and efficacy in various medical conditions.

## 4.1 Impact of RBC Morphology on Microcapillary Flow during COVID-19

The COVID-19 data was analyzed using the toolbox to gain a better understanding of the roles played by RBCs in the disease. Previous research [25, 116] has found certain markers in the blood of COVID-19 patients that are related to inflammation and how severe the disease might be. They have also looked at the RBCs shapes to see if they are connected to COVID-19. One particular RBCs shape, called spherocytocytes, seems to be linked to the infection. These cells have a connection with some substances in the body that help to protect it from harmful substances called reactive oxygen species (ROS) and hydroperoxides, which can cause stress [12]. This suggests that the spherocytocytes-shaped RBCs might be helpful in detecting COVID-19 infection and how the body is responding to it, as in septic patients [117]. In response to bacterial infection, their immune system releases pro-inflammatory substances that not only fight the infection but also generate ROS to destroy bacteria. Spherocytocytes-shaped RBCs exhibit increased antioxidant activity, which serves as a protective response to counteract the elevated ROS levels induced by the infection [116, 117].

The analysis revealed that RBCs from healthy controls, don't show the echinocytes shapes (see Figure 3.19 ), but maintained their healthy shape when suspended in their own plasma. However, when these RBCs were exposed to allogenic plasma from COVID-19 patients, they exhibited a significant increase in pathological shapes, including spherocytocytes. Surprisingly, RBCs from COVID-19 patients were able to transform into croissant and slipper shapes during flow, resembling the single-cell flow behavior observed in healthy control RBCs suspended in autologous plasma (Figure 3.19). Although these findings contradict previous literature that suggested spherocytocytes cannot revert back to their healthy discocyte shape (in stasis) under normal conditions [112, 118], they align with Ponder E.'s results [119], which describe that spherocytes—the final stage of RBC transforma-

tion before hemolysis (cell destruction)—could revert to biconcave discs, provided they have not reached the stage of prolytic spheres (an advanced stage of degradation). Additionally, Roussel *et al.* have shown that morphological changes in red blood cells, such as membrane shedding and the acquisition of a spherocytosis phenotype, although apparently reversible, result in smaller red blood cells with reduced volumes [120]. These smaller cells are preferentially removed from the blood by the spleen (splenic sequestration [120]). These results indicate that red blood cells have a special ability to maintain a balanced environment in the blood, as they can adjust their metabolism and shape in response to changes in their surroundings [12]. The analysis of RBCs' proteins and metabolites aligns with the changes observed in the plasma of COVID-19 patients, confirming a close association between altered RBC morphology and markers of inflammation, oxidation, and oxygen deprivation in these patients [12]. This was demonstrated in the investigation of RBCs and plasma for the 50 primary metabolites and proteins, previously altered in COVID-19 samples, in the PinP, CinC, CinP, and PinC samples as shown in Figure 4.1A.

In the initial analysis of the impact of RBCs on plasma, higher levels of certain proteins like albumin and transferrin were observed in the CinC samples, which are associated with reduced coagulation and inflammation. Conversely, the PinP samples displayed elevated levels of proteins and metabolites linked to inflammation and coagulation in the plasma (such as C2, C3, C5, C7, C9, SERPINA1, SERPINA3, SERPINA G1 and C-reactive protein). Additionally, in the PinC samples, [68]the plasma content swiftly transformed to resemble that of individuals without COVID-19, while the opposite effect occurred in the CinP samples. These results (Figure 4.1B) highlight the considerable influence of red blood cells on plasma content and suggest a delicate equilibrium between red blood cells and plasma. This interplay between red cells and plasma may account for the morphological changes observed in healthy RBCs when exposed to COVID-19 plasma, where the influence of red cells on plasma content appears to affect red cell morphology, ultimately impacting the blood flow properties of the cells [10].

Furthermore, alterations in the concentrations of tryptophan-related metabolites in plasma were observed (Figure 4.1C). COVID-19 patients exhibited elevated levels of a metabolite known as kynurenine, a factor associated with an increased risk of mortality [10]. Intriguingly, when COVID-19 patients' RBCs were introduced into healthy plasma, kynurenine levels increased, while the opposite effect occurred when healthy individuals' red cells were exposed to the patients' plasma. This implies that red blood cells might have a role in modulating the levels of kynurenine and related metabolites, potentially influencing the risk of mortality in COVID-19 patients (Figure 4.1D).

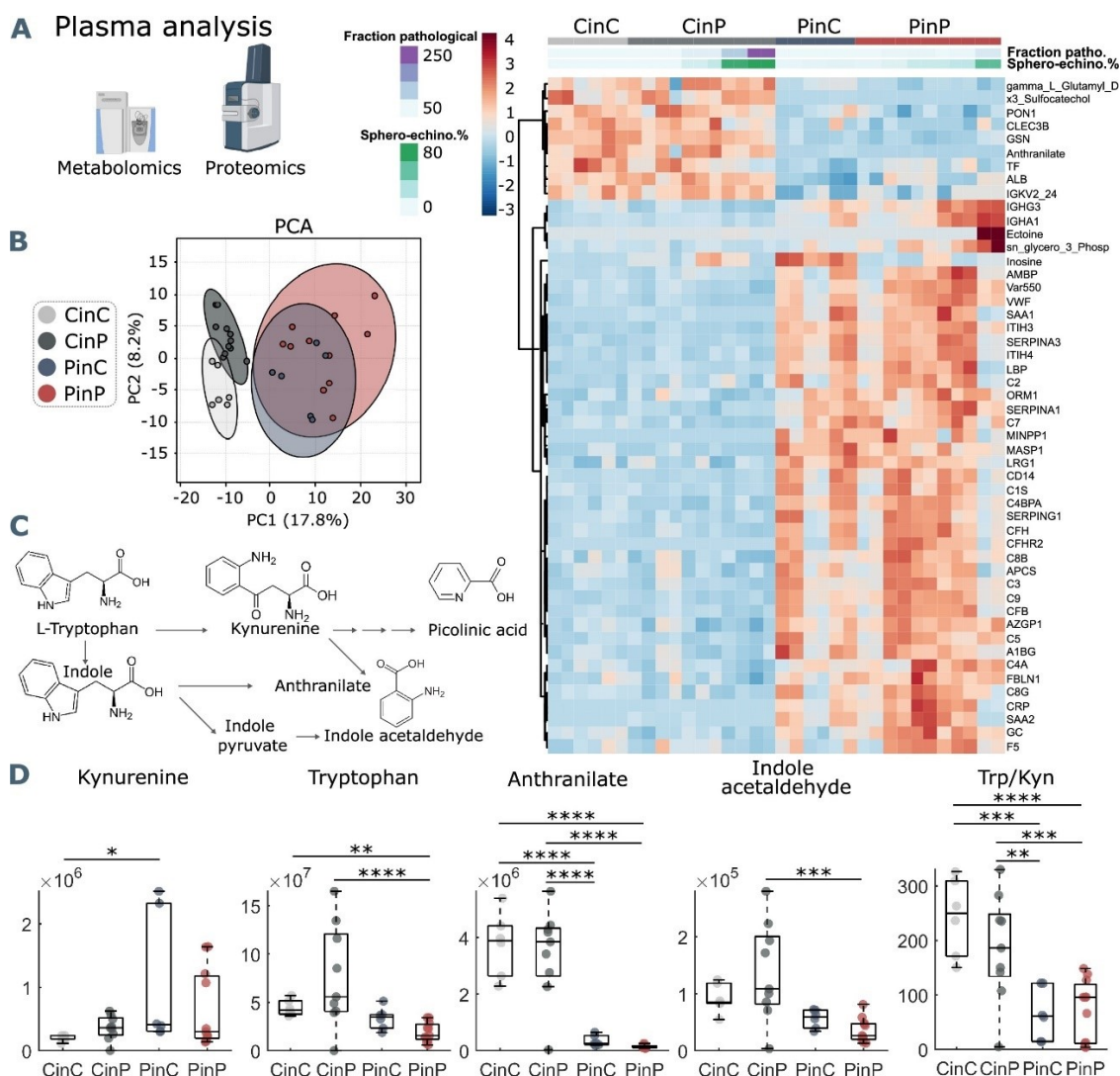


Fig. 4.1: Taken from [12]. (A) Hierarchical clustering analysis was performed on the most significantly altered top 50 metabolites and proteins using a two-way ANOVA test. (B) Principal component analysis (PCA) carries out on the metabolomics and proteomics plasma data revealing distinctive groupings and variations among the samples. (C) The tryptophan pathway's conversion to kynurenine, anthranilate, and indole acetaldehyde. (D) The boxplots present peak areas for selected analytes determined by UHPLC-MS.

Despite differences in plasma components like albumin, fibrinogen, gelsolin, transferrin, serpins, and immunoglobulins between healthy RBC samples (CinC) and RBC samples from COVID-19 patients (PinP) [10], certain similarities exist in

these substances within the RBCs (Figure 4.2A). Moreover, RBCs from healthy individuals exhibit unique behavior when in their own plasma (CinC), characterized by elevated levels of pantothenol, adenosine, and hydroxyglutarate, known for their antiseptic properties. This hints at a protective effect of RBCs when in their autologous plasma. Conversely, RBCs in PinP samples from patients are rich in proteins linked to cellular stress responses, including ubiquitination and proteasome-mediated protein degradation, suggesting higher oxidative stress. There are also signs of increased arginine breakdown in these RBCs.

This highlights the significant influence of RBCs on the protein and chemical composition of plasma [10]. When RBCs are placed in allogeneic plasma (CinP and PinC), the plasma's protein and chemical profile adapts to resemble what's expected with the respective RBC type. This shift results in altered protein and immunoglobulin levels that align with their associated RBC groups (CinC and PinP). It demonstrates the RBCs' fast capability to fine-tune their protein levels when interacting with new plasma (Figure 4.2B). Interestingly, these shifts in RBC metabolism and protein content don't correspond with changes in RBC morphology, as PinP samples exhibit more pathological RBC shapes compared to PinC samples.

The RBC shapes have correlations with various plasma components, particularly with the sphero-echinocytes (Figure 4.2C). For instance, substances linked to increased glycolysis (like lactate and 2,3-diphosphoglycerate (2,3-DPG)), a process that becomes more active when RBCs take on a sphero-echinocyte shape, are correlated. Additionally, compounds related to tryptophan metabolism (nicotinamide and tryptophanamide) show connections with the presence of spheroechinocyte-shaped RBCs. Furthermore, certain components such as glutamate, creatine, and hypoxanthine, along with lactoferrin (LTF), ectoine, and 2-oxoglutarate ( $\alpha$ -ketoglutarate), are also associated with the occurrence of spheroechinocyte shapes in RBCs.

Furthermore, changes in the shape of red blood cells are also related to specific substances found within the red blood cells themselves (Figure 4.2D). It's observed that variations in RBC shapes are associated with various factors: (i) RBC deformability seems to be negatively correlated with lactate and mannitol levels, suggesting that reduced levels of mannitol may be linked to decreased RBC flexibility, possibly indicating health issues, (ii) proteins like albumin (ALB) and transferrin (TF) play a role in affecting RBC shapes, (iii) decreased TF levels are associated with inflammatory markers such as C-reactive protein (CRP) and interleukin-6 (IL-6), (iv) there's a correlation between lower levels of tryptophan and related metabolites within RBCs and altered RBC shapes, and (v) Certain amino acids and catabolic products, especially those related to arginine, are positively correlated with pathological RBC shapes.

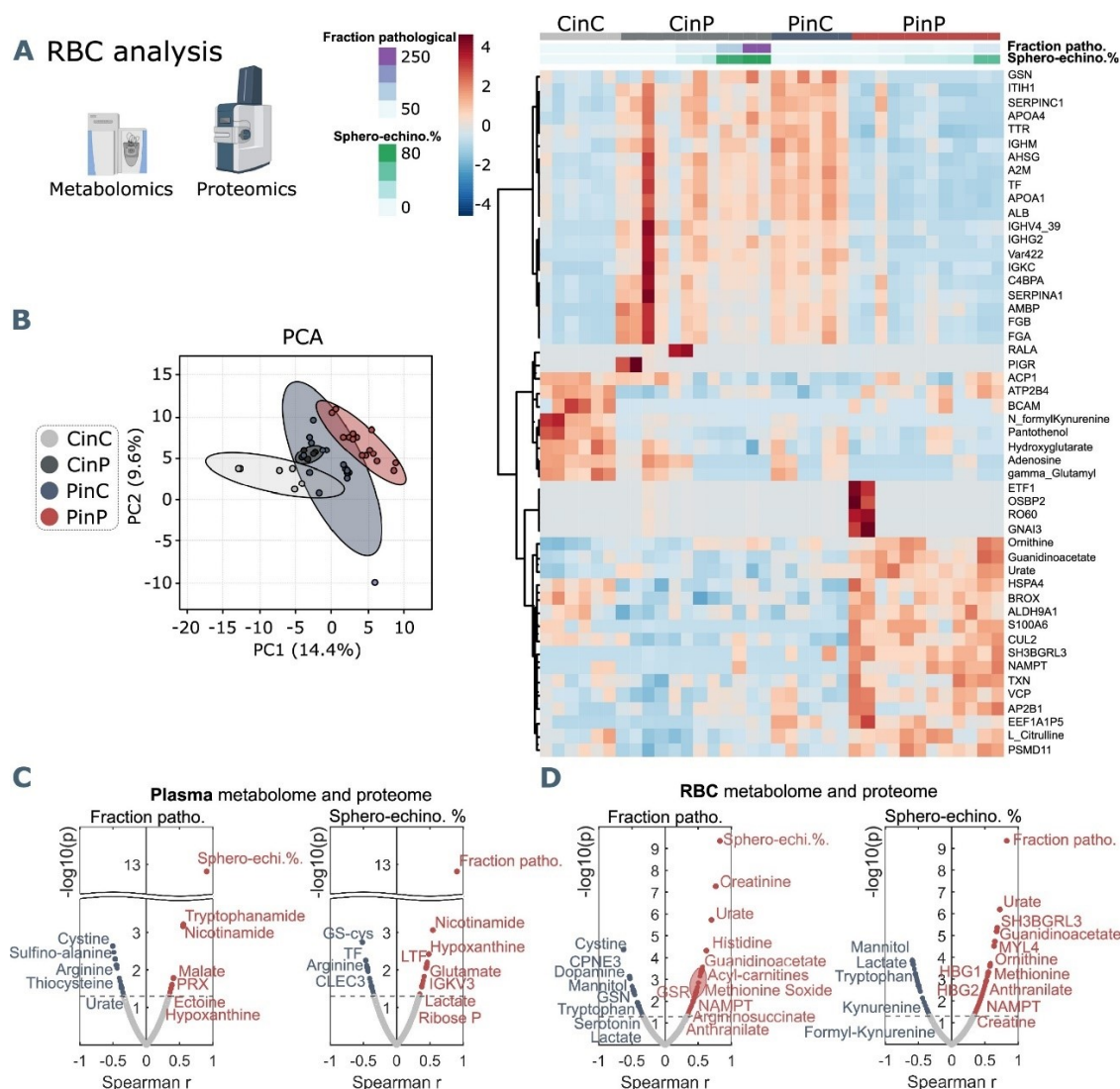


Fig. 4.2: Taken from [10]. (A) Hierarchical clustering analysis of the top 50 metabolites and proteins in RBCs by two-way ANOVA test that exhibited the most pronounced changes. (B) PCA analysis performed on the metabolomics and proteomics from RBC content. Plasma and RBC Spearman correlation analysis of RBC shape parameters with omics data. (C) Volcano plot representations highlight the most significant proteins and metabolites in plasma. (D) Volcano plot representations highlight the most significant proteins and metabolites in RBCs.

All these findings may have implications for the clinical use of convalescent plasma transfusion in COVID-19 patients. Although this treatment approach has not shown significant clinical benefits so far, there is potential for improvement by

transfusing plasma from healthy individuals to COVID-19 patients. This transfusion may have positive effects on the RBCs flow properties and potentially reduce the risk of blood clot formation, which is commonly associated with abnormal RBCs in COVID-19 [10]. However, it is important to carefully consider the potential drawbacks of plasma transfusion. One significant concern is the dilution of the patient's antibodies in the transfused plasma. This dilution could potentially compromise the effectiveness of the patient's immune response against the virus, as antibodies play a crucial role in neutralizing the virus and aiding in recovery. To fully understand the benefits and limitations of plasma transfusion in COVID-19 treatment, further studies are necessary. These studies should focus on elucidating the underlying mechanisms by which RBCs contribute to restoring plasma balance and how this restoration impacts patient outcomes. It is essential to investigate the potential benefits of plasma transfusion in enhancing RBC flow properties and reducing the risk of complications, while also addressing the potential limitations associated with antibody dilution.

## 4.2 Insights into RBC Behavior in Sickle Cell Disease

The study utilized a toolbox to assess the severity of SCD by analyzing data from SCD samples in flow in both deoxygenated and oxygenated conditions. The results revealed distinct differences in the behavior of RBCs between patients and controls, not only under hypoxic conditions where sickle cells were observed. The analyses indicate that the parameters derived from flow parameters have the potential to serve as biomarkers for assessing disease severity, even under normal oxygen conditions. This is significant as the lack of consensus on specific criteria and parameters for defining disease severity poses a major challenge in managing SCD [121, 122].

In the context of normal oxygen conditions, a parameter called "the slipper fraction" was introduced as a potential biomarker for assessing the deformability of RBCs in SCD. The analysis revealed notable differences in the ability of SCD patient RBCs to deform into slippers at high speeds compared to control RBCs, suggesting a reduced proportion of deformable RBCs in patients. This parameter offers the advantage of eliminating the requirement for deoxygenation during analysis. Moreover, the presence of sickle hemoglobin (HbS), a distinctive feature of SCD, was found to be associated with another parameter called the pathological fraction. Surprisingly, the relationship between HbS levels and the pathological fraction exhibited an inverse proportionality under normal and hypoxic conditions, contrary to initial expectations. While the quantity of abnormal RBCs appears to have a directly proportional influence on HbS levels under normal oxygen conditions, this dependence becomes inversely proportional in hypoxia.

In the context of hypoxia, the formation of sickle cells, resulting from the crystallization of HbS, in microcirculation has been extensively documented in the scientific literature [123–125]. These sickle cells exhibit various deformation shapes, as described in [53]. During flow analysis, sickle cells were observed across the entire range of velocities to which the RBCs were subjected, displaying four out of the five reported sickle shapes. The absence of the multiple domain cell form can be attributed to the likelihood that its polymerized HbS fibers may not possess enough properties to flow and subsequently are susceptible to breakage under the force of the flow. However, the other four shapes of sickle cells (single domain cell, three domain cell, central constriction cell, and spherulite cell) were not only observed in abundance but also demonstrated significant diversity within the same classification. These sickle cells displayed varying flow properties (see Figure 3.27), flowing both near the center and in proximity to the channel walls. Moreover, they exhibited orientations in the same direction as well as opposite to the flow. This information, when combined with other clinical parameters, has the potential to serve as a biomarker for assessing disease severity.

Microfluidic methodologies have played a vital role in SCD investigations and are recognized as significant contributors in the identification of novel disease biomarkers, as highlighted by Horton [123]. Microfluidic devices can replicate hypoxic conditions and diverse blood flow to mirror in vivo characteristics like oxygen levels, and mechanical rigidity. Aich *et al.* [56] note vaso-occlusive events can be a key indicator of clinical implications in SCD, potentially serving as a disease severity biomarker. While deformation quantification via dynamic deformability index is possible, this method has limitations in tissue geometry and single cell analysis. Lab-on-chip platforms, as the one proposed here, are capable of simulating various body microenvironments, present promising biomarkers, fostering a more comprehensive understanding of SCD mechanisms and treatment effects. Tools like the proposed platform can offer a way to assess drug safety, toxicity, and effectiveness, contributing to a more personalized medical approach for SCD patients. Moreover, it can provide insights into how irregular sickle cell flow behavior can impact specific organs, guiding the development of combination therapies to enhance treatment outcomes.

These findings provide valuable insights into the relationship between the RBC flow parameters and the SCD. However, it is important to note that this information alone is insufficient. SCD is a highly heterogeneous condition that manifests differently among individuals, and its progression can vary across populations and ethnic groups. Further research is necessary to unravel the underlying mechanisms and implications of these observations, which could potentially contribute to the development of targeted interventions for the management of SCD.



### 4.3 Biomechanical RBC properties in Neuroacanthocytosis syndrome compared to Huntington's disease

The utilization of the proposed toolbox extends to the examination of microcapillary RBC flow as a novel characterization approach for neuroacanthocytosis syndrome (NAS) and Huntington's disease (HD). In NAS patients, distinct RBC properties are observed compared to healthy controls, as depicted in the Figure 3.33. Nevertheless, identifying acanthocytes in NAS patients has posed significant challenges, often leading to delays in diagnosis. The primary approach relies on the identification of gene mutations through genetic testing, or alternatively, it can be performed using conventional characterization methods like wet unfixed blood smears. However, these traditional methods are not universally accessible [38] and can also be prone to errors. Regarding HD, the quest for novel biomarkers has gained increased urgency [126], primarily due to the challenges associated with its diagnosis, which currently relies on brain scan images and cerebrospinal fluid analysis. But, unlike NAS, HD does not typically exhibit a prominent presence of acanthocytes as a diagnostic hallmark. However, recent research indicates that abnormal RBC can also be identified in HD patients [48]. This raises important questions: can the presence of pathological RBC shapes, similar to NAS, serve as a biomarker for HD characterization? Additionally, how can NAS be distinguished from HD when both conditions exhibit the presence of such abnormal cells?

To address these inquiries, proposal to leverage the mechanical characteristics of RBCs during circulation as a biomarker for both diseases was done. This aims to enhance diagnostic accessibility, enable comprehensive disease monitoring, and thereby provide a means to gain deeper insights into their progression and potential therapeutic avenues.

In NAS patients, the presence of acanthocytes was observed in the capillary flow velocity range of 1-9 mm/s, whereas normocytes were found in healthy control subjects, as illustrated in Figure 3.31. However, as the flow intensity increased, a clear distinction between healthy and pathological RBCs became apparent, as indicated by the y-offset parameter depicted in Figure 3.32. At higher velocities, the distribution of flow positions, evaluated through the offset, showed distinct patterns between controls and NAS patients.

Conversely, in the case of HD, the behavior of pathological cells differed. At high velocities, the percentage of abnormal cells was minimal compared to NAS patients and closely resembled the shape distribution of healthy controls. However, a notable difference emerged within the low-speed range of 1-3 mm/s, where a higher

accumulation of pathological cells was observed in HD patients, as demonstrated by the shape-ratio in Figure 3.32. Similar to NAS, the analysis of flow biomarkers posed challenges due to the overlapping characteristics between pathological and healthy RBC shapes at low velocities [9] ( See section Author’s declaration of contributions, DECLARATION 2.), as indicated by the y-offset and mean projection area parameters. Thus, relying on the presence of acanthocytes remained crucial. Notably, a careful examination of the percentage of pathological cells at low velocities revealed a substantial presence of pathological shapes in HD samples, distinguishing them from controls but resembling the findings in NAS patients.

Given that NAS and HD result in substantial yet systematic and reproducible alterations in RBC morphology during capillary flow, it was demonstrated that the observed morphological characteristics in the capillary flow of RBCs can be a functional biomarker for identifying both diseases. In light of this fact, the discussion done by Walker [45], exploring the intricate aspects of clinical trials aimed at slowing down the progression of HD, is reconsidered. They underscore the impediments faced in such studies, primarily due to funding constraints and the lack of a clearly defined and practical evaluation marker. This discussion prompts the proposal highlighted here that the analysis of RBCs morphology in flow, augmented by AI, could be valuable markers not only for HD disease but also for NAS within the context of clinical trials. According to Walker, ongoing observational studies of individuals at risk are exploring the possibility of using the onset of HD clinical symptoms or other disease biomarkers, such as alterations in imaging tests, as potential trial endpoints. However, these imaging tests, although functional, suffer from being both time-consuming and costly, rendering them less than ideal for addressing this issue. To overcome these limitations, the RBC shape assessment method proposed herein provides a quicker and more robust means of evaluating RBC flow properties and pathological shapes. This solution stands as a promising path for clinical trials, not only to monitor the effects of drugs on patients but also to track the progression of the disease itself.

In summary, the potential of acanthocytes in microcapillary flow as a biomarker for NAS is still under investigation, and its diagnostic significance in HD needs further exploration. Differentiating between NAS and HD relies on the distribution and accumulation patterns of abnormal cells at specific velocity ranges. NAS patients exhibit a wider range of acanthocytes across velocities, while HD patients demonstrate a concentrated presence of the pathological shapes primarily at low velocities. Additional research and studies involving a larger number of patients, including differential diagnosis of other neurological disorders, and evaluating the specificity of the method are necessary to validate these findings. These efforts are crucial before RBC capillary flow can be considered a functional characterization tool or a reliable biomarker for interventional studies in these diseases. And Con-

sidering the lack of effective treatments for halting or reversing HD and NAS [126], the search for new biomarkers capable of monitoring disease progression holds significant promise for identifying targets for intervention and therapy. By identifying specific biomarkers, it becomes possible to develop strategies that can better track the course of these diseases and facilitate the development of interventions aimed at improving patient outcomes

## 4.4 Assessing RBC Shapes in Microfluidic Flow for Stored Blood

The Toolbox was employed to evaluate the changes induced by the storage through the analysis of individual cell flow. Across the entire range of velocities, the presence of pathological RBC shapes resulting from storage lesions was successfully detected using the Toolbox, as depicted in Figure 3.36 through phase diagrams that highlighted pathological RBC shapes. However, the parameter of biggest relevance for this scenario was examined at high speeds due to the RBC impaired deformability. Figure 3.37 illustrated that the cells were unable to deform into the characteristic slipper shape, which could lead to their recognition as "dysfunctional" by the human body and subsequent removal. After transfusion, a significant proportion of transfused RBCs, up to 30%, are cleared from the bloodstream within 24 hours [9,127] ( See section Author's declaration of contributions, DECLARATION 2.). Nevertheless, the precise mechanisms underlying this elimination process and the subsequent rejuvenation of the remaining RBCs in circulation, leading to the restoration of their original functions, are still not fully understood [9,73,128] ( See section Author's declaration of contributions, DECLARATION 2.). Additionally, there is often a lack of information regarding the survival duration of transfused RBCs within the body. Consequently, utilizing the y-offset as a parameter to assess functional and high-quality RBCs could aid in making informed decisions regarding the volume and frequency of transfusions for each patient. This approach could minimize the risks associated with transfusion-related complications [73].

The RBCs functionality can be significantly influenced by various factors such as donor eligibility, health status, storage time, and transportation. However, beyond these factors, the optimal compatibility between a blood unit and its recipient could be an important consideration. Parameters such as age and sex [73,129,130] have been investigated to assess their impact on reducing the risks associated with transfusion procedures. The findings, presented in Figure 3.38, demonstrate a notable variation in RBC properties over time among different donors. This information, combined with additional donor data, could be utilized to assess the compatibility and identify the ideal match for transfusion purposes. By incorporating a compre-

hensive understanding of RBC properties and considering donor-specific factors, it becomes possible to optimize the selection of compatible blood units for transfusion, ensuring enhanced patient outcomes. An exemplary illustration of this concept is found in [131], where the discussion centers on the utilization of lab-on-a-chip technology and machine learning, such as the toolbox proposed here, to enhance the assessment of RBC quality and refine transfusion medicine [132]. The primary focus of Isiksacan *et. al* involve elucidating how these innovative technologies, when harmonized with approaches like metabolomics, laboratory analyses, and recipient data, can generate a comprehensive 'vein-to-vein' database tailored for precision transfusion medicine. In this scenario, when combining lab-on-a-chip technology with artificial intelligence, an extensive understanding of RBC properties and donor-related factors is achieved, facilitating the evaluation of freshness, quality, and transfusion efficiency. Ultimately, the integration of these technologies into transfusion medicine endeavors can significantly improve patient outcomes by enhancing the selection of compatible blood units and elevating the overall quality assurance of stored RBCs [131].

Furthermore, the assessment of donor dependency in blood units can be extended to address the challenge of increased storage time. By evaluating whether certain blood units maintain the required quality and functionality parameters even after the legally mandated storage period of six weeks, this approach presents a potential solution to the current issue of blood shortages. Currently, all these matters are addressed by the EU Regulation on Blood, Tissues and Cells (BTC legislation) [65, 133], which establishes guidelines ensuring the safety and quality of blood products. However, this legislation, existing for nearly two decades, no longer adequately meets the evolving demands in the field [134]. The need for an update is driven by advancements in science and technology, emerging diseases, and global commercialization. Systems for handling human-origin substances operate at a national level, posing challenges for cross-border exchange and access to related therapies. In July 2022, the European Commission proposed a revision and extension of the BTC regulations to simplify and standardize these practices. The Commission suggests replacing the current directives with a single regulation to be uniformly applied across all Member States. This aims to establish consistent protection levels across the EU, facilitating access to these substances across borders. This proposal aligns with the challenges faced in the quality and safety of blood substances like the RBC units used in transfusions. It seeks to set high standards ensuring the health protection of donors and recipients. Innovations like combining microfluidic technologies with artificial intelligence for analyzing and categorizing blood cells in microcapillary flow represent significant advancements, enabling swift and objective evaluations of stored blood cell quality. Moreover, this evaluation enables the identification of blood units that remain viable beyond the standard storage duration, effectively optimizing the utilization of available resources and

contributing to the mitigation of blood scarcity.

By conducting further clinical studies using the toolbox, it is possible to not only extend the understanding of stored RBC quality and donor dependency but also provide prospective predictions regarding the behavior of specific RBCs in vivo. This could potentially enhance the management of RBC transfusions and contribute to advancements in the field of erythrocyte management [9,73] ( See section Author's declaration of contributions, DECLARATION 2.).



## 5 Conclusion and outlook

In conclusion, this research has developed a comprehensive toolbox based on artificial intelligence for characterization blood diseases. Chapter 1 introduces the state of the art in studying single RBC deformability as a biomarker, detailing instances where RBC deformity occurs (such as in certain pathologies and stored blood units) and the application of artificial intelligence in analyzing single RBC samples in flow. The following chapter explains the methodology and materials used in constructing the microfluidic chips, preparing samples under both oxygenated and hypoxic conditions, and developing the toolbox for tracking and cropping flowing single RBCs. Chapter 3 encompasses two pivotal research streams: the methodological development for classifying the shapes of flowing single RBCs and the biological investigation of these methods applied to blood samples from healthy individuals, patients with diseases that cause RBC deformation, and stored blood units.

During the methodological development, four different artificial intelligence-based techniques were devised to classify the RBC shapes of healthy individuals in *in vitro* experiments, based on their membrane deformations induced by microfluidic flow. The first technique proposed the use of single RBC images obtained through optical and spatial modulation of RBCs to implement an ANN. This ANN served as the decoder to reconstruct the cell image based on modulation, thereby classifying them as slippers or croissants. Although this method showed advancements in the modulation stage by reducing reliance on sophisticated optics, there was still room for improvement in the AI component. This led to the development of the second classification technique, which transitioned from the mask approach to a real encoder, transforming the system into an autoencoder. The use of a VAE approach aimed to address challenges in the modulation process by improving encoding and generating better decoded images, resulting in a well-defined latent space with stable RBC shapes in its corners. While stable RBC shapes were successfully positioned in certain quadrants of the latent space, the transition shapes between slippers and croissants did not align with those observed in *in vitro* experiments or described in literature, prompting the exploration of alternative classification solutions. The third technique considered the inclusion of damaged RBC samples during classification, leading to the implementation of a four-stage CNN-Tree model. However, due to significant confusion between healthy and pathological RBC classes, the Tree-CNN approach did not yield satisfactory results, necessitating the development of a

more robust methodology. Finally, the fourth technique, transfer learning, was implemented. RBCs were classified by fine-tuning a pre-trained object tracking model called YOLO. This approach improved performance by reducing misclassification between healthy and pathological RBC shapes, greatly enhancing the accuracy and efficiency of the classification process. This successful system was integrated into the toolbox, allowing the evaluation of hydrodynamically induced shapes of tracked and cropped RBCs. A phase diagram was constructed to illustrate the distribution of these shapes as a function of their velocity, facilitating the calculation of flow parameters to statistically characterize the flow behavior of individual RBCs.

The second part of this chapter delves into a biological investigation, presenting the phase diagram data and establishing the following flow parameters:

- Area of the 2D projection of the RBC, relative to the XY axes.
- Y-offset, defined as the position of the RBC center of mass relative to the channel width.
- Shape ratio, the proportion of pathophysiological RBC shapes relative to healthy ones.
- Pathological fraction, quantifying the abnormally shaped RBCs (including sickle cells) relative to the total number of RBCs.
- Slipper fraction, the proportion of slipper-shaped RBCs over all RBC shapes.
- Others fraction, the proportion of RBC shapes not classified in the literature over all RBC shapes.

The study statistically characterized these parameters using the ANOVA test to establish the reference behavior of healthy RBC shapes in flow, serving as a benchmark for comparison. The same parameters were then calculated for patients under different conditions, including those with blood diseases such as SCD, as well as diseases where RBCs play a significant role in disease progression and act as markers, such as COVID-19, NAS, and HD. Additionally, these parameters were extended to assess the quality and functionality of blood units for transfusion purposes.

The fourth and final chapter of this research provides valuable insights into the behavior of RBCs in microfluidic channels, focusing on RBC morphology in micro-capillary flow. The main findings and implications of this study can be summarized as follows:

- Insights into RBC behavior during COVID-19: The study found that RBCs from healthy controls maintained their typical when suspended in their own plasma. However, when these RBCs were exposed to plasma from COVID-19 patients, they exhibited a significant increase in pathological shapes, includ-



ing spherocytocytes, which are indicative of infection. Conversely, RBCs from COVID-19 patients demonstrated the ability to transform into croissant and slipper shapes during microfluidic flow, mirroring the single-cell flow behavior observed in healthy control RBCs suspended in autologous plasma. This suggests that the pathological changes in RBC morphology are influenced by the plasma environment and can revert to more normal shapes under specific conditions.

- Insights into RBC behavior in SCD: When examining RBCs from sickle cell anemia (SCD) patients under varying oxygen conditions, it was noted that these cells exhibited decreased deformability into slippers at high speeds compared to control RBCs. This suggests a lower proportion of deformable RBCs in SCD patients. Furthermore, the presence of HbS was associated with the pathological fraction, indicating an inverse relationship between HbS levels and the pathological fraction when comparing hypoxic and normal conditions.
- Insights into RBC behavior in NAS compared to HD: The study presented the microfluidic approach as an alternative to identifying acanthocytes in NAS patients and suggested a potential novel biomarker for HD by identifying distinct altered shapes of RBCs in patient samples. Beyond merely distinguishing between the pathological shapes associated with the two diseases, the research also revealed variations in the distribution of them. While acanthocytes in NAS predominantly appeared at high speeds, HD exhibited a significant accumulation of pathological RBCs at low speeds, highlighting unique characteristics of RBC behavior in each condition.
- Insights into RBC behavior in stored blood: The study observed a notable phenomenon: as the storage duration of RBCs increased, changes induced by the storage process led to a decrease in the deformation capacity of these cells. Specifically, there was a reduction in the quantity of slippers and an increase of spherocytocyte shape observed in units stored for extended periods. This finding underscores the impact of storage duration on the mechanical properties and deformability of RBCs, highlighting a potential limitation or consideration in the context of blood storage practices.

The findings from this study lay the groundwork for potential clinical implications, including the introduction of flow-based biomarkers for diagnosing and prognosticating the analyzed diseases. Moreover, it is conjectured that various other conditions, such as diabetes, rheumatism, diverse RBC disorders, and inflammation-related diseases like sepsis, may also demonstrate subtle yet systematic and reproducible alterations in RBC morphology during capillary flow. This suggests a wide array of potential applications for this technology as a diagnostic and monitoring system.

## 5.1 Future prospects

During this research, we identified an intriguing new path building on our current findings. Our study highlighted the link between the shapes of single RBCs in flow and various blood conditions. To further explore and validate these insights, we plan to investigate the role of artificial intelligence in characterizing these cells. In this next phase, we will expand the range of blood conditions studied and explore AI methods that can not only characterize RBCs in pathological shapes but also diagnose the underlying diseases.

AI offers new diagnostic possibilities based solely on the morphological information of single flowing RBCs by minimizing classification errors and eliminating subjective human input. Automating this process enables quick and robust assessments of flow properties and the quantity of pathological RBC shapes, opening new perspectives for monitoring and diagnosing blood conditions.

# Bibliography

- [1] OpenAI, “Chatgpt,” 2025. <https://chat.openai.com>.
- [2] D. GmbH, “DeepL translator,” 2025. <https://www.deepl.com/translator>.
- [3] T. W. Secomb, “Blood flow in the microcirculation,” *Annu. Rev. Fluid Mech.*, vol. 49, pp. 443–461, Jan. 2017.
- [4] S. M. Recktenwald, K. Graessel, F. M. Maurer, T. John, S. Gekle, and C. Wagner, “Red blood cell shape transitions and dynamics in time-dependent capillary flows,” *Biophys. J.*, vol. 121, pp. 23–36, Jan. 2022.
- [5] S. Guido and G. Tomaiuolo, “Microconfined flow behavior of red blood cells in vitro,” *Comptes Rendus Phys.*, vol. 10, pp. 751–763, Nov. 2009.
- [6] A. Guckenberger, A. Kihm, T. John, C. Wagner, and S. Gekle, “Numerical–experimental observation of shape bistability of red blood cells flowing in a microchannel,” *Soft Matter*, vol. 14, no. 11, pp. 2032–2043, 2018.
- [7] B. Kaoui, G. Biros, and C. Misbah, “Why do red blood cells have asymmetric shapes even in a symmetric flow?,” *Phys. Rev. Lett.*, vol. 103, p. 188101, Oct. 2009.
- [8] A. Saadat and et al., “A system for the high-throughput measurement of the shear modulus distribution of human red blood cells,” *Lab. Chip*, vol. 20, no. 16, pp. 2927–2936, 2020.
- [9] S. M. Recktenwald and et al., “Erysense, a lab-on-a-chip-based point-of-care device to evaluate red blood cell flow properties with multiple clinical applications,” *Front. Physiol.*, vol. 13, p. 884690, Apr. 2022.
- [10] U. A. Gurkan, “Biophysical and rheological biomarkers of red blood cell physiology and pathophysiology,” *Curr. Opin. Hematol.*, vol. 28, pp. 138–149, May 2021.
- [11] G. Tomaiuolo, “Biomechanical properties of red blood cells in health and disease towards microfluidics,” *Biomicrofluidics*, vol. 8, p. 051501, Sept. 2014.
- [12] S. M. Recktenwald and et al., “Cross-talk between red blood cells and plasma

- influences blood flow and omics phenotypes in severe covid-19,” *eLife*, vol. 11, p. e81316, Dec. 2022.
- [13] M. Depond, B. Henry, P. Buffet, and P. A. Ndour, “Methods to investigate the deformability of rbc during malaria,” *Front. Physiol.*, vol. 10, p. 1613, Jan. 2020.
- [14] M. Zhang, X. Li, M. Xu, and Q. Li, “Automated semantic segmentation of red blood cells for sickle cell disease,” *IEEE J. Biomed. Health Inform.*, vol. 24, pp. 3095–3102, Nov. 2020.
- [15] A. V. Buys, M.-J. Van Rooy, P. Soma, D. Van Papendorp, B. Lipinski, and E. Pretorius, “Changes in red blood cell membrane structure in type 2 diabetes: A scanning electron and atomic force microscopy study,” *Cardiovasc. Diabetol.*, vol. 12, p. 25, Dec. 2013.
- [16] L. Da Costa, J. Galimand, O. Fenneteau, and N. Mohandas, “Hereditary spherocytosis, elliptocytosis, and other red cell membrane disorders,” *Blood Rev.*, vol. 27, pp. 167–178, July 2013.
- [17] A. Vayá and et al., “Red blood cell distribution width and erythrocyte deformability in patients with acute myocardial infarction,” *Clin. Hemorheol. Microcirc.*, vol. 59, no. 2, pp. 107–114, 2015.
- [18] G. Simionato and et al., “Red blood cell phenotyping from 3d confocal images using artificial neural networks,” *PLOS Comput. Biol.*, vol. 17, p. e1008934, May 2021.
- [19] S. Quint and et al., “3d tomography of cells in micro-channels,” *Appl. Phys. Lett.*, vol. 111, p. 103701, Sept. 2017.
- [20] X. Ma and et al., “Extracorporeal membrane oxygenation (ecmo) in critically ill patients with coronavirus disease 2019 (covid-19) pneumonia and acute respiratory distress syndrome (ards),” *Med. Sci. Monit.*, vol. 26, Aug. 2020.
- [21] E. R. Mann and et al., “Longitudinal immune profiling reveals distinct features of covid-19 pathogenesis,” *Infectious Diseases (except HIV/AIDS)*, June 2020. preprint.
- [22] World Health Organization, “Coronavirus disease (covid-19) - World Health Organization (WHO),” 2023.
- [23] A. Izcovich and et al., “Prognostic factors for severity and mortality in patients infected with covid-19: A systematic review,” *PLOS ONE*, vol. 15, p. e0241955, Nov. 2020.

- [24] M. Palladino, "Complete blood count alterations in covid-19 patients: A narrative review," *Biochem. Medica*, vol. 31, pp. 403–415, Oct. 2021.
- [25] T. Thomas and et al., "Covid-19 infection alters kynurenine and fatty acid metabolism, correlating with il-6 levels and renal status," *JCI Insight*, vol. 5, pp. e140327, 140327, July 2020.
- [26] P. E. Taneri and et al., "Anemia and iron metabolism in covid-19: a systematic review and meta-analysis," *Eur. J. Epidemiol.*, vol. 35, pp. 763–773, Aug. 2020.
- [27] F. Zhou and et al., "Clinical course and risk factors for mortality of adult inpatients with covid-19 in wuhan, china: a retrospective cohort study," *The Lancet*, vol. 395, pp. 1054–1062, Mar. 2020.
- [28] X. Li and et al., "Risk factors for severity and mortality in adult covid-19 inpatients in wuhan," *J. Allergy Clin. Immunol.*, vol. 146, pp. 110–118, July 2020.
- [29] A. Majeed and M. A. Shajar, "Is hemoglobin the missing link in the pathogenesis of covid-19?," *Anaesth. Pain Intensive Care*, vol. 24, pp. 9–12, May 2020.
- [30] G. Ponti, M. Maccaferri, C. Ruini, A. Tomasi, and T. Ozben, "Biomarkers associated with covid-19 disease progression," *Crit. Rev. Clin. Lab. Sci.*, vol. 57, pp. 389–399, Aug. 2020.
- [31] M. Kubánková and et al., "Physical phenotype of blood cells is altered in covid-19," *Biophys. J.*, vol. 120, pp. 2838–2847, July 2021.
- [32] L. De Franceschi, G. J. C. G. M. Bosman, and N. Mohandas, "Abnormal red cell features associated with hereditary neurodegenerative disorders: The neuroacanthocytosis syndromes," *Curr. Opin. Hematol.*, vol. 21, pp. 201–209, May 2014.
- [33] A. Danek and R. H. Walker, "Neuroacanthocytosis," *Curr. Opin. Neurol.*, vol. 18, pp. 386–392, Aug. 2005.
- [34] L. Rampoldi, A. Danek, and A. P. Monaco, "Clinical features and molecular bases of neuroacanthocytosis," *J. Mol. Med.*, vol. 80, pp. 475–491, Aug. 2002.
- [35] H. H. Jung, A. Danek, and R. H. Walker, "Neuroacanthocytosis syndromes," *Orphanet J. Rare Dis.*, vol. 6, no. 1, p. 68, 2011.
- [36] L. Rampoldi and et al., "A conserved sorting-associated protein is mutant in chorea-acanthocytosis," *Nat. Genet.*, vol. 28, pp. 119–120, June 2001.

- [37] R. H. Walker, H. H. Jung, F. Tison, S. Lee, and A. Danek, “Phenotypic variation among brothers with the mcleod neuroacanthocytosis syndrome,” *Mov. Disord.*, vol. 22, pp. 244–247, Jan. 2007.
- [38] A. Storch, M. Kornhass, and J. Schwarz, “Testing for acanthocytosis: A prospective reader-blinded study in movement disorder patients,” *J. Neurol.*, vol. 252, pp. 84–90, Jan. 2005.
- [39] F. Reichel and et al., “Changes in blood cell deformability in chorea-acanthocytosis and effects of treatment with dasatinib or lithium,” *Front. Physiol.*, vol. 13, p. 852946, Apr. 2022.
- [40] A. Rabe and et al., “The erythrocyte sedimentation rate and its relation to cell shape and rigidity of red blood cells from chorea-acanthocytosis patients in an off-label treatment with dasatinib,” *Biomolecules*, vol. 11, p. 727, May 2021.
- [41] M. J. W. Adjobo-Hermans, J. C. A. Cluitmans, and G. J. C. G. M. Bosman, “Neuroacanthocytosis: Observations, theories and perspectives on the origin and significance of acanthocytes,” *Tremor Hyperkinetic Mov.*, vol. 5, p. 328, Aug. 2015.
- [42] European Medicines Agency, “Orphan designation: Eu/3/19/2149,” 2019.
- [43] O. C. Murphy, O. O’Toole, C. K. Hand, and A. M. Ryan, “Chorea-acanthocytosis and the huntington disease allele in an irish family,” *Tremor Hyperkinetic Mov.*, vol. 8, p. 604, Oct. 2018.
- [44] M. M. Gold, K. Shifteh, J. A. Bello, M. Lipton, D. M. Kaufman, and A. D. Brown, “Chorea-acanthocytosis: A mimicker of huntington disease case report and review of the literature,” *The Neurologist*, vol. 12, pp. 327–329, November 2006.
- [45] F. O. Walker, “Huntington’s disease,” *The Lancet*, vol. 369, pp. 218–228, Jan. 2007.
- [46] Y. Yu and et al., “Acanthocytes identified in huntington’s disease,” *Front. Neurosci.*, vol. 16, p. 913401, June 2022.
- [47] D. G. Anderson and et al., “Absence of acanthocytosis in huntington’s disease-like 2: A prospective comparison with huntington’s disease,” *Tremor Hyperkinetic Mov.*, vol. 7, p. 512, Dec. 2017.
- [48] K. Peikert and et al., “Commentary: Acanthocytes identified in huntington’s disease,” *Front. Neurosci.*, vol. 16, p. 1049676, Nov. 2022.

- [49] L. Palmer and et al., "Icsh recommendations for the standardization of nomenclature and grading of peripheral blood cell morphological features," *Int. J. Lab. Hematol.*, vol. 37, pp. 287–303, June 2015.
- [50] L. A. Kamentsky, "Cytology automation," in *Advances in Biological and Medical Physics*, vol. 14, pp. 93–161, Elsevier, 1973.
- [51] M. Podlacha, K. Pierzynowska, L. Gaffke, G. Jerzemowska, E. Piotrowska, and G. Wegrzyn, "Behavioral- and blood-based biomarkers for huntington's disease: Studies on the r6/1 mouse model with prospects for early diagnosis and monitoring of the disease," *Brain Behav. Immun. - Health*, vol. 23, p. 100482, Aug. 2022.
- [52] G. A. Barabino, M. O. Platt, and D. K. Kaul, "Sickle cell biomechanics," *Annu. Rev. Biomed. Eng.*, vol. 12, pp. 345–367, July 2010.
- [53] J. D. Corbett, W. E. Mickols, and M. F. Maestre, "Effect of hemoglobin concentration on nucleation and polymer formation in sickle red blood cells," *J. Biol. Chem.*, vol. 270, pp. 2708–2715, Feb. 1995.
- [54] G. W. Christoph, J. Hofrichter, and W. A. Eaton, "Understanding the shape of sickled red cells," *Biophys. J.*, vol. 88, pp. 1371–1376, Feb. 2005.
- [55] M. Lu, M. A. Rab, S. S. Shevkoplyas, and V. A. Sheehan, "Blood rheology biomarkers in sickle cell disease," *Exp. Biol. Med.*, vol. 245, pp. 155–165, Jan. 2020.
- [56] A. Aich, Y. Lamarre, D. P. Sacomani, S. Kashima, D. T. Covas, and L. G. De La Torre, "Microfluidics in sickle cell disease research: State of the art and a perspective beyond the flow problem," *Front. Mol. Biosci.*, vol. 7, p. 558982, Mar. 2021.
- [57] V. Rizzuto and et al., "Combining microfluidics with machine learning algorithms for rbc classification in rare hereditary hemolytic anemia," *Sci. Rep.*, vol. 11, p. 13553, June 2021.
- [58] D. S. Darbari, V. A. Sheehan, and S. K. Ballas, "The vaso-occlusive pain crisis in sickle cell disease: Definition, pathophysiology, and management," *Eur. J. Haematol.*, vol. 105, pp. 237–246, Sept. 2020.
- [59] R. E. Ware, M. De Montalembert, L. Tshilolo, and M. R. Abboud, "Sickle cell disease," *The Lancet*, vol. 390, pp. 311–323, July 2017.
- [60] M. D. Lynne D. Neumayr, M. D. Caroly C. Hoppe, and C. Brown, "Sickle cell disease: Current treatment and emerging therapies," Nov. 2019. [Online, Accessed: July 28, 2023]. Available: <https://www.ajmc.com/view/>

sickle-cell-disease-current-treatment-and-emerging-therapies.

- [61] J. Kanter and C. Falcon, “Gene therapy for sickle cell disease: where we are now?,” *Hematology*, vol. 2021, pp. 174–180, Dec. 2021.
- [62] A. A. Abraham and J. F. Tisdale, “Gene therapy for sickle cell disease: moving from the bench to the bedside,” *Blood*, vol. 138, pp. 932–941, Sept. 2021.
- [63] S. Lotterman and S. Sharma, “Blood transfusion,” *StatPearls*, Jun 20 2023. In: StatPearls [Internet]. Treasure Island (FL): StatPearls Publishing; 2024 Jan–.
- [64] W. H. Organization, “Global status report on blood safety and availability 2021,” 2022. [Online, Accessed: August 19, 2023]. Available: <https://www.who.int/publications-detail-redirect/9789240051683>.
- [65] E. Parliament and C. of the European Union, “Directive 2004/23/ec of the european parliament and of the council,” 2004. [Online, Accessed: August 20, 2023]. Available: <https://eur-lex.europa.eu/legal-content/EN/TXT/?uri=CELEX:32004L0023>.
- [66] D. Mvere and Weltgesundheitsorganisation, eds., *Manual on the management, maintenance and use of blood cold chain equipment*. Geneva: World Health Organization, 2005.
- [67] H. Relevy, A. Koshkaryev, N. Manny, S. Yedgar, and G. Barshtein, “Blood banking–induced alteration of red blood cell flow properties,” *Transfusion (Paris)*, vol. 0, pp. 071005074756002–???, Sept. 2007.
- [68] N. J. H. Raat, F. Berends, A. J. Verhoeven, D. De Korte, and C. Ince, “The age of stored red blood cell concentrates at the time of transfusion,” *Transfus. Med.*, vol. 15, pp. 419–423, Oct. 2005.
- [69] E. Parliament and C. of the European Union, “Regulation (eu) 2017/745 of the european parliament and of the council,” 2017. [Online, Accessed: August 20, 2023]. Available: <https://eur-lex.europa.eu/legal-content/EN/TXT/?uri=CELEX:32017R0745>.
- [70] L. Larsson and et al., “Non-phthalate plasticizer deht preserves adequate blood component quality during storage in pvc blood bags,” *Vox Sang.*, vol. 116, pp. 60–70, Jan. 2021.
- [71] D. Chen, K. Serrano, and D. V. Devine, “Introducing the red cell storage lesion,” *ISBT Sci. Ser.*, vol. 11, pp. 26–33, Jan. 2016.
- [72] J. W. Lagerberg, H. Korsten, P. F. van der Meer, and D. de Korte, “Pre-



- vention of red cell storage lesion: a comparison of five different additive solutions,” *Blood Transfus.*, 2017.
- [73] M. G. Lopes, S. M. Recktenwald, G. Simionato, H. Eichler, C. Wagner, S. Quint, and L. Kaestner, “Big data in transfusion medicine and artificial intelligence analysis for red blood cell quality control,” *Transfusion Medicine and Hemotherapy*, vol. 50, no. 3, pp. 163–173, 2023.
- [74] G. R. Schleder and A. Fazzio, “Machine learning na física, química, e ciência de materiais: Descoberta e design de materiais,” *Rev. Bras. Ensino Física*, vol. 43, no. suppl 1, p. e20200407, 2021.
- [75] P. Hamet and J. Tremblay, “Artificial intelligence in medicine,” *Metabolism*, vol. 69, pp. S36–S40, Apr. 2017.
- [76] L. Kaestner, “Artificial intelligence meets hematology,” *Transfus. Apher. Sci.*, vol. 59, p. 102986, Dec. 2020.
- [77] F. Rosenblatt, “The perceptron: A probabilistic model for information storage and organization in the brain,” *Psychological Review*, vol. 65, no. 6, pp. 386–408, 1958.
- [78] M.-C. Popescu, V. Balas, L. Perescu-Popescu, and N. Mastorakis, “Multi-layer perceptron and neural networks,” *WSEAS Transactions on Circuits and Systems*, vol. 8, 07 2009.
- [79] S. Mouloudi, H. Rahmanpanah, S. Gohari, C. Burvill, and H. M. Davies, “Feedforward backpropagation artificial neural networks for predicting mechanical responses in complex nonlinear structures: A study on a long bone,” *Journal of the Mechanical Behavior of Biomedical Materials*, vol. 128, p. 105079, 2022.
- [80] D. E. Rumelhart, G. E. Hinton, and R. J. Williams, “Learning representations by back-propagating errors,” *Nature*, vol. 323, pp. 533–536, 1986.
- [81] S. Ruder, “An overview of gradient descent optimization algorithms,” 2017.
- [82] C. Doersch, “Tutorial on variational autoencoders,” 2021.
- [83] K. O’Shea and R. Nash, “An introduction to convolutional neural networks,” *ArXiv*, vol. abs/1511.08458, 2015.
- [84] K. O’Shea and R. Nash, “An introduction to convolutional neural networks,” 2015.
- [85] A. F. Agarap, “Deep learning using rectified linear units (relu),” *arXiv preprint arXiv:1803.08375*, 2018.

- [86] H. E. Kim, A. Cosa-Linan, N. Santhanam, M. Jannesari, M. E. Maros, and T. Ganslandt, "Transfer learning for medical image classification: a literature review," *BMC Med. Imaging*, vol. 22, p. 69, Dec. 2022.
- [87] S. J. Pan and Q. Yang, "A survey on transfer learning," *IEEE Trans. Knowl. Data Eng.*, vol. 22, pp. 1345–1359, Oct. 2010.
- [88] K. Matthews, E. S. Lamoureux, M.-E. Myrand-Lapierre, S. P. Duffy, and H. Ma, "Technologies for measuring red blood cell deformability," *Lab. Chip*, vol. 22, no. 7, pp. 1254–1274, 2022.
- [89] Z. Wen and et al., "Biophysical meanings of orientation and deformation of rbcs in shear flow field of low viscosity with new ektacytometry," *Sci. China C Life Sci.*, vol. 41, pp. 195–202, Apr. 1998.
- [90] H. L. Reid, A. J. Barnes, P. J. Lock, J. A. Dormandy, and T. L. Dormandy, "A simple method for measuring erythrocyte deformability," *J. Clin. Pathol.*, vol. 29, pp. 855–858, Sept. 1976.
- [91] I. Dulińska and et al., "Stiffness of normal and pathological erythrocytes studied by means of atomic force microscopy," *J. Biochem. Biophys. Methods*, vol. 66, pp. 1–11, Mar. 2006.
- [92] S. Hénon, G. Lenormand, A. Richert, and F. Gallet, "A new determination of the shear modulus of the human erythrocyte membrane using optical tweezers," *Biophys. J.*, vol. 76, pp. 1145–1151, Feb. 1999.
- [93] A. Kihm, L. Kaestner, C. Wagner, and S. Quint, "Classification of red blood cell shapes in flow using outlier tolerant machine learning," *PLOS Comput. Biol.*, vol. 14, p. e1006278, June 2018.
- [94] J. Martin-Wortham, S. M. Recktenwald, M. G. M. Lopes, L. Kaestner, C. Wagner, and S. Quint, "A deep learning-based concept for high throughput image flow cytometry," *Appl. Phys. Lett.*, vol. 118, p. 123701, Mar. 2021.
- [95] E. S. Lamoureux, E. Islamzada, M. V. J. Wiens, K. Matthews, S. P. Duffy, and H. Ma, "Assessing red blood cell deformability from microscopy images using deep learning," *Lab. Chip*, vol. 22, no. 1, pp. 26–39, 2022.
- [96] D. P. Kingma and J. Ba, "Adam: A method for stochastic optimization," *arXiv preprint arXiv:1412.6980*, 2014.
- [97] M. Doan and et al., "Objective assessment of stored blood quality by deep learning," *Proc. Natl. Acad. Sci.*, vol. 117, pp. 21381–21390, Sept. 2020.
- [98] K. He, X. Zhang, S. Ren, and J. Sun, "Deep residual learning for image

- recognition,” 2015.
- [99] J. Friend and L. Yeo, “Fabrication of microfluidic devices using polydimethylsiloxane,” *Biomicrofluidics*, vol. 4, p. 026502, June 2010.
  - [100] D. A. Kihm, “Deformability-induced effects of red blood cells in flow,” 2021.
  - [101] J. M. Nowful, S. C. Lok, and S.-W. R. Lee, “Effects of plasma cleaning on the reliability of wire bonding,” in *Advances in Electronic Materials and Packaging 2001 (Cat. No.01EX506)*, (Jeju Island, South Korea), pp. 39–43, IEEE, 2001.
  - [102] G. van Rossum, “Python tutorial,” Tech. Rep. CS-R9526, Centrum voor Wiskunde en Informatica (CWI), Amsterdam, May 1995. [Online, Accessed: July 5, 2023]. Available: <https://ir.cwi.nl/pub/5007>.
  - [103] R. V. Chadnov and A. V. Skvortsov, “Convex hull algorithms review,” in *Proceedings. The 8th Russian-Korean International Symposium on Science and Technology, 2004. KORUS 2004.*, (Tamsk, Russia), pp. 112–115, IEEE, 2004.
  - [104] G. Bradski, “The opencv library,” *Dr. Dobbs’s Journal: Software Tools for the Professional Programmer*, vol. 25, no. 11, pp. 120–123, 2000.
  - [105] Z. Wang, A. C. Bovik, H. R. Sheikh, and E. P. Simoncelli, “Image quality assessment: From error visibility to structural similarity,” *IEEE Trans. Image Process.*, vol. 13, pp. 600–612, Apr. 2004.
  - [106] S. Van der Walt, J. L. Schönberger, J. Nunez-Iglesias, F. Boulogne, J. D. Warner, N. Yager, E. Gouillart, and T. Yu, “scikit-image: image processing in python,” *PeerJ*, vol. 2, p. e453, 2014.
  - [107] I. Goodfellow, Y. Bengio, and A. Courville, *Deep Learning*. MIT Press, 2016.
  - [108] G. Jocher, A. Chaurasia, A. Stoken, J. Borovec, Y. Kwon, K. Michael, J. Fang, Z. Yifu, C. Wong, D. Montes, *et al.*, “ultralytics/yolov5: v7. 0-yolov5 sota realtime instance segmentation,” *Zenodo*, 2022.
  - [109] A. Bochkovskiy, C.-Y. Wang, and H.-Y. M. Liao, “Yolov4: Optimal speed and accuracy of object detection,” 2020.
  - [110] C.-Y. Wang, H.-Y. M. Liao, I.-H. Yeh, Y.-H. Wu, P.-Y. Chen, and J.-W. Hsieh, “Cspnet: A new backbone that can enhance learning capability of cnn,” *2020 IEEE/CVF Conference on Computer Vision and Pattern Recognition Workshops (CVPRW)*, pp. 1571–1580, 2019.
  - [111] S. Liu, L. Qi, H. Qin, J. Shi, and J. Jia, “Path aggregation network for

- instance segmentation,” *2018 IEEE/CVF Conference on Computer Vision and Pattern Recognition*, pp. 8759–8768, 2018.
- [112] M. Bessis, R. I. Weed, and P. F. Leblond, *Red Cell Shape*. Berlin, Heidelberg: Springer Berlin Heidelberg, 1973.
- [113] M. Diez-Silva, M. Dao, J. Han, C.-T. Lim, and S. Suresh, “Shape and biomechanical characteristics of human red blood cells in health and disease,” *MRS bulletin*, vol. 35, no. 5, pp. 382–388, 2010.
- [114] J. R. Hess, “Conventional blood banking and blood component storage regulation: opportunities for improvement,” *Blood Transfusion*, vol. 8, no. Suppl 3, pp. s9–s15, 2010.
- [115] C. M. Pandey and et al., “Microfluidics based point-of-care diagnostics,” *Biotechnol. J.*, vol. 13, p. 1700047, Jan. 2018.
- [116] T. Thomas and et al., “Evidence of structural protein damage and membrane lipid remodeling in red blood cells from covid-19 patients,” *J. Proteome Res.*, vol. 19, pp. 4455–4469, Nov. 2020.
- [117] R. M. Bateman, M. D. Sharpe, M. Singer, and C. G. Ellis, “The effect of sepsis on the erythrocyte,” *Int. J. Mol. Sci.*, vol. 18, p. 1932, Sept. 2017.
- [118] G. Lim H. W., M. Wortis, and R. Mukhopadhyay, “Red blood cell shapes and shape transformations: Newtonian mechanics of a composite membrane: Sections 2.5–2.8,” in *Soft Matter* (G. Gompfer and M. Schick, eds.), pp. 139–204, Weinheim, Germany: Wiley-VCH Verlag GmbH & Co. KGaA, 2008.
- [119] E. Ponder, *Hemolysis and Related Phenomena*. Saunders, 1948.
- [120] C. Roussel, A. Morel, M. Dussiot, M. Marin, M. Colard, A. Fricot-Monsinjon, A. Martinez, C. Chambrion, B. Henry, M. Casimir, G. Volle, M. Dépond, S. Dokmak, F. Paye, A. Sauvanet, C. Le Van Kim, Y. Colin, S. Georgeault, P. Roingeard, and S. Spitalnik, “Rapid clearance of storage-induced microerythrocytes alters transfusion recovery,” *Blood*, vol. 137, pp. 2285–2298, 2021.
- [121] A. Brandow and R. Liem, “Advances in the diagnosis and treatment of sickle cell disease,” *Journal of hematology & oncology*, vol. 15, no. 1, p. 20, 2022.
- [122] J. White, M. U. Callaghan, X. Gao, K. Liu, A. Zaidi, M. Tarasev, and P. C. Hines, “Longitudinal assessment of adhesion to vascular cell adhesion molecule-1 at steady state and during vaso-occlusive crises in sickle cell disease,” *British Journal of Haematology*, vol. 196, no. 4, pp. 1052–1058, 2022.
- [123] R. E. Horton, “Microfluidics for investigating vaso-occlusions in sickle cell

- disease,” *Microcirculation*, vol. 24, p. e12373, July 2017.
- [124] Y. Alapan, Y. Matsuyama, J. Little, and U. Gurkan, “Dynamic deformability of sickle red blood cells in microphysiological flow,” *Technology*, vol. 4, no. 02, pp. 71–79, 2016.
- [125] R. An and U. A. Gurkan, “Emerging functional microfluidic assays for the study of thromboinflammation in sickle cell disease,” *Current Opinion in Hematology*, vol. 29, no. 6, pp. 327–334, 2022.
- [126] United Kingdom National Health Service (NHS), “Huntington’s disease: Diagnosis,” 2021. [Online, Accessed: July 5, 2023]. Available: <https://www.nhs.uk/conditions/huntingtons-disease/diagnosis/>.
- [127] M. Luten, B. Roerdinkholder-Stoelwinder, N. P. M. Schaap, W. J. De Grip, H. J. Bos, and G. J. C. G. M. Bosman, “Survival of red blood cells after transfusion: a comparison between red cells concentrates of different storage periods,” *Transfusion (Paris)*, vol. 48, pp. 1478–1485, July 2008.
- [128] G. Barshtein, I. Pajic-Lijakovic, and A. Gural, “Deformability of stored red blood cells,” *Front. Physiol.*, vol. 12, p. 722896, Sept. 2021.
- [129] G. Edgren and et al., “A population-based binational register for monitoring long-term outcome and possible disease concordance among blood donors and recipients,” *Vox Sang.*, vol. 91, pp. 316–323, Nov. 2006.
- [130] N. M. Heddle and et al., “The association between blood donor sex and age and transfusion recipient mortality: an exploratory analysis,” *Transfusion (Paris)*, vol. 59, pp. 482–491, Feb. 2019.
- [131] Z. Isiksacan and et al., “Assessment of stored red blood cells through lab-on-a-chip technologies for precision transfusion medicine,” *Proc. Natl. Acad. Sci.*, vol. 120, p. e2115616120, Aug. 2023.
- [132] L. Kaestner, P. Schlenke, M. von Lindern, and W. El Nemer, “Translatable tool to quantitatively assess the quality of red blood cell units and tailored cultured red blood cells for transfusion,” *Proceedings of the National Academy of Sciences*, vol. 121, no. 11, p. e2318762121, 2024.
- [133] European Medicines Agency, “Directive 2002/98/ec of the european parliament and of the council,” 2002. [Online, Accessed: July 5, 2023]. Available: [https://www.ema.europa.eu/en/documents/regulatory-procedural-guideline/directive-2002/98/ec-european-parliament-council-27-january-2003-setting-standards-quality-safety-collection-testing\\_en.pdf](https://www.ema.europa.eu/en/documents/regulatory-procedural-guideline/directive-2002/98/ec-european-parliament-council-27-january-2003-setting-standards-quality-safety-collection-testing_en.pdf).

- [134] L. Amand-Eeckhout, “Standards of quality and safety for substances of human origin intended for human application,” Sept. 2023. [Online, Accessed: July 5, 2023]. Available: [https://www.europarl.europa.eu/RegData/etudes/BRIE/2023/751449/EPRS\\_BRI\(2023\)751449\\_EN.pdf](https://www.europarl.europa.eu/RegData/etudes/BRIE/2023/751449/EPRS_BRI(2023)751449_EN.pdf).

# Acknowledgments

This work was carried out within the international EVIDENCE consortium, funded by the European Union's Horizon 2020 research program. EVIDENCE involved the collaboration of 16 European partner institutes.

First and foremost, I would like to express my gratitude to my PI, Dr. Stephan Quint, for selecting me to be part of this exceptional PhD program and for the numerous opportunities that have shaped my professional development. I am also deeply thankful to Prof. Dr. Lars Kaestner for his unwavering support throughout my academic journey. I would also like to extend my appreciation to Prof. Dr. Christian Wagner for warmly welcoming me into his research group. The invaluable exchange of knowledge and experiences within this group has significantly contributed to my growth as a researcher.

From Christian's group, I am particularly grateful to Dr. Steffen Recktenwald, whose guidance and supervision have been essential in my progress. I would like to acknowledge Dr. Thomas John for his technical assistance and support. Special thanks go to my friend and flatmate, Min Qiao. I would also like to express my gratitude to my friends Yazdan Rashidi and Felix Mauer for the countless coffee breaks and enjoyable conversations. I am also thankful to Greta Simionato, Nils Boussard, Mohamed, Khadija Larhrissi, Mohammed Bendaoud, Mohammed Nouaman, Dr. Alexis Darras, Dr. Andreas Tschöpe, and all other past and present colleagues for their collaboration and support. I extend my thanks to our wonderful secretary, Sara Zimmermann, and our previous secretary, Nina Apfelbaum, as well as technician Karin Kretsch for their continuous assistance.

Furthermore, I would like to express my gratitude to all my fellow PhD students from the EVIDENCE project. Our productive meetings and conferences have been both enriching and inspiring: Silvia Neri, Giulia Iacono, Catarina Freire, Mariam Dynar, Aline Hatem, and Robert Seute.

Aos meus estimados amigos brasileiros que trouxeram um pouco do nosso lar para Saarbrücken por meio de sua calorosa presença — Ricardo Campos, Nicole Klein, Julia Spatzek e Bruno Stepien: muito obrigado! Também gostaria de expressar um agradecimento especial ao meu esposo, Matheus Schaefer, que concordou em embarcar nessa aventura ao meu lado. E, finalmente, agradeço aos meus pais, Leandro e Fabiana Lopes, e à minha irmã, Beatriz Lopes, no Brasil, cujo amor incondicional supera qualquer distância que possa existir.